Characterization of structure and properties of thin film crystals and ferroelectric $BiFeO_3$ - a coupled TEM, SPM, and optical probe approach

by

Jacob Ragnar Jokisaari

A dissertation submitted in partial fulfillment
of the requirements for the degree of
Doctor of Philosophy
(Materials Science and Engineering)
in the University of Michigan
2016

Doctoral Committee:

Professor Emmanoul Kioupakis, Co-Chair
Professor Xiaoqing Pan, Co-Chair
Adjunct Professor George W. Graham
Professor Joanna M. Millunchick
Associate Professor Jamie D. Phillips

Dedication

To my wife, to my family, and to the many people who have helped and supported me over these long years. This work is dedicated to you without whom it would never have been possible.

Acknowledgements

There are many who deserve my acknowledgement and thanks. In no particular order I would like to thank:

Professor Pan and **George Graham**, for allowing me to join the group after leaving my previous group, my committee for help and support in completing this work

Professors **Emmanoul Kioupakis**, **Joanna Millunchick**, and **Jamie Phillips** for being my committee, and fo many good conversations and especially, encouragement in the last few weeks

Previous and current Pan group Members:

Chris Nelson and **Peng Gao** whose work has informed this thesis more than any other and for getting me into this area of materials science in the first place,

Linze Li, **Shuyi Zhang**, **Yi Zhang**, **Lin Xie**, **Sung Joo Kim**, **Kui Zhang**, and **Pei Lei**, all of whom have contributed directly to this work

Also, **Mingjie Xu**, who is the other half of the *in-situ* TEM holder design team, who deserves special recognition, and will carry the project forward into the future

Chang Zhou, **Baihai Li**, and **Mike Katz**, with whom it has been my privilege to work with over these past years, and to all other current and former members of the Pan Group

And special thanks is due **Emeritus Professor Wilbur Bigelow** for immense help and encouragement in TEM holder design

Finally, thanks to our many collaborators who were instrumental in performing the work, including: **Darrel Schlom**, **Colin Heikes** and **Carolina Adamo** from Cornell for growing the many BFO samples, **Yuanming Liu** and **Jiangyu Li** from Univ. of Washington for teaching me PFM, and many others here and elsewhere that are too numerous to list

I would also like to acknowledge the agencies provided funding for these projects including the US Department of Energy (DOE) under grant DE-FG02-07ER46416 and the National Science Foundation under grant DMR-1420620.

Table of Contents

List of Figures

Abstract

Correlating advanced microscopy methods including transmission electron microscopy, scanning probe microscopy, and optical spectroscopy on the same materials and even the same specimens allows complimentary measurements to be obtained, revealing new details about structure-property relationships measured on a nanometer scale. Combining measurements not only corroborates the information obtained from any particular method, but also compensates for deficiencies of any single technique. An array of microscopy techniques including high resolution transmission electron microscopy, scanning probe microscopy, and Raman spectroscopy were applied to address scientific and engineering questions concerning the structure and properties of domain patterns in $BiFeO_3$ ferroelectric thin films and to examine novel TiO_2(B) thin films suitable for Li-ion battery applications. In $BiFeO_3$, application of these combined techniques allowed a relationship between epitaxial strain and domain width to be established, two cases of strained films with unique domain structures to be identified, transformation of domain structures from all 109° to mixed to all 71° based on differing film thicknesses of 100 and 200 nm to be observed, and to identify growth-induced defects that control domain structure over very long range, 100 nm or more, compared to many studies. In TiO_2(B) films, a combination of advanced microscopy and first principals calculations were applied with Raman spectroscopy to produce a definitive

reference for further investigation of the crystallinity, structure, composition, and properties of TiO_2(B) materials with Raman spectroscopy. Finally to extend these studies of nanostructures and allow direct measurement of electronic and optical properties, the design, development, and construction of proof-of-concept prototypes of specimen rods for in-situ transmission electron microcopy combining electrical probe, scanning tunneling measurements, and optical excitation and spectroscopy is discussed.

Chapter 1

Introduction and Background

In this chapter, I introduce the motivation for this work, and discuss the materials used in this work, $BiFeO_3$ (referred to as BFO from here on) and TiO_2(B), in terms of their properties and applications. There is considerable emphasis placed on the properties of ferroelectricity and domain walls in BFO, as these topics comprise a major component of this work. Finally, the development of a new in-situ holder, a major contribution of this work, is discussed.

1.1 Introduction

The continuing pressure to create ever smaller and more complex electronic devices, requiring ever smaller components, has driven the need to engineer materials on the nanoscale. One potential group of materials that shows promise for devices is thin-film transition metal oxides[1]. This group encompasses a huge number of different compounds with different crystals structures and properties. As such this work focuses on just two that have been of particular interest to researchers. One class of such oxides is the ferroelectric perovskites, where domains of specific polarization affect the local electronic properties[2], ferroelectric switching couples with other properties such as photovoltages[3], and through magnetoelectric and multiferroic effects, with magnetism[4], as in the compound $BiFeO_3$. The domain walls themselves have different properties than the bulk material and can be utilized as functional elements[5]. In BFO,

controlling the type, orientation, and character of domains and domain boundaries is critical to designing devices using this material.

The other important group of oxide materials addressed in this work is the many polymorphs of titanium oxide, which have found application in sensors[6-9], photocatalysis[10-13], solar cells[14-17], and more recently, a potential anode materials for Li-ion batteries[18-24]. Of the polymorphs of TiO_2, including rutile, brookite, and anatase, particular interest has been focused on the relatively recently discovered bronze phase of TiO_2 (TiO_2(B)). While nanostructured powders of TiO_2(B) have been described before, Zhang *et al*.[25]were the first to grow thin films of this material and thereby make it available for characterization here, allowing detailed analysis of the film's unique structure and the opportunity to probe its functional properties in high quality crystalline films. A detailed understanding of the crystal structure, defects, structural interfaces, and how this affects properties is essential to exploit the potential of these materials in modern technological applications.

Characterization of materials on the nanoscale is a key component of modern materials science and methods to study the smallest scales have been evolving rapidly. Electron microscopy has been used for many decades to image the atomic scale. The modern development of aberration correctors for electron microscopes has improved resolution limits into the sub-angstrom range[26, 27]. Scanning probe technology is another means of accessing the nanoscale, first with the development of scanning tunneling microscopy (STM) followed by atomic force microscopy (AFM) in the 1980's. From these beginnings, scanning probe microscopy (SPM) machines have become truly multifunctional, combining surface mapping, current mapping (CAFM), biasing,

capacitance, piezoresponse force microscopy (PFM), and more in a single device. Advanced optical techniques, such as scanning Raman spectroscopy, which itself depends on recent developments in laser technology and optical filters, have also been integrated with SPM. The development of all of these new techniques is driven by the new information that can be gathered from correlated measurements obtained via multiple techniques, preferably applied simultaneously, or at least sequentially, to the same specimens.

For this study, I apply advanced microscopy methods including transmission electron microscopy, scanning probe microscopy, Raman spectroscopy, and develop new *in-situ* TEM methods in order to examine factors determining domain structures in ferroelectric BFO and to characterize novel thin films of the battery material, TiO_2(B). In BFO the effects of film thickness, epitaxial strain, and extended defect structures on domain patterns and switching behavior are examined in detail in order to elucidate factors which control the type, density, and size of ferroelectric domain walls. Control of the type and distribution of domain walls is a necessary prerequisite to engineering domain-based devices. Secondly, advanced microscopy techniques are employed to examine novel thin films of the titanium oxide battery material TiO_2(B) in detail. Finally, in order to improve upon these methods, and better measure and understand the functional properties of such nanoscale details, I undertook the construction of a new in-situ TEM specimen rod platform to combine SPM, TEM, and optical measurement. Design, construction details, and proof of concept are included in chapter 6.

1.2 Background

1.2.1 Ferroelectrics and Multiferroics

The property of ferroelectricity is defined by the existence of a spontaneous polarization, which produces a dipole electric charge in the material. In the context of a crystalline material, this means the unit cell is distorted from perfect crystal symmetry. The displacement between the total positive and negative ionic charges within the unit cell is the polarization vector. Overall macroscopic electric field is minimized in a manner analogous to magnetic materials; an array of domains of counteracting polarizations forms. The domain structures form to minimize the total energy, balancing the energies associated with surfaces and domain walls, and can be affected by additional factors such as strain or external fields[28]. Within a domain, the polarization is uniform, with all of the unit cells in the volume sharing the same polarization. The zone between two adjacent domains is referred to as a domain wall. This situation is exactly analogous to magnetic domains. The structure and properties of domain walls will be discussed in the next section.

Many of the most scientifically and industrially important ferroelectrics are part of the perovskite family of materials, for which the crystal symmetry can be described by a pseudo-cubic unit cell. Due to the symmetry of the crystal, the polarization vector may point in several equivalent possible directions, giving multiple degenerate polarization states. From a thermodynamic viewpoint, this can be visualized in terms of the free energy diagram as a function of polarization (see Fig. 1.1). The free energy diagram represents the 'switching' shown in the PZT unit cell, pictured in the center of Fig 1.1, where the central oxygen octahedron is displaced along the c-axis. The hysteresis loop

represents the functional measurement of polarization derived by integrating the capacitance as the applied voltage bias is changed, and is also shown in the Fig. 1.1. The total energy of the ferroelectric crystal has multiple, equivalent minima, each corresponding to a specific polarization state. An externally applied force such as an electric field, then, can produce a transition from one polarization state to another. The property of ferroelectricity is tied to several effects, including the piezoelectric effect, the pyroelectric effect, the electrorestrictive effect, and changes in the dielectric properties[29]. Because all of these properties are related to the polarization, polarization switching affects all of them.

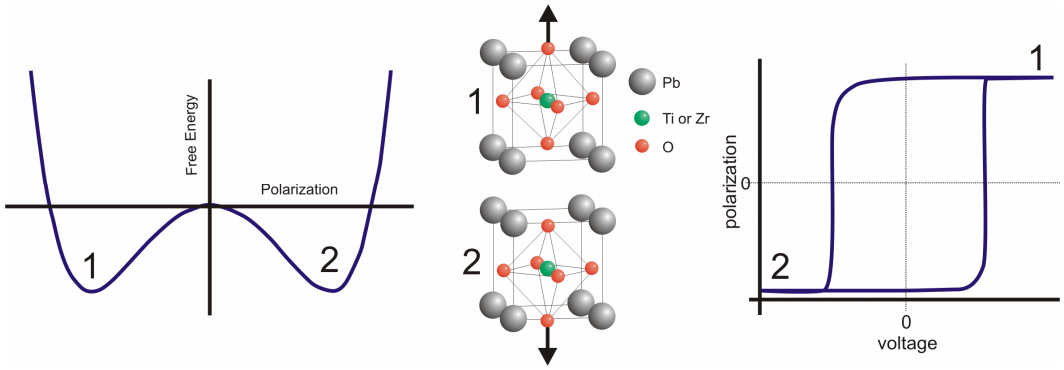

Figure 1.1 Polarization in one dimension with two stable states shown in the free energy curve (left), the atomic displacement in PZT (center), and the classic remnant hysteresis curve (right)

Multiferroic materials are those which have more than one order parameter, such as ferroelectric ordering, that is coupled to a second order parameter, such as magnetism[4]. Multiferroic materials are of technological interest, as the coupled order parameters can be exploited for new type of, for example, memory devices[30]. The best known multiferroic material is BFO, which has both ferroelectric and antiferromagnetic ordering with a curie temperature—where ferroelectricity disappears—of ~1100K and a Neel temperature—where antiferromagnetism becomes paramagnetism—of ~640K[31], both

well above room temperature. A device utilizing this coupling has been described, where BFO is paired with a FeCo magnetic film and switching electrical polarization can be used to switch the ferromagnetic bit in FeCo via coupling through the antiferroelectric order in BFO[32].

The most common application for ferroelectric materials is either for the piezoelectric and converse piezoelectric effects where a displacement is induced by voltage, or a voltage by flexing the ceramic[29]. For the latter, there is a great deal of interest in utilizing these effects for energy harvesting[33]. In electronics applications, the largest interest is in memory devices[30, 34]. For memory, new device architectures such as ferroelectric tunnel junction devices[35], memristor devices[36], devices exploiting coupling between ferroelectric and magnetic properties [37-39], and architectures utilizing domain-wall based microelectronics[40], have been proposed. More recently, ferroelectric materials have become attractive for use in photovoltaic devices where they have been shown to have above-bandgap output voltages[41-43]. This behavior has been demonstrated in several perovskite ferroelectric materials, including $Pb(Zr_{0.2}Ti_{0.8})O_3$ under UV illumination[44], $BiFeO_3$ under visible light[45], while very recently, hybrid organic-inorganic perovskite materials such as the layered perovskite $(benzylammonium)_2PbCl_4$[46, 47] have been discovered.

A few recent developments have contributed to the renaissance of interest in ferroelectric materials. For one, the growth of high quality thin films has become possible by methods such as RF sputtering, pulsed laser deposition (PLD), and reactive molecular beam epitaxy (MBE). Prior to this, most ferroelectric materials were only available as cut single crystals, or poor-quality polycrystalline films prepared by sol-gel or similar

techniques. The new availability of high quality single crystal films is partially due to the development of suitable substrates for epitaxial growth[48]. The availability of well-matched substrates allows for much greater control of crystal quality, orientation, and strain in thin film growth. Such thin films provide an ideal model system for characterization of ferroelectric properties with respect to defects and to boundary conditions such as built-in fields, and misfit strain. Furthermore, the demand for ever lower power consumption and smaller components for electronic devices drives interest in ferroelectric oxide thin films as an alternative to silicon based devices in some applications, particularly permanent memories[5]. In addition, there has also been immense growth in the demand for piezoactuators and good dielectrics for which the ferroelectric oxides are suitable[34]. Finally, the advent and very rapid improvement over the past decade in scanning probe and *in-situ* microscopy methods have made accurate nanoscale measurements and simultaneous electronic characterization of ferroelectric polarization possible, driving scientific interest in the materials as the new technology provides access to hitherto unavailable length scales. From these studies, it has become clear that the properties of domain walls themselves, rather than the bulk material, control the properties, opening the possibility that domain walls themselves may be useful to make nano-electronic devices[5, 49].

1.2.2 Domain walls and their properties

As discussed previously, ferroelectric domains, like their magnetic analogs, form long-range twinned structures to minimize uncompensated electric charges or strain induced by the polarization. Such a twin structure is referred to as a domain structure, or pattern. The characteristics of the walls between domains depend on the material, and the unit cell

direction along which the polarization occurs. In pseudocubic tetragonal systems such as PZT, the displacement is along any <100> direction, while in a pseudocubic rhombahedral system such as BFO the polarization occurs along the <111> body diagonal. Even within one material, then, several different types of domain wall can form. These are generally referred to by the angle they form between the polarization vectors, such as the 180° domain wall that would form between the two polarization states shown in Fig. 1.2. Each domain wall type has a different associated bound charge, stress, etc., and can display distinct properties, such as electrical conductivity[5, 40, 50]. The domain structure of BFO is covered in more detail in section 1.2.3.

Domain walls can be charged or uncharged depending on the direction of the polarization vectors in the adjacent regions. A head-to-tail arrangement where they point in the same direction is uncharged, while a head-to-head or a tail-to-tail arrangement will result in a net bound charge at the boundary. Charged domains walls do not usually form, as they have much higher energies than uncharged domain walls, but they are expected to have significantly different electrical properties. There is some evidence, for example, of structure changes induced at charged domain walls[51].

Several studies, theoretical and experimental, have examined the electrical conductivity of ferroelectric materials in the bulk. In general, ferroelectric oxides are relatively insulating in, but for what conduction does occur, there have been several studies into the mechanisms underpinning leakage currents. In ferroelectrics such as PZT and BFO, it has been shown that interface-determined Schottky emission, or Fowler-Nordheim tunneling at higher applied voltages[52, 53], were the major mechanisms. It has also been shown that these mechanisms dominate conduction when the ferroelectric is paired

with a metallic (platinum) or an oxide (SRO, LSMO) electrode. These bulk conduction mechanisms determine the leakage currents and degrade the ferroelectric performance overall. However, changes in conduction based on changes in polarization are a potentially useful property. In order to examine this property, it is necessary to examine conduction near domain walls and other features in ferroelectric thin films.

Recently, many studies have indicated an anomalously large or unexpected conductivity at domain boundaries in various ferroelectric materials, a behavior which several papers have noted may allow for new device applications[2, 50, 54-56]. Seidel *et al.* showed conductivity at the domain wall in a freshly switched domain via PFM and CAFM[2]. Landau-Ginsberg-Devonshire calculations suggested that the bandgap decreases near a domain wall, lowering the barrier to conduction [50]. Additionally, the possibility that band bending and a lowering in the Schottky barrier near a domain wall contributes to static domain wall conductivity, and suggests that suitable doping might be used to control conductivity. Lanthanum doping of BFO has been examined[56], and was shown to modulate the conductivity. The measurement showed that the change in conductivity was thermally activated, and demonstrated a shift in the conduction mechanism depending on the bias voltage from Schottky emission, where thermally excited electrons constitute the bulk of conduction, to Fowler-Nordheim tunneling, where electrons begin to tunnel through the energy barrier, increasing the current. Farokhinpoor demonstrated conductivity in 71° domain walls in BFO, and similarly attributed the static conductivity of these domain walls to a decrease in the Schottky barrier height at higher voltages, and to electron-filled trap states at lower voltages[57]. If the conductivity was in fact due to barrier height, several authors suggested that the conductivity could be tuned

or even that a metal-to-insulator transition may be possible at the domain boundary with appropriate bandgap design[55, 56].Yang *et al*. took this approach, doping BFO with calcium[45]. The net effect of this doping was a large anisotropy between the conductivity of the as-grown film and of a switched domain area, such that a switched domain in this film shows markedly higher conductivity than the surrounding material. This effect was attributed to a high concentration of mobile oxygen vacancies generated by calcium doping, which formed a conductive network under the influence of the electric field in the poled domains. Doping, then, is a means of affecting the static conductivity of domain walls.

Several theoretical studies have examined possible mechanisms for domain wall conductivity, finding several physical mechanisms for conduction. Morozovska *et al.* have shown that in many ferroelectrics, even uncharged domain walls have the potential to be conductive, largely due to band bending and flexoelectric effects[50]. Eliseev *et al.* have examined domain/surface junctions in ferroelectrics and shown that rotostrictive and flexoelectric effects may cause a local decrease in the bandgap and profoundly alter the local electronic properties, even when the domain is not charged [55].In BFO, Catalan *et al.* examined the appearance of a rotation of the oxygen octahedral in the unit cells near the domain wall that may give rise to domain wall conductivity [58]. While many authors look at BFO due to flexoelectric effects at 71° and 109° domain boundaries, Guyonnet *et al.* demonstrated similar conductivity in 180° domain walls in PZT[54], and demonstrated that the conductivity was temperature dependent, highly asymmetric with a diode-like character, and stable over a long period. For charged domain walls in uniaxial $LiNbO_3$, Eliseev *et al.* calculated that the wall conductivity may also depend upon an

accumulation of carriers at the domain wall due to flexoelectric effects. A tail to tail arrangement of the polarization vector of two adjacent areas will produce an excess of holes, and similarly a head to head orientation will produce an excess of electrons. As holes are much less mobile, head to head charged domain walls are expected to show much higher conductivities than the tail to tail arrangement [59]. From all of this work, it appears that static domain wall conductivity is influenced by a number of factors, and many different structure-property relationships depending on subtle changes in the domain structure of ferroelectric materials remain to be discovered.

Static conductivity is not the only current transport process associated with domain boundaries in ferroelectrics. Recently, large changes in conductivity, far above what would be expected from a switching current, have been associated with domain wall motion. Maksymovych *et al.* demonstrated a very large increase in the conductivity upon reaching the coercive voltage and the occurrence of ferroelectric switching, over orders of magnitude of difference in PZT[60]. The bulk film conduction was considered to be due to Fowler-Nordheim tunneling and the current was shown to depend on the polarization. Further work indicated similar high conductivity during domain wall motion in BFO, and attributed the change to electrically induced distortion of the domain wall that, due to weak pinning, resulted in slow domain wall motion over a wide voltage window, and therefore a dependence of the conductivity on the degree of distortion[61]. It has been suggested that all topological defects, which in these materials means domain walls and domain wall intersections, could display anomalous electronic phenomena. For sufficiently small, circular nano-domains with highly curved domain walls, metallic levels of conductivity during switching were found with the conductivity scaling with the

size of the domain[62]. The high conductivity was attributed to tilted, charged domain walls formed during the switching process. These charged domain walls should attract free carriers, forming high-conductivity pathways through the film. The effect was only noted on nano-scale domains with circular margins; larger domains did not show the metallic conduction. It should be noted that there is no confirmation that the smaller, more curved domain walls were actually more tilted during switching as there was no way to image the domain wall through the film thickness.

Application of ferroelectric materials depends strongly on the domain wall configuration and, perhaps, even on the properties of a single domain wall in a thin film[5]. In order to engineer domains on this scale, a few things are necessary. The first is high-quality thin films that form regular arrays of domains, as has been achieved in some thin film growth techniques discussed previously. The second is a means to observe both the overall domain configuration, as well as the nanoscale details of the domain walls. Imaging in both top-down and cross-section is required to accurately determine the mechanisms involved in switching, in order to be certain of such factors as charged domain wall formation. Finally, a method to directly manipulate an individual domain wall, for instance applying a bias, is needed. Few techniques, however, allow direct characterization of these structures. Bulk electronic testing, even of nano-scale devices, average the dynamic effects of several boundaries together and therefore contains no information on the nanoscale dynamics associated with ferroelectric switching. In order to directly access this behavior, a means of truly atomic-scale measurement is required, such measurements as form the core of this work.

1.2.3 $BiFeO_3$

The perovskite compound $BiFeO_3$, is one of the most important of the strongly correlated oxide materials, in which the electrons in the material cannot be treated as having independent motion, that is the total electron wave function cannot be constructed as the product of the wave functions of the individual electrons. This phenomenon gives rise to many unusual properties, such as ferroelectricity. BFO is also the best known single-phase room-temperature multiferroic material, demonstrating both ferroelectricity and antiferromagnetic characteristics with a curie temperature of ~1100K[31] and a Neel temperature of ~640K[31]), well above room temperature. This makes it suitable for electronic devices that operate at ambient temperatures. In addition, the spontaneous ferroelectric polarization is quite strong, ~100 $\mu C/cm^2$, making BFO a potential lead free replacement for the piezoelectric lead-zirconate-titanate(PZT). Interest in the material has grown further in recent years due to its potential for use in multiferroic devices [30, 63],

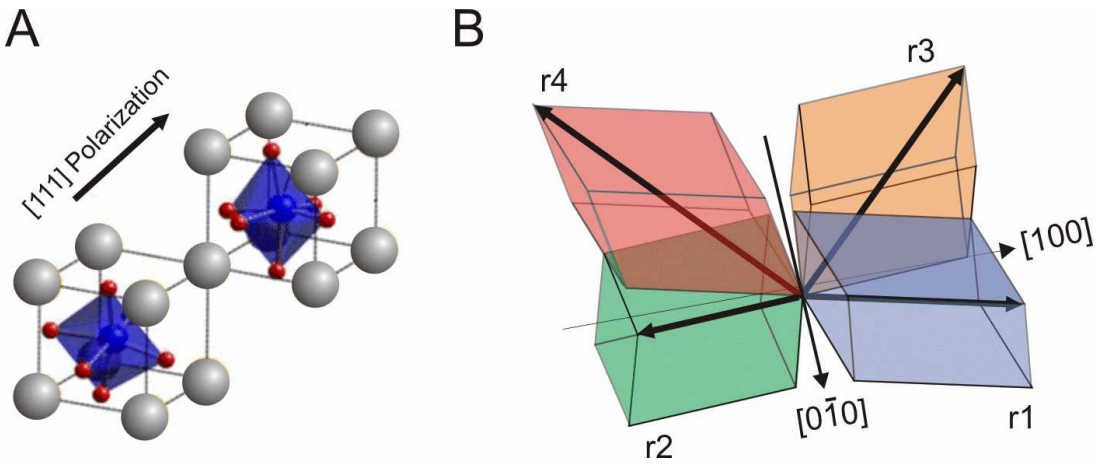

Figure 1.2 Polarization in BFO. A. shows the [111] polarization vector which requires two unit cells due to rotation of the oxygen octahedra B. shows the four possible domain types on orthoscandate substrates

domain wall engineering for electronic devices [5, 40], optical devices[43, 64], and even as a ferroelectric photovoltaic material[43, 45]. In all of these cases, the particular functionality of interest lies in the ability to modulate the associated property, such as magnetic polarization, by ferroelectric switching. Being able to use an electric field to modulate magnetism, and other properties, greatly enlarges the potential utility of this material for novel electronic devices.

BFO has a rhombahedral (R3C) structure that can be considered a pseudocubic perovskite unit cell, with $\alpha=\beta=\delta=90°$ and a lattice parameter of 3.964Å. Polarization in $BiFeO_3$ occurs by displacement of the Fe cation and the oxygen octahedra along the $<111>_P$ directions where the oxygen octahedra are also counter-rotated by ~13.8°[65]. Here, the O suffix indicates orthorhombic indices, and P refers to the pseudocubic indices. Fig. 1.2 shows an atomic model of a BFO unit cell with an exaggerated depiction of the atomic displacements associated with the polarization. Both the Fe ion and the Bi ions are displaced from their ideal positions. This becomes useful in determining polarization by TEM later. Fig. 1.2B shows a schematic of all of the possible polarization orientations, taking into account the restrictions on polarization from the epitaxial relationship with the substrate.

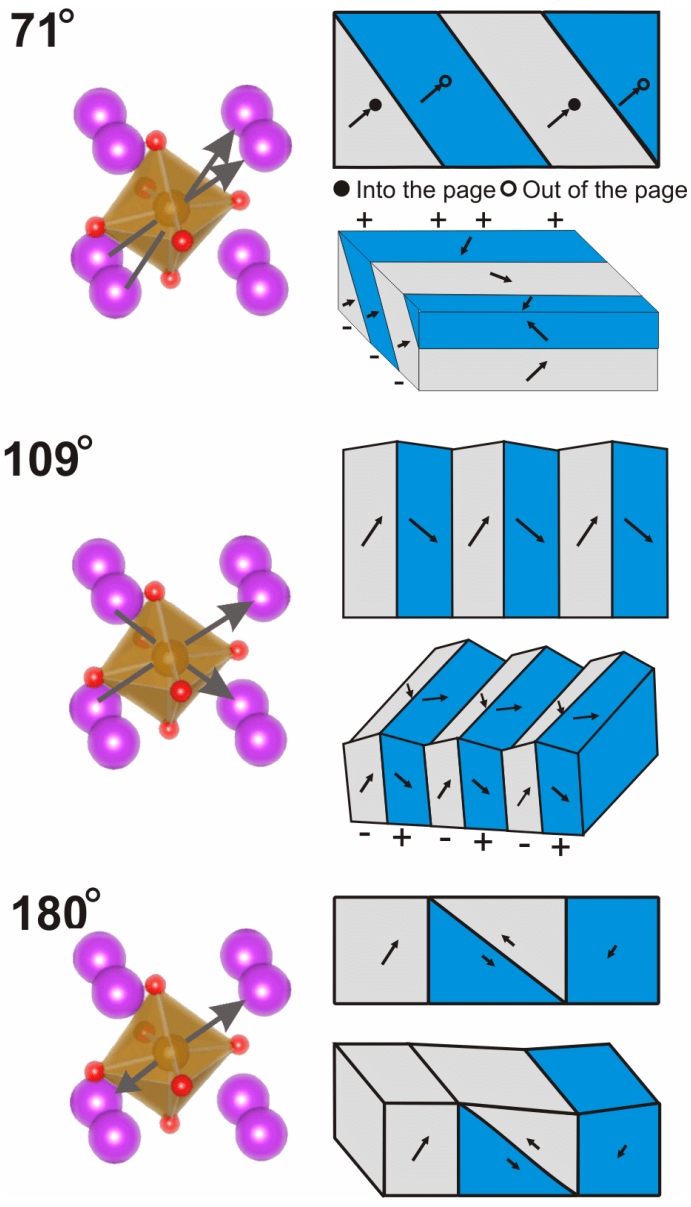

Figure 1.3 Domain structures in BFO projected on a [010] axis for 71° and a [100] axis for 109° and 180° domains. An illustration of the vector change associated with switching for each domain wall type is given on the right, while the representation of the domains is given on the left. The 2-D schematics of the domains are as they appear in TEM

The ferroelectric distortion, along the body diagonal of the unit cell results in four ferroelastic polarization variants. The four variants can be oriented either up or down, for a total of eight unique polarization directions. The intersection between any two of these produces three different domain wall types, which are characterized by the angle through which the polarization vector is rotated using the domain type terminology in Fig. 1.2, we have 71° with (r1+||r4+.i) domains , 109°with (r1-||r4+) domains, or 180° (r1+||r1-), shown in Fig. 1.3. The 71° and 109° domains in particular have slight strain at the domain boundary due to the mismatch in the distortion of the unit cell associated with polarization. As there are different domain wall types, and different domain wall types have different properties, such as conductivity along the domain wall, the preferred orientation of domains in a thin film directly affects its technologically useful properties. The domain wall types as viewed in cross-section in TEM or PFM are depicted in Fig 1.3.

Any of these domain wall types may form twin structures, which are influenced by boundary conditions such as intrinsic or applied fields, or epitaxial strain. Twinned (striped) domain structures form spontaneously to minimize the total energy associated with the polarization, including the domain wall energy and strain energy[66].The type and orientation of the domain walls depends on the orientation of the crystal and the film quality[67], the film thickness[68, 69], defects[70], and many other variables. They are atomic-scale in dimension with a width on the order of a single unit cell in the crystal[71]. Ferroelectric domain walls are generally considered to be of Ising type, where the transition from one polarization to the next is very sharp. In BFO, however, it has been shown that domain walls can have some Bloch or Neel characteristics, with

either a slow change in magnitude, or a rotation of the polarization, respectively, due to flexoelectric effects[72].

1.2.4 TiO_2(B), the bronze phase of titanium oxide

Titanium dioxide (TiO_2) exhibits a number of structurally distinct phases, the best known of which are rutile, brookite and anatase. The bronze phase of titanium dioxide,TiO_2(B), a monoclinic polymorph first described in 1980,[73] has recently attracted much interest due to its unusual layered structure and its potential application in Li-ion batteries,[18-24]photocatalysts,[10-13] chemical sensing,[6-9] and dye-sensitized solar cells.[14-17] The crystal structure of this unusual compound is pictured in the crystal model in Fig. 1.4. Of particular interest are large open 'channels' in the structure. The are sufficiently large as to be able to easily accommodate Li^+ ions, particularly those in the a-b plane, allowing for high capacities, with a theoretical capacity of 355 mAh/g, and an experimentally tested capacity of 120 mAh/g at rapid charge/discharge rates of 80°C in Li-ion battery applications.[25]

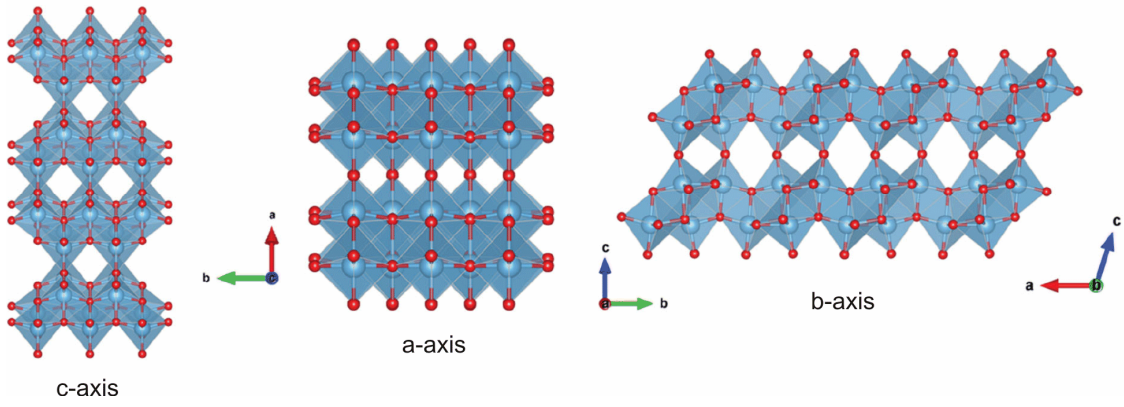

Figure 1.4 Crystal model of TiO_2(B) projected along the three principal axes. The open 'channels' in the crystal structure allow for intercalation of Li ions, making TiO_2(B) an effective battery anode material

There are many reports in the literature on synthesis of nanopowders and nanostructures by hydrothermal methods,[18, 24, 74] aqueous solutions,[73, 75] and calcination of amorphous films.[76] In all of these cases the material produced has been impure and often poorly crystalline, containing a considerable fraction of anatase as well as water from synthesis, which is thought to play a role in stabilizing the TiO_2(B) phase.[74, 77] A few recent reports of TiO_2(B) films produced by chemical hydrolysis[76] and by electrophoresis of nanopowders[17] have yielded micron-thick nanostructured films, but of poor crystalline quality.

Here, epitaxial thin films composed of a nearly pure phase TiO_2(B) were grown on Ca:TiO_2(B) templates themselves grown on $SrTiO_3$ buffered Si. In order to fully characterize this material, we use a mixture of SPM, TEM, polarization-dependent Raman, and theoretical calculation of the Raman spectrum. The combination of characterization techniques allows a definitive Raman fingerprint for the material to be obtained. Details are included in Chapter 6. This type of characterization is applicable to many different systems, and underscores the need to incorporate optical techniques along with electron and scanning probe microscopies. We use a combination of TEM, SPM, and Raman spectroscopy to examine the nanostructure of this important material in thin film form, with the intent to make *in-situ* experiments possible in this materials system.

Chapter 2

Experimental Methods

In this section, the many characterization and sample preparation techniques used to complete this work are reviewed. It has been a theme of this work to push the boundaries of technique and attempt to extend existing methods as well as to develop new methods and the apparatus required to carry them out. This various experimental methods and the background and history of their development are discussed.

2.1 Transmission Electron Microscopy

Transmission electron microscopy is (TEM), perhaps the best method to access truly atomic-scale details within a material. With the modern improvements in software control and the advent of aberration correctors to compensate for spherical aberrations in magnetic lenses, sub-angstrom resolutions have become possible[26, 27]. Such high resolution imaging is required to view atomic-level details such as domain walls and defects in crystals. In particular, atomic scale resolution allows mapping of the polarization distribution in ferroelectrics.

Details of TEM imaging methods that are most directly applicable here are covered in depth by C. T. Nelson[71], and will be repeated here only briefly. There are two major TEM imaging modes employed here. The first uses a parallel electron beam, where the incident electrons are all parallel to each other. This is conventional TEM mode, and can give phase contrast with the objective aperture removed, or diffraction contrast (bright

field (BF), and dark field(DF) with the use of the objective aperture to select the transmitted, or a diffracted beam. In conventional TEM mode, it is possible both to image, and to generate electron diffraction patterns. In the second mode, a convergent beam is used, where the beam is focused to a point at the specimen, and the beam is then raster scanned. This mode is referred to as scanning transmission electron microscopy (STEM). Scattered electrons are collected either by a ring-shaped detector, high-angle annular dark field (HAADF), or a central detector collecting the transmitted electrons for bright field imaging. STEM mode has the benefit of a simpler contrast mechanism, and is sensitive to atomic number, known as z-contrast, as heavy ions are more efficient at scattering electrons. Also, the majority of aberration-corrected microscopes are corrected only in STEM mode, so the majority of the atomic resolution images in this work were collected using STEM. STEM imaging, however, suffers from scan noise, contamination problems, and greater constraints on the sample quality.

Another useful aspect of TEM is its analytic capacity for spectroscopy giving information on the identity of atoms and their oxidation states, through energy dispersive x-ray analysis (EDS), electron energy loss spectroscopy (EELS), and electron diffraction. The spectroscopy methods come from several different types of interactions between the electron beam and the sample. For EELS, some of the electrons in the TEM beam are inelastically scattered during their interaction with the sample. Inelastic scattering results in a characteristic loss of energy, which is associated with a particular element in the case that a core electron was displaced, or a plasmon resonance for very low energy losses[78]. These electrons can be sorted by energy using a magnetic prism[78], resulting in a spectrum of ‘edges’ which yield information on the elemental composition and, for

example, the oxidation state of a metallic element. Another type of scattering event will result in electrons being pushed out of their core energy levels in the sample, and the subsequent optical emission as that vacancy is filled. This releases an X-ray, which is characteristic of the element. The energy of the X-ray can be measured, and this produces the EDS signal[78]. EDS allows the distribution of elements in the specimen to be mapped.

The major techniques employed in this work were diffraction contrast imaging (dark field and bright field) which give excellent contrast of ferroelectric domains, phase contrast imaging for higher resolution imaging, and HAADF STEM for atomic resolution imaging. Examples of diffraction contrast imaging of domains at low and atomic resolutions and of imaging domains in HAADF and BF STEM is shown in Fig. 2.1.

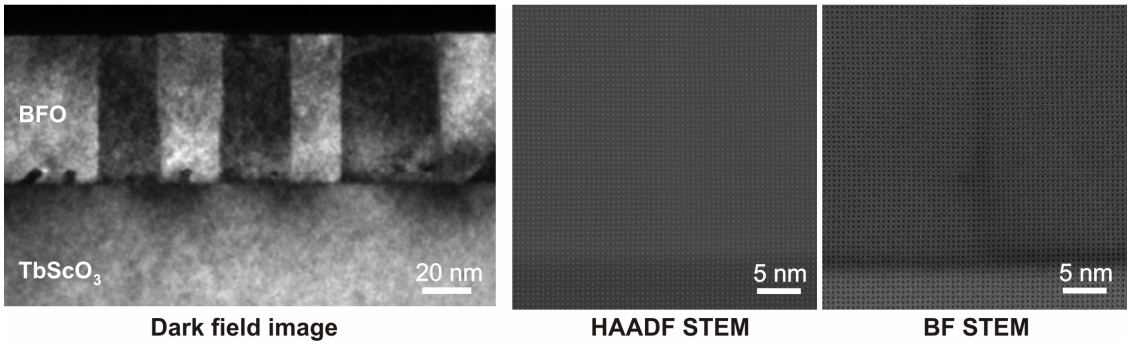

Figure 2.1 Examples of TEM imaging. Diffraction contrast shows domains very clearly, but at poor resolution while z-contrast shows no domain wall contrast, and BF STEM shows weak domain contrast

2.2 In-situ Transmission Electron Microscopy

Since the invention of electron microscopy, there has been interest in not only observing static structures, but also observing physics in action. All of the ways of exerting external stimuli on a sample in the microscope are collectively known as *in-situ* methods. In the transmission electron microscope, phenomenon on the scale of

angstroms can be probed, and over many years, many different experimental apparatus have been designed to allow external stimulus such as temperature, electrical bias, and mechanical force to be applied. These *in-situ* apparatus allow the response of materials to such stimuli to be observed. Despite a great deal of effort, with review articles detailing experiments in heating, cooling, mechanical deformation, environmental control such as supporting gas and liquid atmospheres, and magnetic contrast via Lorenz microscopy dating back to the 1970's[79], much remains to be done. For electronic materials, applying a voltage bias and measuring current is the experiment of interest, and there has been considerable activity in applying bias to ferroelectric materials. Firstly, because of the potential for devices based on the properties of domain walls and domain switching, and secondly, at least in part, because domain polarization provides clear contrast in TEM.

The earliest studies employing in situ TEM biasing for study of ferroelectric switching began in the 1980s on $Gd_2(MoO_4)_8$single crystals, carried out by Yamamoto *et al.*[80]. These early studies were soon followed by the work of Snoeck *et al.* who examined ferroelectric and ferroelastic domain wall motions in $BaTiO_3$ single crystals in plan (top-down) view[81]. Studies on polycrystalline PZT and PZST were carried out by Tan *et al.* who were able to observe the effect of repeated electrical cycling on intragranular crack growth[82, 83]. In separate works they reported the formation of small cavities behind the crack tip in PZT during electrical cycling, domain growth[84], and domain nucleation at grain boundaries with Qu and Zhao *et al.*[85].More recently, Sato *et al.* observed nanoscale non-180° domain walls (DWs) in lead magnesium niobate–lead titanate (PMN-PT) single crystals[86], demonstrating that a mechanism for ferroelectric switching,

beginning with reorientation of nano-domains followed by only small motions of the larger domain boundaries. In a similar fashion, Winkler *et al.* investigated the domain nucleation, propagation, and switching in $BiFeO_3$[86-88].This work used BFO samples cut from bulk crystals by focused ion beam methods, and were able to directly image domain collisions, repulsion, and other interactions in a plane view sample. A dependence of the domain relaxation rates on the applied bias was described and phenomena such as defect pinning, nucleation of new domains at defects were observed. Finally, the potential for atomic resolution time-resolved switching studies using *in-situ* TEM have been discussed by several of the previously mentioned authors. All of this illustrates the utility of *in-situ* TEM biasing for studying these materials, and further, the great potential utility of these techniques.

All of the work mentioned above was done in bulk materials rather than thin films. Very recently, direct characterization of ferroelectric switching in thin-film heterostructures became possible with the integration of a movable or scanning probe and TEM sample holders. For example Chang H. *et al.* watched domains grow induced by local electric fields in $BiFeO_3/DyScO_3$ without a bottom electrode[89]. While Zhang *et al*. studied the transition between tetragonal- and rhombohedral-like phases in highly strained $BiFeO_3$ on $LaAlO_3$ substrate, using PFM for electronic switching and *in-situ* TEM for mechanical switching such that the structure change could be seen in cross section[90]. The application of high strain *in-situ* was found to induce the phase transition from the tetragonal (T) to the rhombohedral (R) phase in BFO, as shown clearly through electron diffraction measurements, with a return to the T phase upon the release of strain.

In a thin-film heterostructure of $BiFeO_3/LaSrMnO_3/TbScO_3$ on (TSO) substrates, Nelson *et al.* studied the domain nucleation dynamics during switching[91]. Their work showed nucleation occurred only near the back electrode, which was attributed to the built-in field of the heterostructure. Gao *et al.* was able to capture interface nucleation and dislocation pinning effects in $PZT/SrRuO_3/DyScO_3$[92], as well as domain wall relaxation and subsequent disappearance of the switched domain [93]with ~40ms time resolution. The ability to capture these dynamic processes with high time resolution is one of the greatest potential assets for these types of in-situ experiments. However, while considerable work has been done by Nelson *et al.*, Gao *et al.*, Li *et al.*[51, 91-94], *etc.* using an *in-situ* holder from NanoFactory AB, which is no longer commercially available; there is currently no commercial platform that successfully combines a nanoscale scanning electrical probe with *in-situ* TEM. In addition, in order to study the photovoltaic effect in materials such as BFO, optical and other inputs are required. For these reasons, a component of this work was dedicated to the design of an improved system to continue these studies consisting of a multifunctional TEM holder capable of nanoprobe electronic measurements and optical input and measurement on a double-tilt stage accommodating standard sample geometries. Results derived from the older NanoFactory system, as well as the new design, are discussed in Chapter 6.

2.3 High resolution Transmission Electron Microscopy

The greatest asset of TEM microscopy methods is the ability to resolve atomic scale detail. It has been applied extensively to observe structure and defect details in crystalline materials. In this work, high resolution methods were used extensively to examine the details of domain walls in BFO, and even to map the polarization through direct

observation of the atomic displacements derived from atomic-scale imaging. STEM imaging in particular has proven useful in order to extract detailed information about polarization, largely due to the advent of aberration correctors in STEM. Aberration correction in conventional TEM imaging remains much less available at this point in time.

Historically, early attempts to calculate and map atomic displacements used phase information from HREM images, where the technique was used to show the displacement across a domain boundary in PZT[95]. This illustrates the ability to directly measure the domain boundary width, as well as accurately characterize the change in polarity at an atomic scale near the boundary. For instance, Jia *et al.* was able to map the polarization distribution unit-cell by unit-cell and show how the interfaces[96], dislocations [97] and domain boundaries [98] influence the dipoles. Nelson *et al.* was able to prove the existence of flux-completion vortex domains in BFO on TSO thin films, and map the polarization around the vortex domain with atomic detail [99]. Jia *et al.* observed similar flux-closure domains in PZT[100]. The polarization across the interfaces in BFO/LSMO/STO were mapped by Chang *et al.* using a similar methodology[101]. High resolution TEM was also used to map the evolution of modulated phases at the ferroelectric–antiferroelectric morphotropic phase boundary by Borisevich[102]and Lubk *et al.* used Gaussian-fit HAADF images and image simulation to map the atomic displacements and demonstrate the existence of both sharp and diffuse domain boundaries in BFO[103]. Similar observations have been made on nanoparticles, where Polking *et al.* were able to measure polarization even in a single BTO nanoparticle [104].

Clearly, high resolution TEM and STEM are indispensable tools to access atomic scale details and extract information about domains and defects in ferroelectric materials in particular. However, electron microscopy is not the only means available for imaging nanostructures, like domains. It has been a major theme in this work to use many independent approaches to imaging these materials, including scanning probe methods and Raman spectroscopy. These help corroborate the information collected at very small scales in TEM with more macroscopic measurements.

2.4 Piezoresponse and scanning force microscopy

Piezoresponse force microscopy is now widely employed to examine ferroelectric domains. In this method, an oscillating signal is applied to a conductive AFM probe. In a piezoelectric material, the sample responds with a mechanical change due to the converse piezoelectric effect, resulting in a change to the tip deflection. As the driving signal is AC, the response to the electrical signal will appear as a harmonic in the tip deflection signal. A lock-in amplifier is used to track the harmonic of the applied AC signal. The amplitude of the signal from the lock-in amplifier is related to the sample displacement and the phase angle between the applied signal and the response is related to the direction the sample moves with respect to the tip. Mathematically, this is described by[105]:

$$V_{tip} = V_{dc} + V_{ac}\cos(\omega t) \quad (1)$$

$$z = z_{dc} + A(\omega, V_{ac}, V_{dc})\cos(\omega t + \varphi) \quad (2)$$

$$z = d_{33}V_{dc} + d_{33}V_{ac}\cos(\omega t + \varphi) \quad (3)$$

Where V_{tip} is the total applied voltage, V_{dc} is the bias offset, V_{ac} is AC signal applied at some frequency ω, z is the sample displacement. The displacement is a function of the dc offset z_{dc}, the amplitude of the response A, and a phase angle φ, which can be simplified

for the out of plane direction with the piezoresponse coefficient d_{33}. The lock-in amplifier tracks φ and ω. The tip deflection, sample response, and the response of the lock in amplifier is represented schematically in Fig. 2.2. In addition to the out-of-plane component of the piezoresponse pictured, there may also an in-plane component, depending on the polarization vector in the material. The in-plane and out-of-plane movements can cross-talk, due to torsion on the cantilever. In order to correctly interpret PFM images, it is necessary to image the same area from several angles and observe the contrast[106, 107].

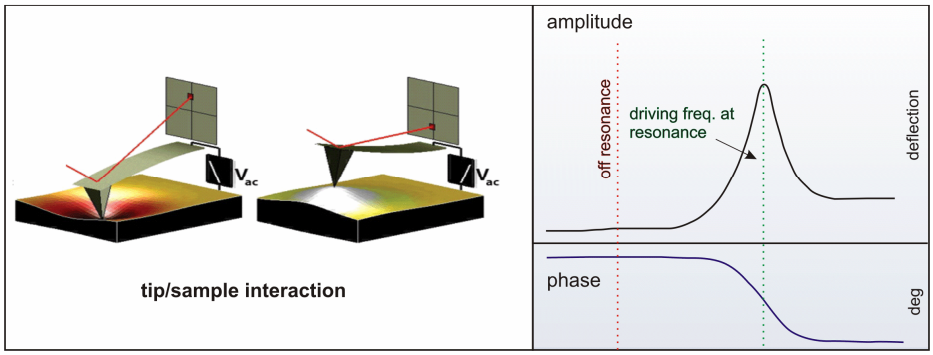

Figure 2.2 Piezoresponse force microscopy. The sample responds to the oscillating voltage at the tip. The right panel shows an idealized version of the displacement curves measured by the PFM lock-in

Historically, the force microscopy method that became piezoresponse force microscopy imaging (PFM)appeared in the literature around 1990 in a work by Saurenback and Terris[108]. Subsequently, the technique was adapted to map domains in many ferroelectric materials, including astriglycine sulfate, and barium titanate[109]. The technique was further refined by Kalinin and Bonnel in several papers[105, 109-112] and other authors[113-116]and, today, is the most popular and widespread means of performing nanoscale domain structure measurements on ferroelectric materials. Several recent papers examine the PFM technique, a review by Soergel describes the technique

and considers some of the challenges in interpreting PFM signals for obtaining quantitative results[117], while the review by Wang *et al.* examines in detail coupling problems between various signals in PFM[116].

The PFM technique is under active development and has been extended with several new methodologies designed to extract more quantitative information. An example is *in-situ* PFM studies carried out at high temperatures, where the decrease in the ferroelectric response near the curie point was examined[118]. Angular resolved PFM (AR-PFM), described by Park *et al.*, allows accurate mapping of the polarization vectors by eliminating contrast from crosstalk though careful analysis of the phase and amplitude contrast as a function of angle[106, 107]. In this method, the sample is rotated with respect to the cantilever through a series of angles and the contrast changes depending on the sample piezoresponse with respect to the cantilever axis, allowing disambiguation of the polarization vectors. Switching spectroscopy PFM (SS-PFM) is a point technique that takes an current-voltage curve at a single location and the phase signal is plotted against the applied field to generate a hysteresis loop of sorts[15, 119, 120]. A map of hysteresis loops can then be performed, taking by sweeping a number of preprogrammed points in a grid across the sample. The hysteresis loop gives analogous information to macroscopic electronic measurements but from the nano-scale. A further development based upon SS-PFM is the band-excitation technique (BE SSPFM), where a complex 'chirp' signal is applied during the sweep and appropriate models are used to process the signal to improve the signal quality. A great deal of information is encoded on the BE SSPFM signal and the extraction of various responses from the signal is a topic currently under development[121, 122].Most commonly, it is used to extract hysteresis loops and

to map relative activation energy for switching, as in Jesse *et al.*, where BE SS-PFM is used to examine the nucleation of domains in PZT films with SRO bottom electrodes. Gruverman *et al.* has used a PFM-based method to measure time-resolved switching dynamics in capacitors[123, 124] using a stroboscopic method in which a switching pulse was timed to the cantilever motion, so that at each point in the cantilever travel, the sample was at the same time position of its switching cycle. Using many switching cycles and assuming that switching occurs in the same way over each cycle, it is possible to construct a time-switching history of the nanocapacitor. However, the assumption that the details of switching do not change over the number of cycles required for imaging limits this methods applicability due to fatigue processes that are known to occur in ferroelectric materials. In addition to the PFM techniques, other well-known scanning probe methods are often applied over the same area and correlated with the PFM information to extract such information as leakage current via conductive AFM (CAFM), or surface potential via Kevin probe (KPFM); in this way the DC conductivity and bound charge associated with domain structures can be detected. Modern scanning probe methods, indeed, attempt to incorporate as many signals as possible over the same area in order to correlate as much information as possible. The scanning probe based characterization techniques are clearly developing very rapidly.

There are several drawbacks to the SPM based domain imaging techniques. Perhaps the largest is the difficulty in obtaining quantitative measurements as the exact geometry of the tip is not known. The size of the electrical contact, for instance, changes with time and tip wear, which alters the current or voltage values measured. Another issue is time resolution. The scanning rate in all SPM is relatively slow, typically a few hertz, resulting

in several minutes per image. The only exceptions being the stroboscopic method mentioned above. Although the next-generation AFM systems are all capable of somewhat higher scan rates, they are unlikely ever to match the 24 frames per second of ordinary video recording. Finally, there is the difficulty of atmospheric control. Unless the system is in ultra-high vacuum, a layer of adsorbates on the surface affects the tip contact characteristics[125].

2.5 Raman spectroscopy of inorganic materials

An alternative method of examining very small structural differences in crystals is by the use of optical spectroscopy techniques. In particular, Raman spectroscopy is sensitive to very small periodic distortions in a crystalline material. While Raman spectroscopy has been applied to organic and biological materials to examine molecular vibrations, it has also shown considerable utility for inorganic materials. It is particularly sensitive to small distortions in bond length and has been exploited to measure changes is chemistry such as doping and strain in both silicon [126]and oxide materials, for measuring temperature[127], and for tracking small chemical variations in geological specimens[128]. It is also widely used to fingerprint phases[129], in much the same way as XRD. Recently, it has become possible to calculate peak positions of the Raman spectrum for any crystal through first principals calculations based on density functional theory (DFT)[130-132]. The theoretical spectrum for a perfect crystal can then be compared in detail to an experimental spectrum to analyze the differences. A detailed description is included in Chapter 6.

The Raman effect arises from the polarizability of a bond. The incoming optical wave interacts with a local phonon state, scattering off the phonon. This means that the

induced electrical moment from the light exchanges a small quantity of energy with the crystal lattice, resulting in an energy change for the scattered photon. The photon can either gain energy from the crystal (anti-stokes scattering) or, much more commonly, lose it (stokes scattering). The amount of energy is controlled by the interaction between the phonon and the photon, and will have a particular value. If these photons are collected and elastically scattered photons filtered out, the Raman spectrum is what remains. So, the polarizability depends on the phonon wavevector:

$$Q_i = A_j \exp\left[\pm i\left(q_j \cdot r - \omega_i t\right)\right] \tag{4}$$

and the incident electric field.

$$E_0 \exp\left[i(k_i \cdot r - \omega_i t\right] \tag{5}$$

This results in a polarizability:

$$P = \varepsilon_0 \chi_0 \cdot E_0 \exp\left[i(k_i \cdot r - \omega_i t)\right] + \varepsilon_0 E_0 \left(\frac{\partial \chi}{\partial Q_j}\right)_0 A_j \times \exp\left[-i\left(\omega_i \pm \omega_j\right)t\right] \exp\left(i(k_i \pm q_j) \cdot r\right] \tag{6}$$

For three dimensions, the polarizability becomes a rank 2 tensor[133]:

$$\begin{bmatrix} P_x \\ P_y \\ P_z \end{bmatrix} = \begin{pmatrix} \alpha_{xx} & \alpha_{xy} & \alpha_{xz} \\ \alpha_{yx} & \alpha_{yy} & \alpha_{yz} \\ \alpha_{zx} & \alpha_{zy} & \alpha_{zz} \end{pmatrix} \begin{bmatrix} E_x \\ E_y \\ E_z \end{bmatrix} \tag{7}$$

Where if there is a change in any α results in the appearance of a Raman peak.

Furthermore, the scattering intensity of any peak has been shown to depend on the polarization of the input light with respect to the Raman tensors[134]:

$$S(e_l, e_s) = c \sum_j \int \left|e_l R_j e_s\right|^2 d\Omega_s \tag{8}$$

Where e_l and e_s refer to the polarizations of the input and scattered light. By measuring the change in intensity of the peaks over a range of angles, it is possible to correlate

changes in a Raman mode to the crystallographic orientation of the specimen. Then, by comparison of Raman spectra, or in an in-situ experiment, use the intensity to examine for one example distortions in the crystal. This has immediate application as a probe to observe changes *in-situ* in batteries, and similar situations where the crystal lattice changes are important. Additionally, the small variations in crystal distortions involved in ferroelectric domain walls are accessible by this technique[135].

2.6 Sample preparation

Thin film specimens for the materials studied here were obtained from several different sources. Titanium oxide films were grown by PLD in-house, while BFO thin film samples were obtained from collaborators.

2.6.1 TiO_2(B) films

All TiO_2(B) films were grown by pulsed laser deposition (PLD) on (100) Si substrates pre-deposited with a 20-unit-cell-thick STO buffer layer grown by molecular beam epitaxy (MBE), as described elsewhere[136]. The ~50 nm thick Ca:TiO_2(B) ($CaTi_5O_{11}$) template layer was deposited from a $CaTi_4O_9$ target made by mixing 80% TiO_2 and 20% CaO powders and dry pressing them into a green body, which was then sintered at 1400 °C. The TiO_2(B) layer was deposited on the Ca:TiO_2(B) template from a pure TiO2 target. The vacuum chamber used for PLD had a base pressure $<10^{-7}$Torr. A 248 nm KrF excimer laser with a pulse duration of 22 ns and a fluence of ~3.4 J/cm^2 was used at a 10 Hz pulse repetition rate for film deposition. The substrate-target distance was 6.35 cm and deposition was carried out at 800 °C in an ambient oxygen pressure of 0.05 Torr. The deposition rate was ~0.01-0.02 Å/pulse. The films studied in this work had thicknesses of 50-200 nm, as measured by a Veeco/Dektak profilometer and via TEM.

2.6.2 BFO films

The BFO films used in this work were obtained from our collaborators, Dr. Darrel Schlom's group at Cornell University. The majority of the films were grown on the $(110)_O$ face of a single crystal $TbScO_3$(TSO) substrate, with the exception of the strain series examined in chapter 5. MBE was carried out in an EPI 930 MBE chamber equipped with a reflection high-energy electron diffraction (RHEED) device. The Fe flux was approximately $2.0x10^{13}$ atoms/(cm^2·s) and the Bi flux was $1.1x10^{14}$ atoms/(cm^2·m). During the deposition, distilled ozone (~80% ozone) was used to create a background oxidant pressure of 10^{-9}Torr. The substrate was maintained at a constant temperature of 610 °C for growth directly on the $(110)_O$ $TbScO_3$ substrate.

In thin films grown on low-misfit orthoscandate substrates, BFO forms highly regular striped domain arrays composed of predominantly one domain type[137]. In this work, except where noted, BFO thin films were prepared on $TbScO_3$substrates. The lattice misfit calculated for the pseudocubic TSO lattice is -0.1266% in $[100]_p$ and -0.1389% in $[010]_p$ where $[001]_p$ || $[110]_O$-TSO, $[100]_p$ || $[-110]_O$-TSO, and $[010]_p$ || $[001]_O$-TSO. The mismatch breaks the degeneracy of the four ferroelastic polarization variants, limiting the displacements to r1 and r4 domains, pictured in Fig. 1.2, on TSO substrates[137].

2.6.3 TEM and PFM sample preparation

For any imaging technique, the quality of sample preparation is key. Each technique has specific requirements of the geometry, arrangement, and properties of the sample being probed. A great deal of effort is put into high-quality processing of samples for application of various microscopic techniques.

For TEM, materials to be sampled are used in very small pieces, generally starting as a 3mm disk. A portion of the sample must then be thinned to electron transparency, ideally thin enough such that an electron will only scatter once within the specimen. For most metal or semiconductor materials, this length is less than 100 nm at an accelerating voltage of 100keV[71]. In high-resolution work, the thinner the sample the better the expected result is. Additionally, the surface must be smooth, and free of contamination such as adsorbed organics, water, solvents, or similar substances. The sample preparation process used for these specimens involves protecting the film by gluing to sacrificial silicon, mounting in hot wax and polishing to less than 1µm at the thin end of a wedge-shaped sample, and ion milling until the film is exposed. Such samples are regarded to be exceedingly fragile, and difficult to handle.

For scanning probe methods, the constraints on the sample are not nearly as great. PFM, biasing, conductivity, and related electrical measurements can all be made under ambient conditions with the greatest requirement being that the surface must be clean and flat. In addition to being clean, the surface must also be very smooth. Even a mirror-like polish leaves significant nanometer-level scratches that degrade the image. Also, there is a small force applied by the tip to the sample, which the sample must be strong enough to support. Otherwise the sample will be scratched, or broken. The applied force depends on the dimensions and modulus of the cantilever. For a 225 µm long Si cantilever, the force usually falls in the range of a few piconewtons. As PFM is a contact mode method, softer cantilevers are generally used. However, cantilevers for contact mode are typically very long and have poor resonance characteristics as the long, soft cantilever supports complex vibration modes, which may disrupt the PFM signal. For PFM, an intermediate

tip length (referred to as FE or FM tips such as the SCM-PIT model from Bruker) is used as a compromise between good resonance and low applied force. Most oxide films are sufficiently robust for direct probing of the film surface, but there are complications for cross sectional samples. It is difficult to meet requirements for smoothness and lack of contamination in polished cross-sections. Also, for a cross section, the sample must be contiguous as anyhole, edge, or large particle from polishing will cause a tip crash. Here, cross section specimens were prepared using TEM methods, *i.e.* mechanical polishing followed by ion milling. The ion milling step in vacuum removes most organic and inorganic contaminants and provides a very smooth surface. This comes at the cost of introducing a thin amorphous layer over the surface, but this was not found to impede imaging. The sample preparation process is illustrated in Fig 2.3.

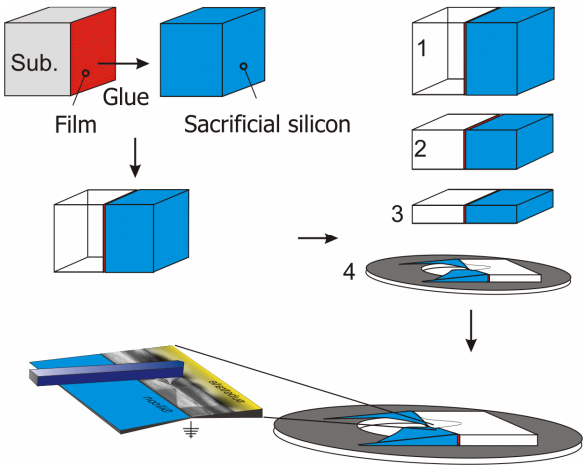

Figure 2.3 TEM/PFM cross sectional sample preparation. Above is a schematic of sample prep where the film is glued to a sacrificial Si piece to protect it during polishing, thinned mechanically as a wedge, then glued to a Mo support ring and ion-milled to electron transparency. The sequence one through 4 indicates mechanical thinning of the sample, which is finally mounted on a Mo disk and ion milled until a region of the film becomes electron transparent.

Both TEM and SPM microscopy methods require clean, flat specimens with little contamination. It would seem reasonable, then, that both techniques can be successfully applied to the same specimen. Though the thinnest region of TEM specimens is best

avoided, a great deal of accessible cross section remains in the region of the sample that is too thick for electron transparency. If PFM is attempted in the thin regions of the sample, care must be taken where the film is exposed and it is possible for the SPM tip to run off the edge or punch through the sample. Here, most specimens prepared for TEM were found to be amenable to SPM measurements as well, and this technique was utilized extensively in this work.

Chapter 3

The influence of crystal defects on domain orientation in $BiFeO_3$

3.1 Background

$BiFeO_3$ has received a great deal of attention due to its large ferroelectric polarization, and multiferroic properties. Applications in ferroelectric computer memories[30], ferroelectric tunnel junction devices[35], memristor devices[36], devices exploiting coupling between ferroelectric and magnetic properties including spintronics applications [37-39], and new possibilities for domain-wall based microelectronics[40] have been considered. The utility of BFO for these applications depends strongly on the formation of domain structures in the material.

Phase field and experimental work in the literature have shown that domain structures in single-crystal ferroelectrics depends sensitively on the energetic balance between internal built-in fields, epitaxial strains, and the depolarization field[37, 138-141]. Similarly, several studies have explored the effect of interfacial effects[139, 140], and film thickness[142], indicating strong effects from substrate clamping and internal fields on domain stability. Large interfaces, such as the top and bottom interfaces of a thin film, therefore are able to substantially alter the domain structures in thin films. Any extended interface, then has the potential to determine domain structure.

There have been a considerable number of studies examining the interactions of various types of crystal defects on ferroelectric domains. Work with BFO powders has indicated

that defects, particularly grain boundaries, can alter domain structures, where a decrease in the particle size causes the particulates to become monodomain and eventually suppresses the ferroelectric properties altogether as the grain boundaries become a significant influence on the total polarization.[143, 144] In thin films, the effects of other types of defects have been shown to have small effects on the domain structure. Particularly, dislocations[145], preexisting domain walls[146-148], and oxygen vacancies[149] have all been show to pin the location of domain walls. There are few instances, however, where an extended defect has a direct influence on the polarization of domain walls that surround it. In PZT grown on bicrystal substrates, it has been shown that the preferred local polarization is influenced by the existence of the boundary[150]. In other words, the boundary selects for a certain domain type. In another case, the existence of a charged domain boundary produces a thin transition zone of random polarization a few atomic layers thick near that boundary, something like a polarization glass.[147]. It is clear, then, that domain boundaries and defects have an effect on polarization in ferroelectrics on a local scale. In this work, we show that extended charged defects can alter the entire domain structure through a distance greater than the average domain size, on the order of<100 nm.

In the present work, an extended layer of defects stabilizes a mixed structure of 109° and 71° domain walls extending through the thickness of a ~500nm thick film. Close examination of the defects indicates both charge and strain originating from the defect is the mechanism influencing the domain wall orientation. This agrees well with phase field models referenced here. Since the mechanisms of strain and charge on domain

structures and the common defect types are generally present in all perovskite ferroelectric materials, this mechanism may be applicable to all perovskite ferroelectrics.

3.2 Experimental Methods

For this work, $BiFeO_3$ films were grown on single crystal $(110)_O$ $TbScO_3$ surfaces by reactive-molecular beam epitaxy (MBE) in an EPI 930 MBE chamber equipped with a reflection high-energy electron diffraction (RHEED) device. The Fe flux was approximately $2.0x10^{13}$ atoms/(cm^2·s) and the Bi flux was $1.1x10^{14}$ atoms/(cm^2·s). During the deposition, distilled ozone (~80%ozone) was used to create a background oxidant pressure of 10^{-9}Torr. The substrate was maintained at a constant temperature of 610 °C for growth directly on the $(110)_O$ $TbScO_3$ substrate.

A combination of TEM and PFM techniques were used to examine these structures, and without both the unique domain structure would never have been visible. The first method used is transmission electron microscopy, where dark-field imaging was carried out on a JEOL 3011 at 300kV and provided clear domain contrast, while STEM imaging was captured using a spherical aberration (Cs) corrected FEI Titan 80-300 operated at 300 kV providing a point-to-point resolution of 0.05 nm (at LBNL). Atomic resolution images may also be used to directly measure polarization information, with appropriate software and processing as described in chapter 2.

The second method of imaging ferroelectric domains is piezoresponse force microscopy, a surface-probe based method which can, in principle, distinguish in-plane and out-of-plane components of the polarization, but it is often difficult to unambiguously distinguish between domain structures from the top surface, as there many confounding effects [151]. More information is available from the film cross-

section, but such samples are difficult to prepare and there are only a few examples in literature [87, 152]. This is unfortunate, as without access to the cross section, there is no information available on structures beneath the surface of the film. In this work, PFM analysis was carried out with an NT-MDT Spectra SPM, and a Bruker Dimension Icon using platinum-coated silicon cantilevers on cross-sectional specimens. A schematic depicting the specimens used is included in Fig. 3.1.

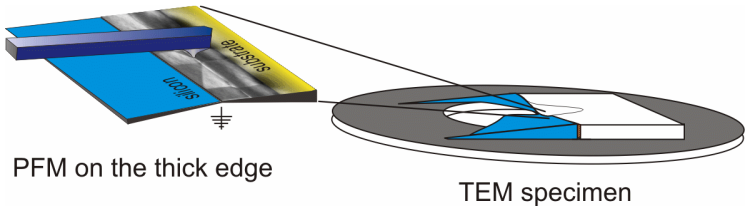

Figure 3.1 Schematic depicting the application of PFM to TEM specimens. The tip is able to scan the thicker region of the specimen, from the electron transparent region to much thicker regions along the interface of a cross-sectional sample.

There are benefits and drawbacks to both techniques. TEM requires preparation of very thin specimens, and there have been questions concerning the stability of domain structures when preparing specimens. The combination of PFM techniques and TEM on the same specimen avoids this problem, where areas greater than 1 µm in thickness can be examined in line with the 30 nm thick sections visible in TEM, and also allows disambiguation of the polarization through a combination of PFM contrast and direct mapping of the polarization in atomic resolution images. The defects and defect structures were analyzed by TEM and compared directly to domain structure information from both dark field and PFM methods.

3.3 Results and Discussion

PFM and TEM showing mapping of the domain structure of a cross-sectional specimen of a ~500nm BFO cross sectional TEM specimen are shown in Fig. 3.2. The exposed

cross section was mapped from an area ~2-3 μm thick almost to the electron transparent region, and through the electron transparent region by TEM. The figure shows a collection of images captured at evenly spaced intervals across the indicated region. An unusual domain structure was observed, with a strong transition between domain types, from 109° to 71°, occurring about 100 nm from the back interface. Though there is some variation in the domain structure across the cross-section, the 109° structure at the interface is present everywhere. Fig. 3.3 gives top-down and cross sectional information from the film. From the top down, the domains appear striped as is relatively normal in these BFO films. The stripes are relatively wider than would be normal for a 109° domain structure. Close ups of the cross section, in panels B and C, show an unexpected domain structure. The images are out-of-plane PFM amplitudes from a film cross section collected with the tip axis parallel, and at a 35° angle to the film. The relationship between the tip axis and the specimen are shown by the white arrows. The contrast variation is indicative of the polarization of the domains[153] and suggests that near the substrate interface to ~100nm from the interface, a 109° domain structure prevails. Above this, much wider 71° domains extend to the surface. In between these two layers, there should be an unfavorable highly charged boundary due to the change in polarization.

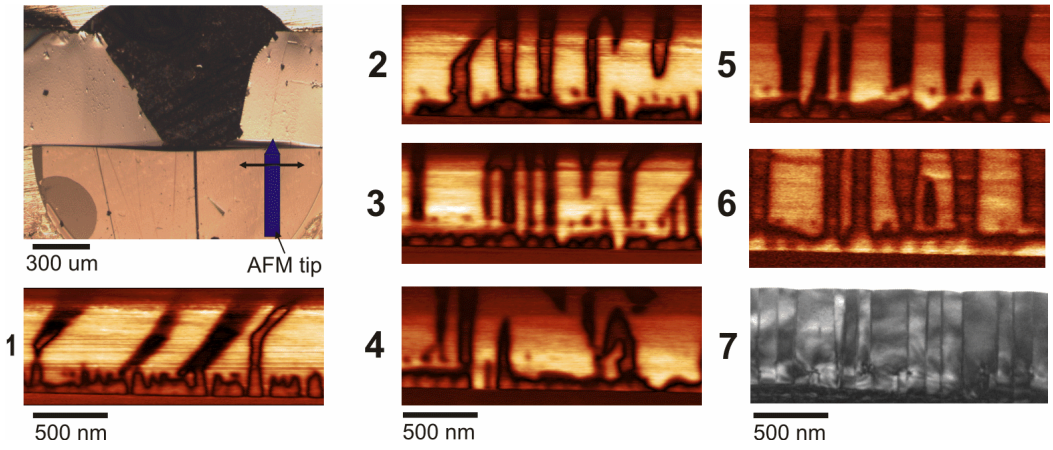

Figure 3.2 Cross-sectional PFM and TEM map of specimen .The figure shows PFM (panels 1-6) and a TEM image (7) taken from the same polished TEM specimen, also pictured. The area from which the images were taken is shown by the AFM tip schematic.T Surveying the film by PFM as well as TEM shows reveals a complex domain structure consisting of two layers. A thin layer between the interface extending ~100 nm into the films, and a second layer with a much sparser set of domains containing many with inclined domain walls.

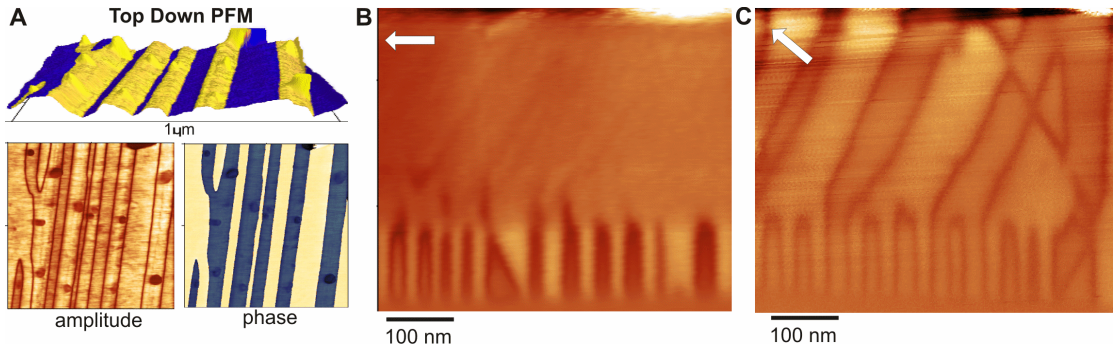

Figure 3.3 PFM mapping of domains . Panel (A) shows top-down PFM of the film. (B) PFM image of the film cross section where the 109° domains at the bottom interface show optimal contrast when the tip axis is aligned scanned parallel to the film (white arrow). Panel (C) shows the same area with the sample rotated 45° with respect to the tip axis, clearly showing the in-plane character of the polarization in the top layer. This indicates the bottom domains are 109°, while the top are 71° domains.

Examining this interface much more closely in TEM in Fig. 3.4, at the top of each 109° domain, a crystalline defect was found. These defects are poorly visible in regular resolution TEM and not visible in PFM as the spatial resolution is typically insufficient and the technique only accesses the surface of the sample, which is damaged by cross-

sectional sample preparation. Initial imaging by TEM also showed mostly 109° domains extending to the surface, as this technique surveys a much smaller portion of the available sample area. To see these domain structures, a combination of both techniques were required. This underscores the importance of applying many techniques to the same samples.

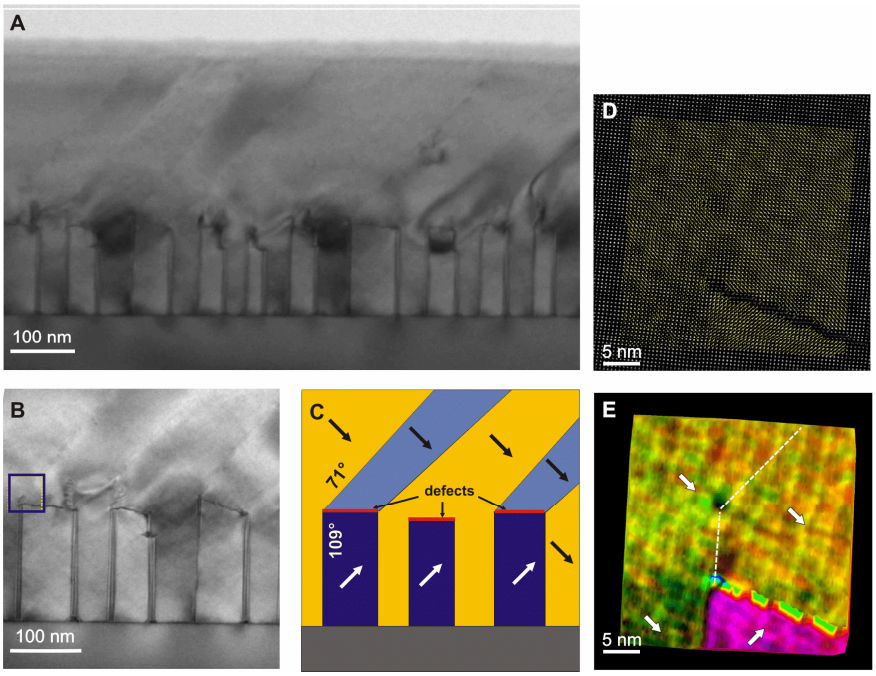

Figure 3.4 Defect-stabilized domain structure. (A) Bright field STEM image showing the domains and the layer of linear defects in the film (B) shows a close up of the bottom layer of domains, showing them to terminate at a long linear defect. (C) is a schematic of the domain structure showing the polarization, where the head to head intersection of the polarization vectors indicates the defects are negatively charged. (D) and (E) show a high resolution image of the corner of the defect indicated in panel (B), and a map of the polarization around the defect, respectively.

Knowing the existence of the unusual domain structure, it is possible to examine the domain interface using atomic resolution HAADF STEM images, where the defects can be clearly seen. Such information can be extracted from the HAADF image in Fig. 3.4D, which is overlain with the vector map of the polarization. The defects are atomic-scale in width, only approximately one unit cell across. The linear defects consist of a Bi-poor

iron rich region where every other Bi column is missing. This can be clearly seen in Fig. 3.5D. This type of structure has been described in literature[154, 155], where these defects are shown to be relatively common occurrences in BFO thin films, and electrically charged. In general, defects have been shown to strongly influence domain structure and ferroelectric properties. Charged defects, such as vacancies, interact strongly with domain walls, resulting in domain wall pinning, and stabilizing complex domain structures[156, 157]. Extended defects such as dislocations can attract and pin domain walls and stabilize charged domain walls. It is reasonable that these charged defects may provide a mechanism for the formation of this mixed 109° and 71° domain structure.

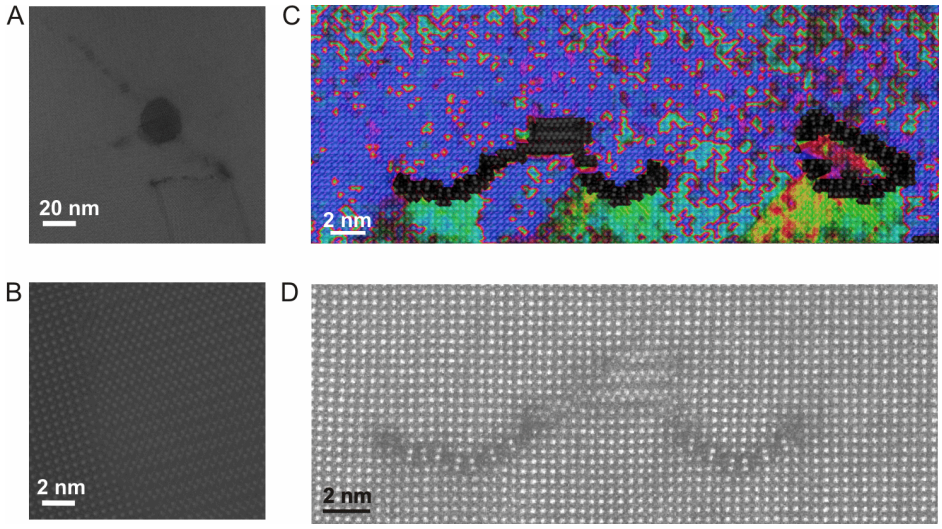

Figure 3.5 Details of extended defect structure The linear defects are associated with particles of a precipitate. (A) shows such a precipitate associated with a long defect and (B) is a high resolution HAADF image of the area indicated in (A) showing the distinct layered structure of the precipitate. (C) polarization mapping of the area around such a defect shows a very strong effect on the polarization of the BFO below the defect but little above it. (D) shows a HAADF image where the intersection between the particle and the defect is clear.

The charged domains affect the local electric field, and determine the termination of the surrounding domains of polarization. Polarization mapping of the atomic resolution

images, shown in Fig. 3.4E supports several details of this argument. First, that our assignments for the domain types are correct, and change across the defect. Secondly, as seen in Fig. 3.5C mapping of similar defects near the bottom interface show the formation of nanodomains under the extended linear defects. This reinforces that the charge on the defect is sufficient to influence the polarization of the surrounding film.

The linear defects themselves appear to be related to small precipitate particles, as seen in Fig. 3.5. These resemble the precipitates described in a recent paper by Deniz *et al.*, which describes the discovery of a metastable layered phase in BFO thin films, described in detail in Ref.[158]. The precipitate is a metastable Bi_2FeO_6 compound where, as can be seen in the image in Fig. 3.5D, it appears as a stack containing 2 layers of Bi atoms with bright contrast, followed by a layer of lower-contrast Fe atoms. This precipitate phase is Bi-rich, while the defect is Bi-poor. This suggests that the Fe-rich step-like defects may be a related to the formation of a particle of the Bi-rich Bi_2FeO_6 phase.

Similar extended defects have been described in $(Bi_{0.85}Nd_{0.15})(Ti_{0.1}Fe_{0.9})O_3$, and shown to distort the charge, strain, and polarization on a local scale, which can induce large changes in the ferroelectric properties[159, 160]. Here, in undoped $BiFeO_3$, the defects appear to stabilize a 109° domain structure below them while screening the remainder of the film from the back interface, resulting in a split domain structure. Mapping of the ferroelectric polarization surrounding the defect in Fig. 3.5C shows a rotation in polarization towards the defect, and a slight increase in the c/a ratio, indicative of strain. However, above the defect, the polarization does not noticeably change. These defects, then, may screen the bulk of the film from the built-in field that exists due to the bottom interface. Further evidence that the defects stabilize the 109° domains is provided in Fig.

3.6 where in a 200 nm thick BFO film, a similar layer of defects stabilizes a 109° structure, while a defect-free 200 nm film shows a stable 71° structure. The reasons for the appearance of the 71° structure in that film is discussed in detail in the next chapter.

In the film with defects, the domain structure atop the defect-stabilized 109° domains is somewhat unclear. On very close examination, a few area containing clear inclined (likely 71°) and vertical (109°) domain walls can be found, as in the thicker 400 nm thick sample, but in general it is hard to distinguish a clear domain structure. One such area is pictured in Fig. 3.6DThis may be a result of the proximity of the defect layer to the surface of the film. The defect layer falls between 100-150 nm towards the film surface from the bottom interface, leaving very little defect-free film on top of the defect-stabilized layer. This may effectively suppress the formation of twinned domain structure in the top layer of the film as the defect layer underneath is not entirely smooth and does not leave room for a twinned domain structure to form. In the case of the much thicker 400 nm films, there is a much larger quantity of defect-free film on top of the defect layer in which a domain structure may form, resulting in the 'split' domain structure that was observed in the thicker sample.

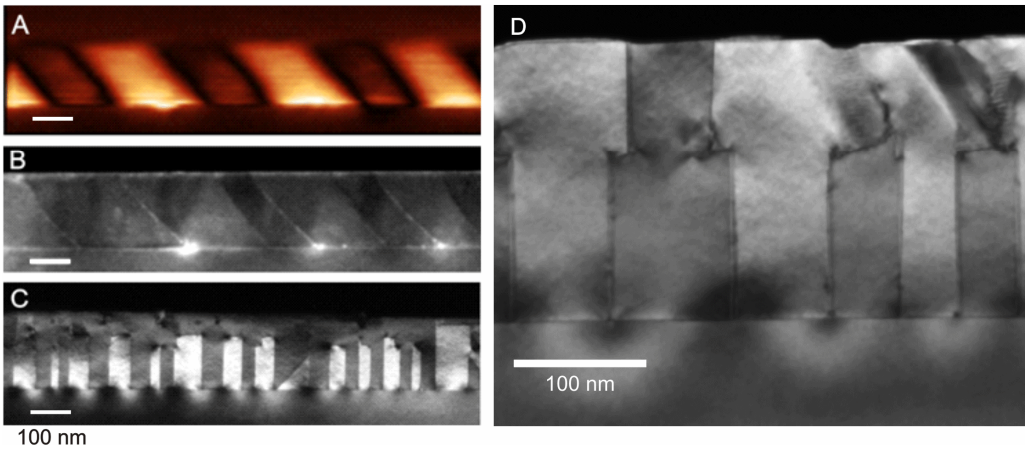

Figure 3.6 Comparison to defect-free films (A) cross-sectional PFM image of 200 nm BFO film from a thick specimen. (B) TEM from the thin area of the same specimen shows the same 71° domain structure. (C) Dark field TEM image of a 200nm film with defects, showing a 109° domain structure beneath the defect layer. (D) shows a closer view of another area of the film where domains are visible in the top layer, and similar to those seen in the 400nm film.

3.4 Summary

In this chapter, it is demonstrated that defects that can be added during film growth directly stabilize otherwise unstable domain structures, allowing the creation of charged domain boundaries and control of domain patterns in BFO thin films. A 2-D layer of charged defects was introduced into a 500nm thick BFO film during thin film growth by MBE resulting in a long-range alteration of the domain orientation. These were detected and examined using a combination of PFM, TEM, and atomic resolution STEM imaging over the entire cross section of the samples. The defects themselves are shown to be similar to those observed by Maclaren *et al.*[154, 155], in which a bismuth layer is missing, resulting in a 2-D iron rich layer. These defects are known to be charged [155]. This produces a change in domain structure through the thickness of the film, with 71° domains forming directly on top of 109° domains. This structure would ordinarily not be stable due to the charged boundary between the 109° and the 71°, but is stabilized by the charged defect. Mapping of the ferroelectric polarization, achieved using computer

processing of the STEM image, clear changes in the polarization in the BFO underneath the linear step-like defects. While there is much work in the literature that has shown that charged domain walls and dislocations affect the local polarization, these effects fade away rapidly within a few unit cells distance from the defect. A defect that influences domain structures extending over 100 nm away observed in this work has not previously been described. The linear defects here are associated with precipitate particles, that have been described in literature[158], and likely result from depletion of Bi in BFO in order to make the Bi-rich layered precipitate. This structure is interesting from both a scientific and a device-application standpoint. From a scientific perspective, switching though such layered structures has not been examined and there are many questions concerning how moving domain walls will interact with the defects themselves, and the intersection of 109° and 71° domain walls. Also, it gives an excellent opportunity to examine the unusual electronic properties of charged domain walls, such as metallic conductivity[5, 40, 49], which are otherwise rare as they tend to be thermodynamically unstable. From a device standpoint, the coexistence of two layers of different domain types would allow multi-bit memory cells if they can be switched independently. For domain-wall nanoelectronic devices, it will be necessary to reproducibly control the formation of stable domain walls, and applying defects as seen here may be a viable means to make that possible.

Chapter 4

The influence of film thickness on domain structure and switching in $BiFeO_3$

4.1 Background

The preferred domain orientation in a ferroelectric has a strong influence on its useful properties. In rhombohedral ferroelectrics such as BFO, there are three different domain wall types, resulting in multiple different domain structures. The surface charge, domain wall properties and energies, and multiferroic properties all depend on the type of domain ordering, as was discussed in chapter 2. Apart from utilizing charged defects to alter domain structures explored in the previous chapter, another approach to affecting domain wall formation by altering the charge balance in BFO thin films is to change the film thickness. This is a result of the depolarization field that forms internally due to the charge displacement in the ferroelectric. A structure composed of 71° domain walls hasa fixed out-of-plane component, resulting in a strong surface charge, and consequently a strong depolarization field. These structures are depicted in Fig. 1.3in chapter 1. They have also been shown to have variable conductivity[57]. The 109° structure has an alternating out-of-plane polarization component which, on a large scale, negates the depolarizing field, and have been shown to have distinct electrical properties from other types[40]. A 180° domain wall contains the polarization vector, and therefore remain charge neutral, but may still be electrically conductive under the right circumstances[50].

180° domains also represent the largest displacement for piezoelectric applications. Each domain wall variant, and therefore, each structure will form depending on competition between internal fields, strain, and the depolarization field. Published phase field calculations from literature indicate that, in terms of energy, 109° have the lowest, followed by 71° and 180°[161], for thin films. However, the depolarization field, and internal fields depend on the film thickness due to screening and similar effects[162]. Strain may also change even without large numbers of dislocations if the film is thick enough.

The effects of film thickness on BFO have been approached both experimentally and theoretically in literature. An energy-based approach for modeling the change in properties in BFO thin films examine the change in the c-axis lattice parameter, the piezoelectric parameter d_{33}, polarization, and dielectric coefficient as a function of thickness[163]. All of these are shown to change drastically for very thin films, below 100 nm, but much less rapidly in thicker films. Experimentally, the piezoelectric parameters have been shown to decrease monotonically with thickness[164], though piezoelectric properties can still be measured with films down to 2nm in thickness[165]. In line with these results, sputtered films between 2 and 150 nm have been examined by PFM methods[165], losing the regular striped structure seen for thicker films, and becoming a blocky mosaic for films <15nm thick. Several studies have also examined the effect of film thickness on the magnetic properties of BFO [162, 166, 167], with the saturation magnetization of strained BFO on STO decreasing with increasing film thickness. While films up to 600nm were included in many studies, the focus was on the dramatic effects in the thinnest films. Effects of increasing thickness on domain type and

structure has not been addressed, but it is clear that though strain, depolarization fields, *etc.* change at a lower rate, the trend continues into much thicker films. For greater film thicknesses where strain and fields may be compensated, effects on the domain structures and switching processes have not been as well explored.

A combination of experimental methods was used to examine and unambiguously determine the domain structures of the films, including PFM, DF TEM imaging, atomic resolution HAADF STEM imaging and mapping. Here, the domain structure of BFO on insulating substrates is shown to be controlled by the film thickness, with uniform 109° striped domains in thinner films (50-100nm), and uniform 71° domains in thicker films (200nm). A transitional structure of mixed 109° and 71° domains was observed for thicknesses of 130nm. This property likely arises from the depolarization field, which decreases as the film thickness increases, as has been demonstrated through phase field modeling. Furthermore, even with the addition of a back electrode that should allow free carriers to compensate the depolarization field, there is a persistent difference in the switching mechanism, where both films switch easily in the out-of-plane direction, while thicker films repeatably switch both in-plane and out-of-plane. These results indicate that the switching mechanism can be altered simply by choosing an appropriate film thickness.

4.2 Experimental Methods

$BiFeO_3$ films were grown on single crystal $(110)_O$ $TbScO_3$ surfaces by reactive-molecular beam epitaxy (MBE) in an EPI 930 MBE chamber equipped with a reflection high-energy electron diffraction (RHEED) device. The '$_O$' subscript indicates orthorhombic indices. The Fe flux was approximately 2.0×10^{13} atoms/($cm^2 \cdot s$) and the Bi

flux was $1.1x10^{14}$ atoms/(cm^2·s). During the deposition, distilled ozone (~80% ozone) was used to create a background oxidant pressure of 1^{-10} Torr. The substrate was maintained at a constant temperature of 610 °C for growth directly on a $(110)_O$ $TbScO_3$ substrate. Cross-sectional samples were mechanically polished using diamond lapping film (South Bay Technologies Inc.) and then ion milled in a Gatan precision ion polishing system.

PFM analysis was carried out with an NT-MDT Spectra SPM, and a Bruker Dimension Icon using platinum-coated silicon cantilevers. The PFM images were captured near resonance both with the tip axis oriented along the film normal and along the film axis for comparison. HRTEM was carried out on a JEOL 3011 TEM at 300kV. Dark field images were tilted slightly off the zone axis and aligned in the two-beam condition (the diffracted beam is along the optic axis). Atomic resolution STEM images were captured using a spherical aberration (Cs) corrected FEI Titan 80-300 operated at 300 kV providing a point-to-point resolution of 0.05 nm (at LBNL). CS corrected Z-contrast images were acquired using a HAADF detector.

Image analysis for GPA was carried out using the FRWRtools plugin for Digital Micrograph™ and polarization mapping was carried out using the Matlab scripts created by C.T. Nelson, described previously.

4.3 Results and Discussion

Based only on the change in film thickness, the entire domain structure goes through a transformation between a 109°, a mixed 109° and 71°, and a pure 71° domain structure. In Fig 4.1, cross-sectional TEM images and PFM out of plane and in plane amplitude images collected from films with nominal thicknesses of 60, 100, 130 and 200 nm are

shown. For the ~60 nm film vertical 109° domains with slightly varying widths are evident, with a fairly high concentration of 180° domain walls. These are visible in both TEM and PFM images. In 100nm films, the domain structure is highly uniform, more so than the thinner film, also of 109° domains, with only a few extended 180° domain walls appearing in PFM analysis of the film. In contrast, for 200nm film thicknesses, PFM and TEM show a complete change to in-plane polarization and inclined domain walls, indicative of 71° domains. These are also uniform in size and extent through the film. Polarization mapping of HAADF STEM images and geometric phase analysis data in Fig. 4.2 supports the conclusion that the inclined domains are 71° as the projection of the [100] direction in BFO shows no contrast, as is expected for 71° domains, but not for 109° or 180°. Furthermore, geometric phase analysis indicates a strongly strained boundary, also indicative of a 71° domain wall.

At an intermediate thickness of 130 nm, the film contains both out-of-plane 109° regions, and orthogonal 71° in-plane regions. This can be clearly seen in the PFM images. The bright areas in the out of plane amplitude are areas of 71° domains. This is confirmed by the in-plane image where the broad stripes of the 71° domains show clear contrast. The darker areas are 109° domains, which is indicated by the width of the stripes within each dark area, and the weak contrast in the in-plane PFM image. Examining the same film in TEM, the cross-section shows both 109° domain walls, and a long bisecting domain, which is consistent with a 71° as this sample was cut parallel to the 71° domains and orthogonally to the 109° domains seen in the PFM images.

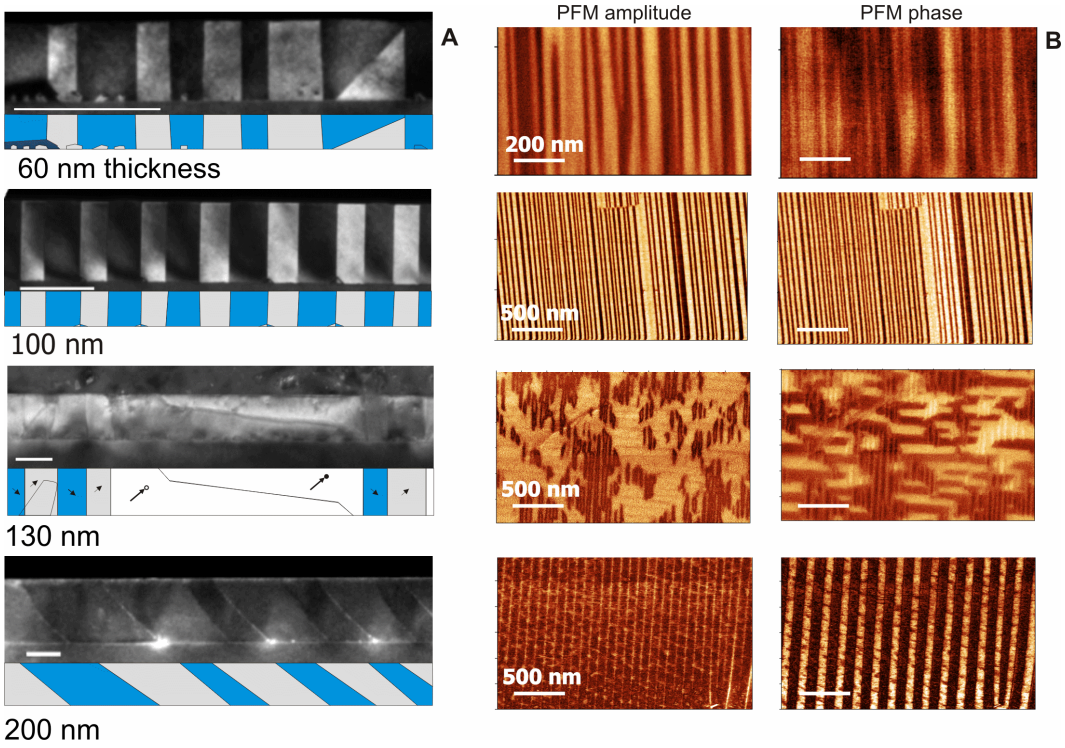

Figure 4.1 The change in domain pattern with thickness. (A) TEM of films at different thicknesses. The cross-sections corroborate the top-down PFM images and allows the domain wall types to be clearly identified. The scale bars are 100 nm in length (B) PFM of films of 50, 100, 130, and 200 nm films. The domain structure changes markedly as the film thickness changes.

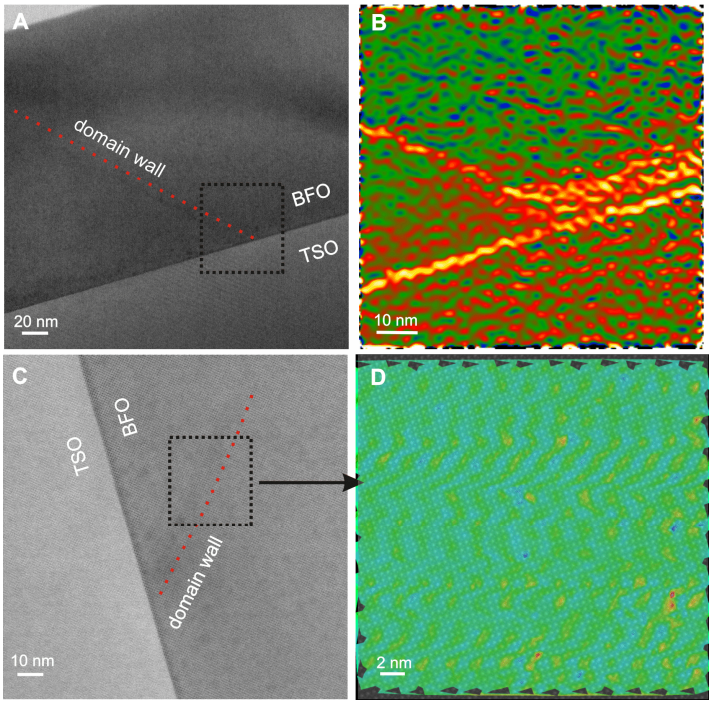

Figure 4.2 Proof of 71° domains (A) BF STEM image of the 200 nm thick film. The domain wall is marked by the red dotted line.(B) GPA analysis of strain in the x-direction where the bottom interface and domain wall are clearly strained. The bottom of the domain to the right of the domain wall also shows strain. (C) BF STEM image showing the, very faint, domain boundary (D) A STEM HAADF image from the indicated zone overlain by a polarization map. Polarization shows no change, which is consistent for a 71° wall viewed from this zone axis.

As noted previously, the prevalent domain type controls many of the important properties. Several papers have featured the 109° domain structures seen in the thinner films, and explored their properties [91, 93, 99, 168-170]. There are fewer examples of 71° structures and it is worthwhile to unambiguously confirm the existence of pure 71° domain structures in the thicker films. Fig. 4.3 shows BF and DF TEM images, and a PFM image of the cross section of 200 nm film specimens. The PFM image was taken from a very thick (>1mm) specimen and compares well with the TEM specimens. Capturing images from both thick and thin regions of samples by independent measurements allows us to eliminate the possibility that sample preparation and thinning for TEM alters the measured structures. Close examination of the 71° domain walls show

a slight curvature and higher contrast than would be expected for a single unit-cell thick domain wall. There is also evidence of alternating strains.

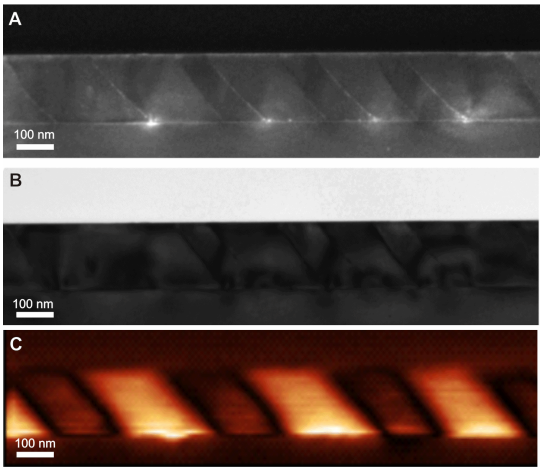

Figure 4.3 Cross section from 200 nm BFO film showing inclined 71° domains.(A), dark field TEM, (B) bright field TEM, and (C) PFM of a thicker cross-section showing that the 71° domain structure is not affected by TEM sample processing

From Figure 4.3, it appears the domain walls are slightly curved. This curvature may arise due to strain at the 71° domain boundary. These boundaries are flexoelectric and the polarization vector points into/out of the paper, resulting in a strain that causes buckling of the film at the base of every other domain, as is clearly seen in the bright field image in Figure 4.3B. This is corroborated by geometric phase analysis in Figure4.2.,which also shows a strain at the base of every other domain. The existence of this curvature and the clear evidence of strain confirms work in the literature indicating that the flexoelectric strain in 71° domain walls can change the character of the boundaries in BFO films[49].

Domain structures and film thickness are related in ferroelectrics by a simple relationship between domain width (and therefore domain wall concentration and total

energy) and thickness known as the Kittel scaling law[28], by analogy to magnetic materials. This approach compares the total energy in the film as it is distributed between internal fields, strain, and the energy of domain walls to find the equilibrium domain width. It is important to note, however, that this assumes that all of the domains are of one type, as different domain walls have different energies. The plot in Fig. 4.4 shows the film thickness against the square of the domain width, and the fit line for Kittel's law. To get ensure a correct fit, the domain wall type had to be determined, and all domains were confirmed to be 109° by combined TEM and PFM in order to generate this curve. The thicker films used to generate this curve, with a thickness <200nm, contained defects as discussed in the previous chapter which stabilized 109° domains. Otherwise, as seen in this chapter, 71° domain structures appear in films over 200nm in thickness. As can be seen from Fig. 4.4, the average domain width is much higher for a 71° domain structure than for a 109° structure. The difference in domain width is reasonable, as 71° domain walls are higher energy than 109° domain walls[161], This result underlines the importance of determining the domain type before attempting analysis of domain width, and also gives a means of determining the domain type from PFM measurements performed on the top surface of a thin film.

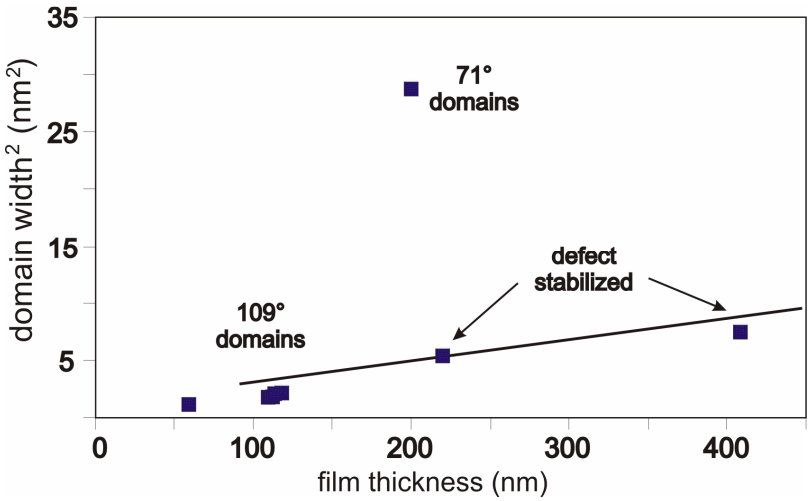

Figure 4.4 Plot of domain width squared against thickness. For samples with 109° domains, the fit to Kittel's law is good, while 71° domains are much broader. 'Defect stabilized' refers to 109° domains stabilized in thicker films by the defects discussed in chapter 3

To find a mechanism to explain the domain transition as a function of thickness, it is possible to use phase field simulations to examine the effect of specific variables on domain structures in ferroelectric material. A good match between simulation results and reality lends credence to considerations of the mechanism underlying the observed phenomena. To this end, the domain pattern of BFO was modeled using phase-field simulations based on the time-dependent Landau-Ginsberg equation. In-plane anisotropic strains of ε_{11} = -0.1%, ε_{22} = -1.0% and ε_{12} = 0% were applied to the bottom surface while the top surface was unconstrained in order to simulate the effect of the substrate interface. An initial domain structure composed of r1/r4 domains was assumed by initially seeding the simulation with only r1 and r4 polarization variants (see Fig. 1.2 for description of polarization variants). The Landau free energy of two BFO films with 109° and 71°, at fixed domain widths, is shown in figure 4.5 as a function of thickness[171]. For lower film thicknesses, and therefore stronger depolarization fields, 109° domain structures are more stable. For film thicknesses greater than 200nm,

71°domains should be more common. In between, there is a region indicating a domain pattern containing a mixture of 109° and 71° domains. This agrees well with experimental observations reported here.

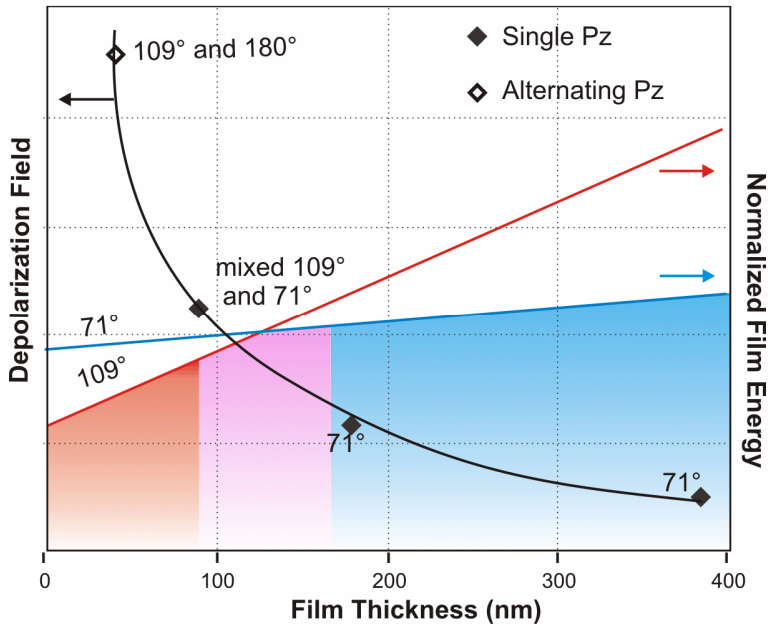

Figure 4.5 Results from phase-field simulations. The domain structure was observed at various depolarization fields. The depolarization field vs film thickness is shown by the black line. The domain structure observed at each measurement point is indicated. Two example landau energy curves of BFO thin films with 109° (red) and 71° (blue) domain structures with a fixed domain width illustrate the crossover between 71° and109° twin structures. These results are in good accord with experimental results

The depolarization field is sensitive to compensation of charge at the interfaces of a thin film. Mechanisms that alter the depolarization field strength include adsorbed ions on the free surface, pinned or mobile charges within the film, and the interface between the film and substrate. Since all of these may depend on the details of thin film growth, the depolarization field strength and thus the transition thickness is likely to be sensitive to the processing method and conditions. The only similar study reporting a direct effect

on domain structures in BFO thin films of similar thickness is in the PhD dissertation of C.T. Nelson[71], in which it is shown that for films produced by a completely different route, RF sputtering, a there is a distinct difference in domain structure for thicknesses between 90 nm and 200 nm was noted. This agrees well with the current result using films grown by MBE, and indicates that the thickness transition, while it may be affected by film growth parameters, it is a material phenomenon as it persists despite the use of different methods of film growth. There are two other references in the literature dealing with RF sputtered BFO films by Folkman et al., in which in one instance an ~180 nm thick BFO film shows 109°[172] domains and an ~160 nm thick BFO film shows 71°s[173] in cross sectional TEM. This apparent contradiction may actually fit well with the story presented here, as both of these thicknesses are near to the 'mixed-phase' region as shown in the phase field simulations. As only a single TEM image at a single thickness is presented, it is impossible to say if this just happens to be a sample from a mixed-domain specimen where one domain type happened to be sampled. T

While the effect of film thickness on static domain structures is significant, switching the polarization of the film is necessary for most potential applications of BFO. Switching effects can be explored in PFM with the addition of an epitaxial LSMO bottom electrode. As there is a considerable difference in spontaneous domain structures, it is possible a change in switching behavior may also be present. The addition of an electrode will have the effect of partially compensating the charge on the bottom interface of the film, so in the ideal case, if the domain structures as seen are dependant only on the depolarization field, then there may be little difference in the switching

behavior. However, if the electrodes do not fully compensate the charge at the interface, an effect based on the film thickness might be expected.

The addition of a bottom electrode adds a large number of complications when trying to disentangle the effect of film thickness for the effects of electrode thickness, the change in the built-in field due to the substrate interface, and changes in the as-grown domain structure driven by the presence of the electrode.

There has been some previous work discussing the effect of electrodes on domain structures in BFO. In previous work on switching dynamics by Nelson et al[91], BFO grown on 20 nm LSMO electrodes on TSO substrates were essentially monodomain, with no preexisting pattern of domains, suggesting that the depolarization field is fully compensated. In the BFO/10 nm LSMO/TSO films used here, a preexisting domain structure does exist, as can be seen in Figs. 4.6 and 4.7. This suggests that the depolarization field is not fully compensated, and a difference in switching behavior is anticipated.

Another electrode effect is based on the thickness of the electrode. In a study examining BFO thin films grown on DSO substrates, it was shown that the thickness of SRO electrode layers directly affects the domain pattern, though the question of how domain switching occurs was not addressed.[174] In their work, for electrodes more than 20 nm in thickness 109° domains were stable. For 10 nm SRO electrodes, a mixed domain structure was stable.

The mixed structure described by Chu *et al.* is similar to the structure seen here in BFO films grown on 10 nm LSMO electrodes. Here as well, there is a native domain structure composed of both 109° and 71° domain regions if films of both 100 nm and 200 nm in

thickness. However, as discussed above, the existence of a preexisting domain structure indicates that the internal and depolarization fields are not fully compensated.

PFM images before and after switching were also collected for both the 100nm film and the 200nm film. Fig. 4.6 shows the results for the 100nm film and indicates that both in-plane and out of plane components switch simultaneously, but only in line with the preexisting domain structure in the film. In the 200 nm films, Fig. 4.7, we first switched the film scanning in one direction, switched the out-of-plane component back, then switched again scanning in a different direction. The result is a change to both the out-of-plane and in-plane domain characteristics, similar to that seen in the 100nm films, but with a much greater effect in plane with the formation of new 71° domain walls. Furthermore, there are several studies in literature that show simultaneous in-plane and out-of-plane switching in PFM. Switching of 600 nm BFO/LSMO/TSO films by Zhao *et al.* showed 109° switching with an out-of-plane component, and in-plane switching with a 71° component[37], consistent with the 200 nm film examined here. Similarly, Balke *et al.*, showed than in-plane switching could be controlled depending on the tip scanning direction[175], though the thickness of the film was not mentioned. For thinner films, out of plane switching has been examined extensively, but little appears to be available for in-plane. In light of the results presented in this chapter, this suggests that, when the depolarization field is incompletely compensated, the same effect seen in the BFO films on insulating substrates presented previously can affect in-plane switching, with thicker films switching easily in-plane while thinner films do not.

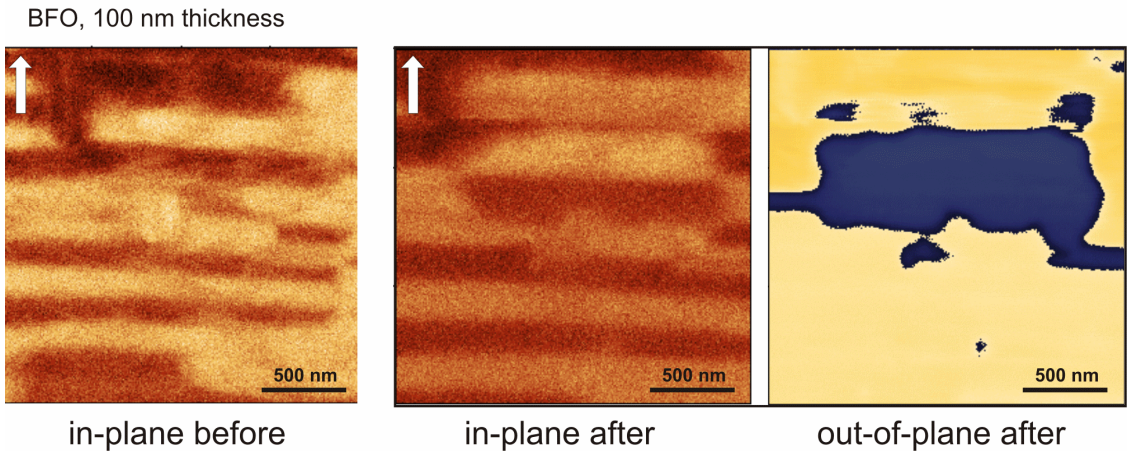

Figure 4.6 PFM switching of 100 nm films. In-plane PFM images of the 100 nm film show a distinctive 71° in-plane striped domain structure prior to switching. Switching with the tip scanned along the direction of the white arrow produces a change in the in-plane and the out-of-plane components.

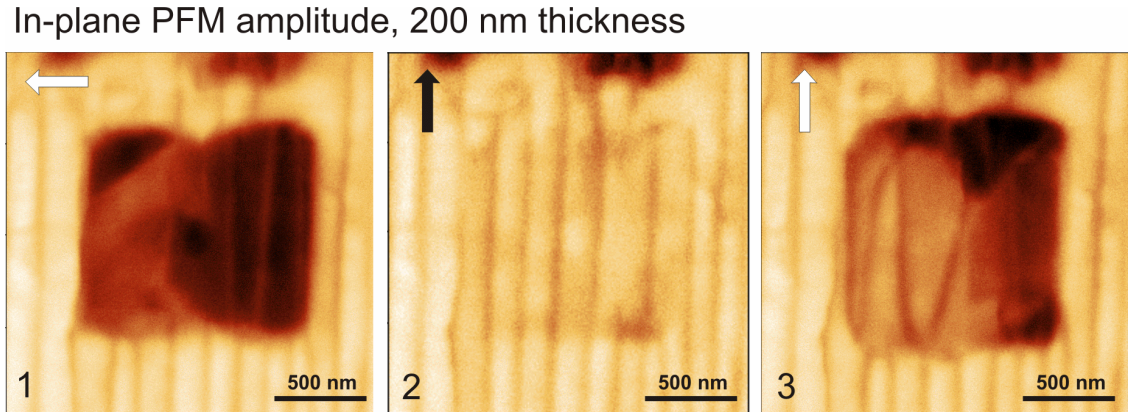

Figure 4.7 PFM switching of 200nm films. Arrows indicate the direction of the scan during poling.

Further evidence that the depolarization field is stronger in thinner films and affects the switching behavior is provided by PFM switching curves. Curves for 100 nm and 200 nm thick BFO films are given in Fig. 4.6. The largest discrepancy is in the 200 nm displacement curve, which shows a double peak. This could be gives evidence of two separate switching events, possibly indicating the occurrence of both out-of-plane switching, and in-plane switching, and this effect is much stronger in the 200nm films

than in the 100nm films. There are two additional interesting features. While both 100 nm and 200 nm films show a coercive voltage offset between the switched and unswitched areas, the voltage offset disappears in the 100 nm films, consistent with a built-in field effect, but is still present in the 200 nm films, and offset to the opposite voltage, which is evidence of a more complicated switching path.

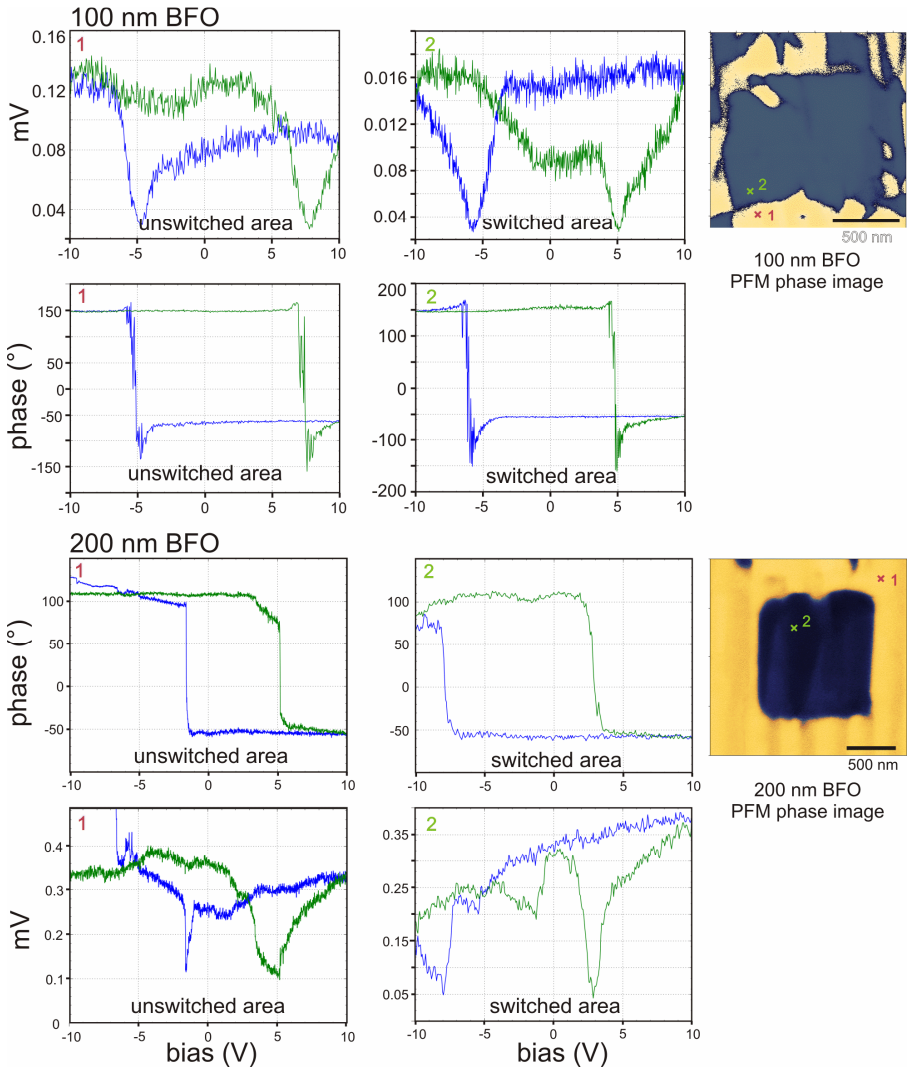

Figure 4.8 PFM switching curves for 100 nm BFO/10 nm LSMO on TSO and 200 nm BFO/10 nm LSMO on TSO samples. The locations where the curves were taken are marked on the images.

4.4 Summary

TEM and PFM imaging was carried out on BFO films of different thicknesses, and indicates that the static domain structure is controlled by the film thickness, with a 109° structure below 100 nm, a transitional mixed structure of ~50% 71°/109° by area at 130nm, and a purely 71° structure above 200nm. This matches well with predictions made by phase field modeling. Therefore, the domain type can be selected simply by changing film thickness. The origin of this change is most likely the depolarization field associated with the various domain types, which shrinks with increasing film thickness[165]. Additionally, with the addition of a back electrode, a change in the switching behavior persists with 200 nm thick films showing easy switching in the in-plane direction and evidence of a more complex multistep switching process while the 100nm films do not. For multiferroic devices, in-plane vs. out-of-plane switching is important due to how the magnetic switching couples to a switchable magnetic layer[166]. As has been stated previously, domain wall type and domain orientation also effects photoelectric properties in BFO[45], opening opportunities to engineer electro-optic devices.

Chapter 5

The influence of epitaxial strain on ferroelectric domains in BFO thin films

5.1 Background

One means of controlling the properties of thin films is by utilizing epitaxial strain with the substrates on which they are grown. In semiconductors, the application of epitaxial strain has been used commercially to tune the electronic properties of the materials. It is expected that similar phenomena would be applicable to oxide thin film materials[1, 44]. In addition to electronic effects, for ferroelectric materials, strain is coupled to the ferroelectric properties via piezoelectricity and large strains provided by epitaxy would be expected to change electrical boundary conditions and therefore change internal fields, and domain structures as discussed in chapter 1. Therefore, misfit strains could be a powerful tool for domain engineering in ferroelectric $BiFeO_3$.

Recently, there has been considerable development in the production of single-crystal rare-earth perovskites, particularly orthoscandates and similar, suitable as oxide substrates for the growth of perovskite thin films[176, 177]. Because of the similar chemistries of the rare-earth compounds, it has become possible to cover a considerable range of mismatch strains by utilizing the different sizes of the rare-earth ions which readily form pseudocubic perovskite-type compounds. In this way, many novel substrates for strain engineering of ferroelectric thin films have become available.

As has been pointed out in previous chapters, different domain types have very different properties, and domain engineering is a promising route to novel electronic devices. Controlling the prevalence of 109°, 71°, and 180° domain walls allows their differing functionalities to be exploited. In addition, for very high compressive misfit strains in BFO grown on LSAT or YAO substrates, BFO has been shown to transform from a rhombohedral to a pseudo-tetragonal structure, with a large increase in the magnitude of the spontaneous polarization[178, 179]. The increase in polarization to values similar to PZT associated with the phase change makes this phase important for lead-free piezoelectrics, as well as substantially affecting the electronic properties[179], opening yet another route for device engineering.

In this chapter, the effects of the mismatch strain to the domain structure and ferroelectric properties are examined through TEM, SPM, and Raman techniques. The strain, film thickness, and resulting domain structures were analyzed to determine effects on the domain ordering and from this extract trends to changes in the ferroelectric properties. Thin films were grown on a series of different substrates with epitaxial mismatches from -6.2% on $YtAlO_3$ to 1.4% on $PrScO_3$. Here negative numbers refer to compressive strains while positive refer to tensile strains.

5.2 Experimental Methods

$BiFeO_3$ films were grown on a set of single crystal perovskite substrates in order to generate differing mismatch strains. Films were grown by reactive-molecular beam epitaxy (MBE) as described in chapter 1. For TEM sample preparation, cross-sectional samples were mechanically polished using diamond lapping film (South Bay Technologies Inc.) and then ion milled in a Gatan precision ion polishing system.

PFM analysis was carried out with an NT-MDT Spectra SPM, and a Bruker Dimension Icon using platinum-coated silicon cantilevers, or NT-MDT conductive diamond cantilevers. The PFM images were captured near resonance both with the tip axis oriented along the film normal and along the film axis for comparison, except where specifically noted. TEM analysis was primarily carried out on a JEOL 3011 TEM at 300kV. Dark field images were tilted slightly off the zone axis and aligned in the two-beam condition (the diffracted beam is along the optic axis). Atomic resolution STEM images were captured using a spherical aberration (Cs) corrected FEI Titan 80-300 operated at 300 kV providing a point-to-point resolution of 0.05 nm (at LBNL). CS corrected Z-contrast images were acquired using a HAADF detector.

Raman spectroscopy was conducted using a combined scanning micro-Raman and scanning probe microscope (SPM) using a 532 nm diode-pumped solid-state laser with confocal diffraction-limited optics (NT-MDT Inc.). Both the excitation and collection of the signal were normal to the sample though the same objective lens. The polarization of the input light was controlled using a half-wave plate, and the depolarized light was collected using a linear polarizer at 90° to the input polarization.

5.3 Results and Discussion

For this work we examined BFO films on substrates spanning a wide range of epitaxial mismatches. Top-down PFM and cross-sectional TEM images were collected from each film. For sufficiently compressively strained films, over 4.4%[178], it is known that the normally rhombohedral BFO can even be converted into a metastable tetragonal phase which was confirmed here on YAO substrates at -6% mismatch. For lower strains, the BFO remains rhombohedral, but there is a strong effect on the domain width and

distributions of widths of domains in these films, indicating that a portion of the strain is relaxed through the formation of domain walls.

Fig. 5.1 shows image data for a range of films with the exception of those under the most compressive strain. The scale for all of these images is the same, and a few trends are immediately evident. Firstly, the films were all grown under identical conditions, but the film thicknesses vary, decreasing with increasing mismatch. Secondly, the domain structures appear similar in the majority of the films, being composed of regular 109° striped domains. Finally, It is clear that there are considerable differences between the domain structures as a function of strain. The domain widths change with mismatch strain. The domain width is a parameter that depends directly on ferroelectricity, and provides a mechanism to compare the different films to one another by comparing the domain width. The results are summarized in Table 1.

Table 1.Summary of measurements for BFO grown on different substrates.

Abbr.	YAO	NGO	STO	DSO	TSO	GSO	SSO	NSO	PSO
	$YAlO_3$	$NdGaO_3$	$SrTiO_3$	$DyScO_3$	$TbScO_3$	$GaScO_3$	$SmScO_3$	$NdScO_3$	$PdScO_3$
Film thickness (nm)	10	24	33	63	54	29	26	16	15
Lattice mismatch (BFO)	-6.2%	-2.6%	-1.52	-0.48%	-0.13%	0.13%	0.66%	1.24%	1.41%
Avg. Domain width (nm)	Mono-domain	80	75	40	41	21	38*	25	15
Avg. domain deviation (nm)	Mono-domain	30	13	20	21	18	25*	10	3
Coeff. Of variance	Mono-domain	0.36	0.30	0.61	0.72	0.76	0.63	0.58	0.31

*SSO is a special case due to an unusual domain structure

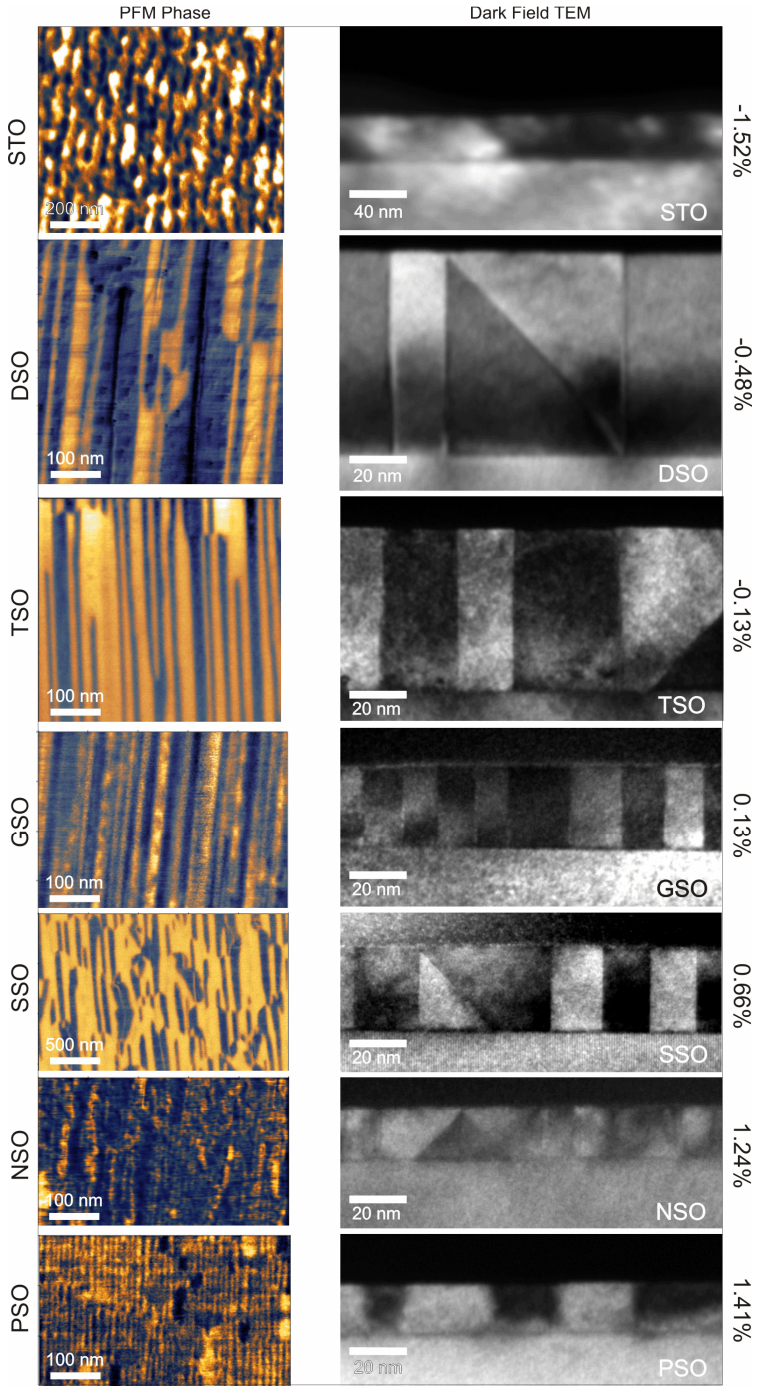

Figure 5.1 PFM and TEM of BFO on various substrates, with the exception of $YAlO_3$ and $NdGaO_3$ as these show no obvious domains in PFM or TEM DF images. The scale is marked for all of the images and a clear difference in domains can be seen over the range of misfit strains From top to bottom: BFO on $SrTiO_3$ substrates show weak contrast in both TEM and PFM, possibly due to weak ferroelectric response, BFO on $DyScO_3$ shows very wide domains, BFO on $TbScO_3$ has the lowest mismatch strain and is used for most of the specimens in this thesis, BFO on $GdScO_3$ has slight tensile misfit, BFO on $SmScO_3$ shows very wide domains in PFM, but much narrower in TEM and is analyzed in more detail later, BFO on $NdScO_3$ shows a very complex domain structure in TEM and very weak contrast in PFM, BFO on $PrScO_3$ at high tensile strain are very thin but show clear, very narrow domains in both TEM and PFM.

A few of the films are not pictured in the figure. The highly compressively strained samples on YAO substrates were very thin, and were evidently in the tetragonal phase. NGO samples cut along the same direction as the rest of the films gave no domain contrast, and PFM gave peculiar results which will be examined in more detail later.

In regards to film thickness presented previously, for the range presented here relatively regular 109° striped domain structures would be expected for the majority of these films at low strains. For films less than 20nm in thickness, it is possible there is some convolution with film thickness effects, but as these are only for the most highly strained samples and mismatch is explicitly taken into account in the models describing the behavior of ultra-thin films, the strain effect is expected to be dominant.

As domain width also depends on the film thickness by Kittel's law[180], in order to compare domain widths between samples grown on different substrates, it is first necessary to ensure that the variation in width does not simply follow the film thickness. Figure 5.2 compares 109° domains from several film thicknesses and allows the expected domain width to be calculated. It should be noted that for the thickest films in this series, the 109° domains were stabilized by defects, as explained in Chapter 3. Despite this, they clearly fit the trend. With this information, it is possible to calculate the expected domain width for films of any thickness, without strain, and use these results to isolate the changes that occur with misfit strain.

To generate Fig. 5.3, domain widths were measured from many PFM and TEM images, and the mean value of domain width and the coefficient of variance for all of the domain widths were calculated for BFO films grown on each substrate. The coefficient of variance is the standard deviation divided by the mean value, and provides a better metric

for comparing data sets where the means are considerable different from each other than the standard deviation. The Kittel thickness relationship was used to ensure any trend was not a result of the difference in thin film thickness shown in Fig. 5.1.

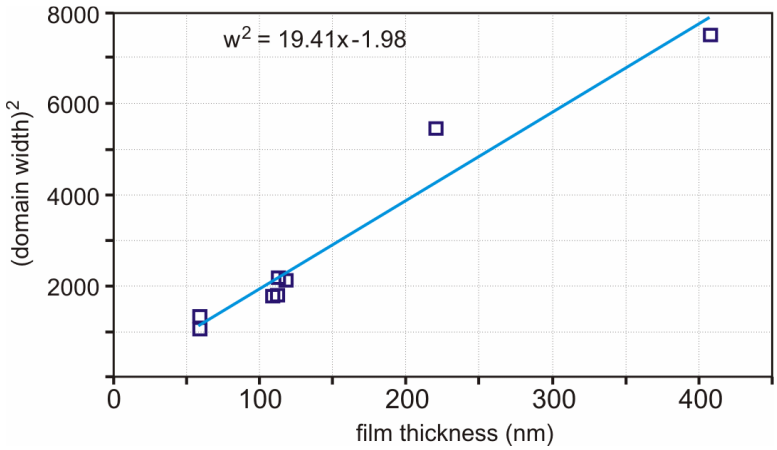

Figure 5.2 Fit line and equation for Kittel's law calculation of the domain width vs thickness. This allows the Kittel scaling law effects to be separated from the strain effects in the next figure, as the expected domain width for a given thickness can be calculated from the trend line.

From Fig. 5.3, it is possible to extract some trends. If BFO grown on NGO and SSO are excluded, there is a clear trend of decreasing domain width from compressive misfit strain, through zero, and continuing as misfit strain becomes tensile. This trend persists even when the Kittel thickness effect is taken into account. Functionally, this means that the density of domain walls increases as the misfit strain becomes tensile; a property that could be of use to tune the materials properties by controlling domain wall density. There are two points to be made from this. For compressive strains, domain walls are suppressed, and for tensile the number of domain walls increases, compensating some of the strain energy. Interestingly, this trend is similar to those described in the work of Daumont *et al.*,[181] where the piezoelectric coefficient declines considerably and polarization declines slightly as misfit strain goes to the tensile side.

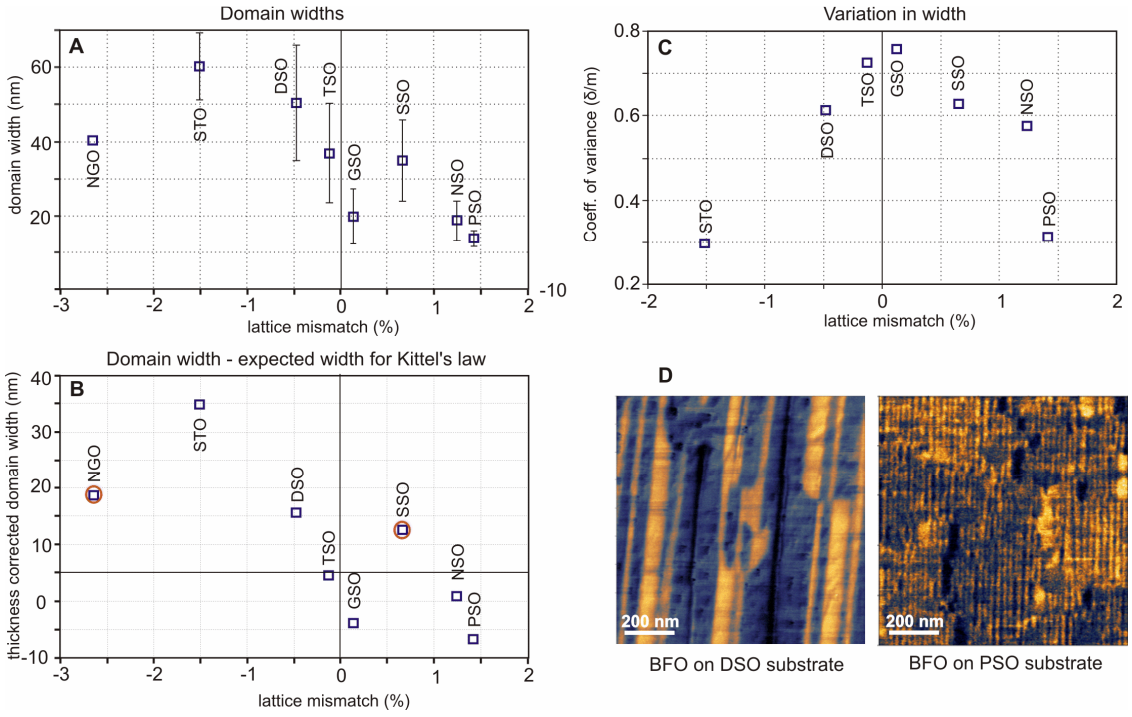

Figure 5.3 Statistics for domain widths in BFO under strain due to epitaxy with different substrates. (A) The mean domain width for films grown on each substrate, with error bars. (B) The mean domain width with the expected domain width from the Kittel rule subtracted showing the differences are due to strain, not thickness. Apart from films on NGO and SSO substrates, marked in red, there is a clear trend of decreasing domain width for increasing tensile misfit strains. (C) shows the coefficient of variance (mean/standard deviation) for each film with a maximum deviation from the mean at the lowest misfit strain. (D) PFM images from a compressively strained and tensile strain specimens illustrating the difference in domain widths.

The second trend is in the distribution of domain width as a function of strain. The variance of domain size is at a maximum at low misfits, and decreases as misfit strain increases, for both tensile and compressive misfits. More strained films, then, have more uniform and regular domain structures than unstrained films. This implies that there should be fewer different domain types for more highly strained films, as they have different widths; a topic that has been demonstrated in earlier chapters.

Finally, there are two standout anomalies from the trend in width, marked in Fig. 5.3B. On the compressive side, BFO/NGO has a much lower width than expected, and on the

tensile side BFO/SSO has much wider domains. These two have unusual domain structures and require closer examination.

For BFO/SSO, there is a large mismatch between the PFM data and the TEM data. The PFM data shows large domains with a very strong out of plane difference in response, while the TEM shows much narrower 109° domains, pictured in Fig. 5.4. Close examination shows that the domain structure is a composite 180°/109° structure. High resolution imaging demonstrates that there are few defects in the film, and the domain walls are very clear. The very high concentration of 180° walls is unusual for BFO and may be of interest due to high conductivities and strong magnetization, giving rise to exchange bias that could be useful for magnetoelectric devices[182], To date, a bimodal distribution of this type has not previously been described.

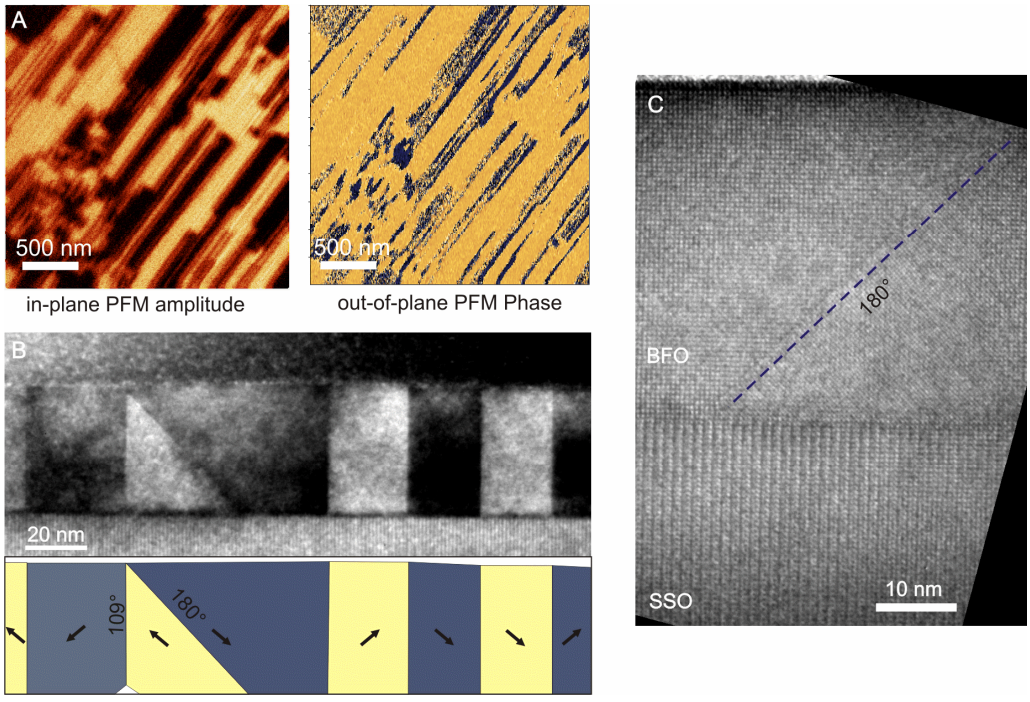

Figure 5.4 Tensile strained BFO on SSO, which shows a very strong mix of fine 109° domains in 180° domains with a large piezoresponse. (A) PFM out of plane amplitude and phase images showing broad stripes ~100 nm in width (B) DF TEM showing nanodomains ~30 nm wide and a schematic of the polarization (C) HRTEM phase contrast timage showing a 180° domain wall. The 180° domain walls show no particular difference from those that occur with much less frequency in other films. Their concentration in the sample, however, is very high.

On the opposite side of the strain curve, in the compressive regime, BFO on NGO shows two very interesting properties. Images and analysis for this film is shown in Fig. 5.5. The first property of interest is the overall domain structure, which is composed primarily of 71° domains, a structure not seen in most other films at this thickness. In literature, there is some suggestion that 71° domains should be stable at small compressive strains, of ~0.06%[183]. However, in this work, BFO/NGO is the first specimen showing a 71° in plane domain structure, at a misfit of -2.6%. It should be noted, however, that while TEM shows few defects or misfit dislocations that could release the strain, the actual strain was not measured and could be somewhat lower than the calculated misfit value.

In addition to the in-plane domain pattern, there are also scattered domains with a very strong out-of-plane component. The strong upward domains should not be 109°, as that would result in highly charged domain walls. They appear circular and are scattered randomly about the film. Atomic scale mapping shows that the majority of the film remains tetragonal, and we did not capture one of these regions in TEM. Since BFO/NGO has a relatively high compressive strain, it is possible that these domains correspond to the tetragonal phase in BFO, which has received a lot of interest for its very high remnant polarization and other properties.

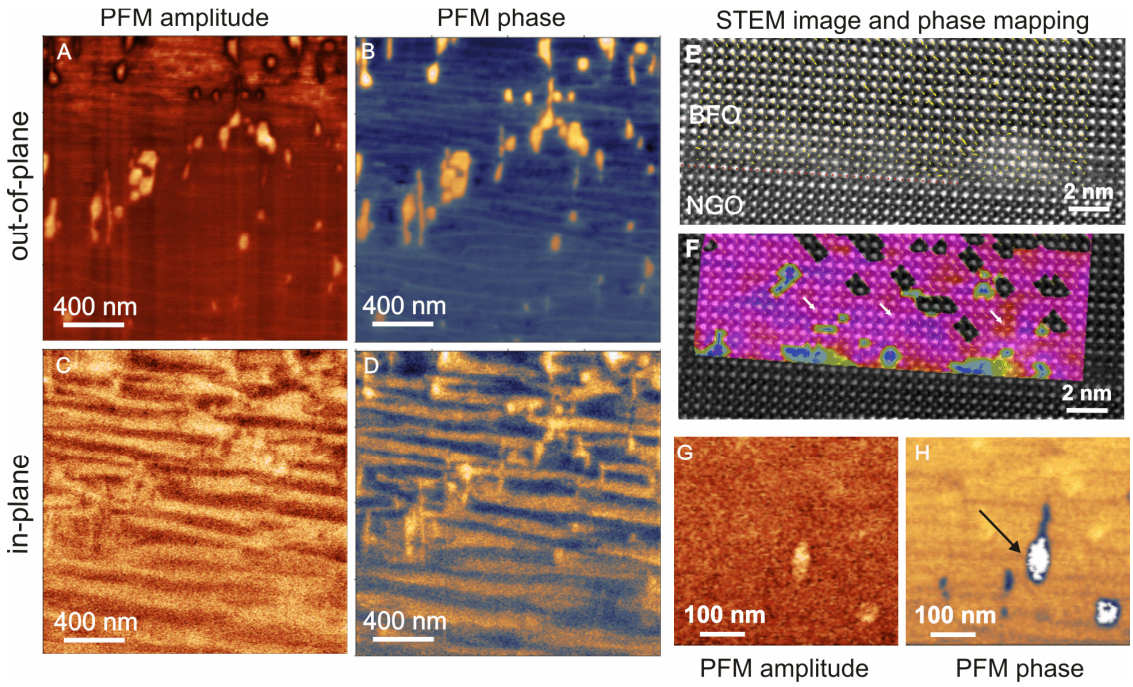

Figure 5.5 Compressively strained BFO /NGO, where a mix of 71° and possibly tetragonal out-of-plane nanodomains exist. The existence of the 71° structure at this film thickness is unusual, and suggests a strong electrical effect occurs at the interface. (A) and (B) show out of plane amplitude and phase images, respectively. (C) and (D) are the corresponding in plane images showing strong 71° domain contrast. (E) and (F) Polarization mapping indicates the majority of the film is still rhombohedral. The white arrows show the direction of the polarization. (G) and (H) show out of plane amplitude and phase of the bright nanodomains. From the amplitude contrast, the amplitude of displacement is high and the direction, via the phase image, is completely out of plane suggesting these nanodomains might be pockets of tetragonal-phase BFO.

5.4 Summary

High quality BFO thin films were grown on a variety of perovskite substrates to examine the effect of misfit strain on ferroelectric properties. The domain structure was examined with PFM and cross-sectional TEM techniques. In order to better compare domain structures in these specimens, average domain width was chosen as a metric and measured for all of the relevant samples. We discovered several trends and identified some film/substrate configurations with unusual domain structures that make interesting candidates for further property testing. In general trends, above -1.52% strain, all of the films showed striped 109° domain structures in TEM. The average domain width,

starting with compressive misfit of -1.52%, decreased steadily through the highest tensile strain. Therefore greater tensile strains resulted in a higher density of domain walls and we can conclude that some of the strain energy is relieved by forming additional domain walls as we move towards higher tensile strains. Additionally, the coefficient of variance of the domain width (standard deviation/mean domain width) is at a maximum for the lowest strains and decreases for both compressive and tensile misfit strains. This indicates that strained films have more uniform domain size than less strained films, even though there is a higher density of domain walls.

There are a couple of outliers to these trends. The film grown on an $SmScO_3$substrate was an exception to this rule and instead showed a completely different domain structure with a 109° pattern embedded in a much larger 180° degree domain structure, while samples grown on NGO show an in-plane 71° domain pattern coupled with small areas of very strong out-of-plane polarization that may correspond to pockets of T-BFO. From these results, we can conclude that strained films form more ordered domain structures which may be of use in domain engineering. More interestingly, there are two outliers. Compressively strained NGO may contain localized T-phase BFO, allowing R-T switching with the inclusion of a back electrode. Meanwhile, samples grown on tensile-misfit SSO substrates show a very large concentration of 180° domains and are a good candidate for exploiting the properties of 180° switching in BFO.

Chapter 6

TEM in-situ holders combining STM, optical excitation, and spectroscopy

6.1 Background

Here we demonstrate a custom-built *in-situ* stage allowing a combination of electrical probing and optical excitation and spectroscopy in a double-tilt system that accommodates conventionally polished specimens. The design parameters and performance of the system is demonstrated. The combination of probe and optical input will enable such experiments as direct measurement of the effect of defects in PV structures on photovoltage, in conventional materials such as GaAs, and in ferroelectrics like $BiFeO_3$, which has shown promise as a high voltage PV material[45]. It may also find application *in-situ* examination of photocatalysis, and other light-matter interactions.

Since the invention of electron microscopy, there has been interest in not only observing static structures, but also observing physics in action. In the transmission electron microscope, phenomenon on the scale of angstroms can be examined and over many years, many different experimental apparatus have been designed to allow external stimulus such as temperature, electrical bias, and mechanical force to be applied. These allow the response of materials to such stimuli to be observed, often in real time. Despite a great deal of effort including work with heating, cooling mechanical deformation,

environmental stages such as gas and liquid atmospheres, and magnetic contrast via Lorenz microscopy undertaken since the 1970's[79], much remains to be done.

The majority of *in-situ* specimen holders are built to a singular purpose, though more recently, there is a considerable push to incorporate as many different measurements as possible into a single holder, as has been noted in at least one review[184]. There are stages allowing mechanical testing, particularly indentation[185-190], electrical bias[152, 191-193], application of magnetic fields, gaseous atmosphere and heating[194, 195], liquid cells[196, 197], *in-situ* battery testing[197-200], and correlated TEM and optical microscopies [201, 202]. It should also be noted that most available *in-situ* holders are single-tilt, with a few exceptions[203]. This limits their application generally to nanostructured materials and makes observations on thin films and polycrystals much more difficult.

It is possible to divide the current holder technologies into a few categories. The first and most common of these are the dedicated-use holders, which includes many commercial products for heating, cooling, and with electrical feed-throughs. These have been available for many years. In particular, the electrical feed-throughs have limitations on their application in that they require specially constructed specimens for measurement. Another option for biasing is the use of a probe-type holder. There are a few examples, including commercial options from Hysitron[188] and the now defunct Nanofactory AB, which has been used in several studies[157, 198-200, 204], that use the concept of a moveable STM-type probe that allows bias to be applied to specific features in regularly prepared samples. Such holders, theoretically at least, are also capable of performing scanning probe imaging *in-situ*. However, in practice they have limitations on their

electronic performance, and they do not include optical or other feedthroughs for more complex experiments. Finally, a popular modern approach is to use chip-based MEMS devices. In this case, a semiconductor fabrication methods are employed to create an "experiment on a chip", which can then be loaded on TEM specimen rods. Many different MEMS designs have been employed in literature [8, 12, 195, 205-207], and several commercial products are available that take this approach, from ProtoChips, Hummingbird Scientific, and others. This approach has both advantages and limitations. The biggest advantage is that the potential experiments are limited only by the available feedthroughs in the specimen rod to support the device under test. However, such systems are limited by the availability and cost of producing the chips, which are consumed with each experiment. Additionally, it is very difficult to mount thin film or monolithic specimens using this approach and requires advanced specimen preparation techniques. Finally, while the MEMS approach greatly simplifies the construction of a specimen holder, it is not as flexible or able to combine as many experimental functionalities such as bias, light, and a moveable probe. Instead, for each application, specialized chips must be developed. In a probe holder, all of these elements can be combined and used on conventionally prepared samples. For these reasons, our current design uses a probe approach rather than a MEMS approach.

The primary engineering problem, noted by many authors[79, 187], is the very small space available in the pole piece gap of the microscope. The entire experiment must sit within at most, a few millimeters in the gap between the pole-pieces in the TEM, and the entire specimen rod is only 10mm or less in diameter. This highly constrains design as space must also be made for electrical wiring, tilt stage pushrods, and other components.

In addition to the small space, problems with charging from the electron beam must be taken into account to minimize electrical signal noise[204].

Under electron beam illumination, several different signals are emitted which could be captured in an *in-situ* experiment. A schematic of the signals emitted is included in Fig. 6.1A. Electron beam induced current (EBIC) carries information about conductivity local to where the beam is focused, while the cathodoluminescence (CL) signal contains information about doping, interfaces, plasmon emissions, and chemistry. In addition to capturing the light and electrical current generated by the electron beam, the second part is to applying additional stimulus such as a bias voltage to examine electronic properties, or an optical signal to excite photovoltage or Raman scattering. All of this information will be correlated to the TEM image.

In this work, we describe a probe-type biasing double-tilt TEM holder that combines a mechanical three axis approach, piezo scanning ability, and optical excitation in a single specimen rod. A schematic of the approach is shown Fig. 6.1B. To our knowledge, this is a uniquely multifunctional system, combining double-tilt capabilities with an SPM scanning probe, biasing, and optical input/output. We demonstrate the high current resolution and spatial resolution *in-situ*. We further demonstrate the optical capabilities through direct measurement of the photovoltaic properties of nanoscale structures including ferroelectric domains in thin film cross-sections.

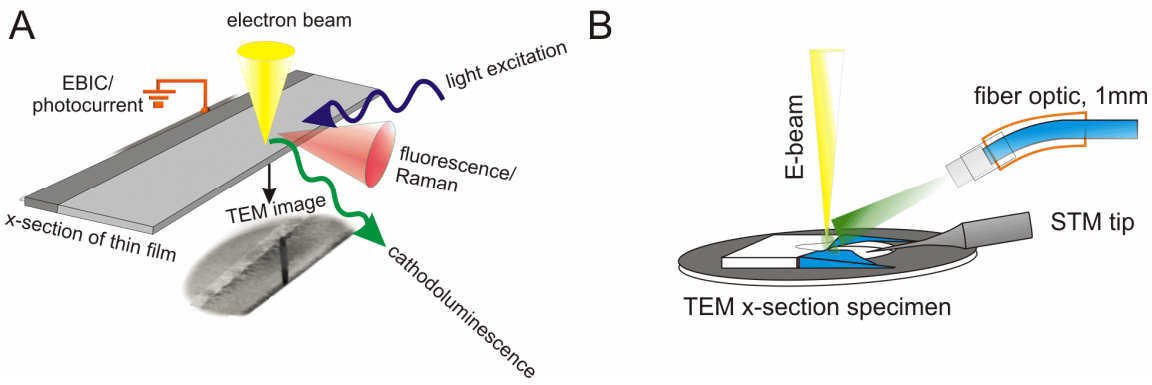

Figure 6.1. Signals produced in TEM and design scheme. (A), the measureable signals produced by the electron beam,(B), the probe and signals applied to the specimen. The electron beam projects an image while the probe tip is able to select features of a few nanometers in dimensions to apply bias. The fiber optic cable allows intense light to be project on the sample and the photovoltage to be measured with high spatial resolution by the probe.

One potential application for the unique combination of a scanning bias probe and optical input is in photovoltaic materials. This setup gives a unique opportunity to examine nanoscale details of the interaction of defects on photovoltage. In particular, the precise effects of crystalline defects can be measured directly, which will be of considerable value in solar cell structures[208]. Additionally, there is much interest in the intermediate band solar cell structures which incorporate nanoscale components such as quantum dots[209]. Finally, another interesting application lies in ferroelectric materials which produces high cell voltages, but low efficiencies[210]. There are also additional open questions in ferroelectric materials concerning the effects of domain polarization and domain walls on PV properties in $BiFeO_3$[211]. Direct *in-situ* TEM investigation of these properties has not previously been available.

6.2 Results and Discussion

In a preliminary attempt to extend the functionality of an existing holder to add optical excitation, two LED's were added to an existing probe holder made by Nanofactory AB

(NF). This modification is pictured in Fig. 2. This provided ~24 mcd of blue light for preliminary experiments. The results of which were encouraging, but there were several important limitations. First, the current resolution was at best ~1nA. This is a relatively low sensitivity for electrical experiments for specimens on this scale. Secondly, the low intensity of the illumination and the inability to choose the excitation wavelength limited the potential photocurrent signal. Thirdly, the movement system on the NFholder is very delicate, and can be unpredictable. A more robust solution for coarse movement is desirable.

There are benefits to using an optical fiber over an LED light source. The use of a fiber as a light pipe removes any limitations on the wavelength and intensity of the light source, while the diodes are fixed output. This is important when measuring optical responses of different materials as the light source can be chosen to match the specific absorption of the material. This also removes the limitation on input power, within reason, as very intense sources such as lasers can be used. This naturally increases the response that can be measured. Another consideration is focus of the light onto the sample. The emission of the diodes cannot be focused onto the sample and much of the light intensity is lost in this way. Finally, the LEDs emit a small amount of heat as well as light, which can strongly influence electrical measurements or introduce mechanical instability due to thermal expansion of the rod tip. Using a fiber, the only heating is due to the optical illumination, which cannot be avoided anyway.

Using an optical fiber light pipe, it is also possible to collect and analyze visible light emitted by a sample. However, the optical requirements for light collection are much more stringent than for optical excitation and there is not enough room to accommodate

both a fiber close enough to the sample to collect a reasonable amount of light, and the STM electrical probe. In order to be able to acquire optical signals emitted *in-situ* in TEM such as CL, or with additional light input, Raman, a holder optimized for light input and output was designed.

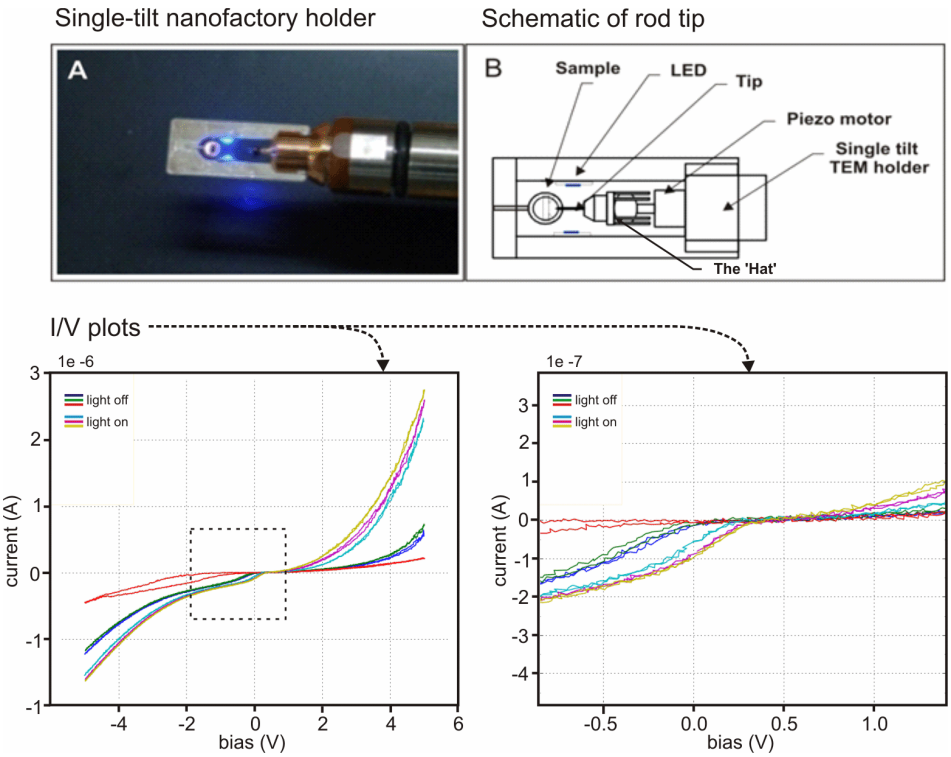

Figure 6.2 Modifications to the NanoFactory holder and preliminary data. The sample was a PIN GaAs solar cell and shows a very weak, but notable, response. (A) shows the tip of the NF single tilt holder with the blue diodes installed. (B) shows a schematic labeling the components of the NF holder. The I/V plots showing the light on/light off curves for a GaAs solar cell show an indication of photovoltage.

The design goal for these holders was to enable electrical probing, optical excitation, and in the second holder, detailed optical measurements to be carried out *in-situ* in the TEM on samples prepared using standard techniques. Additionally, since many of the materials of interest are in the form of cross-sectional single-crystal thin films, the holders must be double-tilt to allow accurate alignment of the zone axis for imaging.

While, in the literature, there are a number of recent attempts to combine TEM and optical measurements, none match the capabilities specified for these designs.

6.2.1 STM/optical holder design

The mechanism for the specimen rod incorporates three separate systems, a mechanical coarse motion approach system, a piezo scanner for fine motion and STM scanning, and an optical input compatible with these systems. The mechanical system will be discussed first. This system utilizes a spring and pushrod approach, allowing three axes of motion. A schematic of the x-y system is shown in Fig. 6.3. Movement along the axis of the holder (z) is handled by moving this entire apparatus, as described in Fig 6.4.

The pushrods pass through a compression vacuum seal just behind the fine-motion piezo scan tube, and through to the rear of the rod where they are actuated by preloaded micrometers. For the z-motion the entire central assembly is spring-loaded and actuated by another micrometer at the back of the holder. This allows three axes of motion, with a maximum mechanical resolution of ~100 nm for a 1° turn of the 80 thread/inch micrometer. The use of a mechanical system such as this carries some advantages over an inertial-drive system as seen in Bobji *et al.*[185] and in the NanoFactory AB systems. The strong mechanical connection eliminates the 'jitter' applied to the tip from the pulse motion of the piezo. It also avoids limitation on the amount of force which can be applied by inertial-drive piezo motors which cannot apply large forces as this undermines the inertial slide mechanism. With respect to the Nanofactory holders, it avoids the variability of the coupling between the mechanical motions caused by the freedom of the 'hat' (see Fig. 6.2B) to slide and rotate in any direction. Finally, the use of a mechanical system allows the motion to be automated with stepper motors, for which control

solutions are inexpensive and easily available. Fig. 6.3 shows the completed rod, and a close up image and schematic of the rod tip showing the layout of the components while Fig. 6.4 shows the construction of the actuators at the back of the holder.

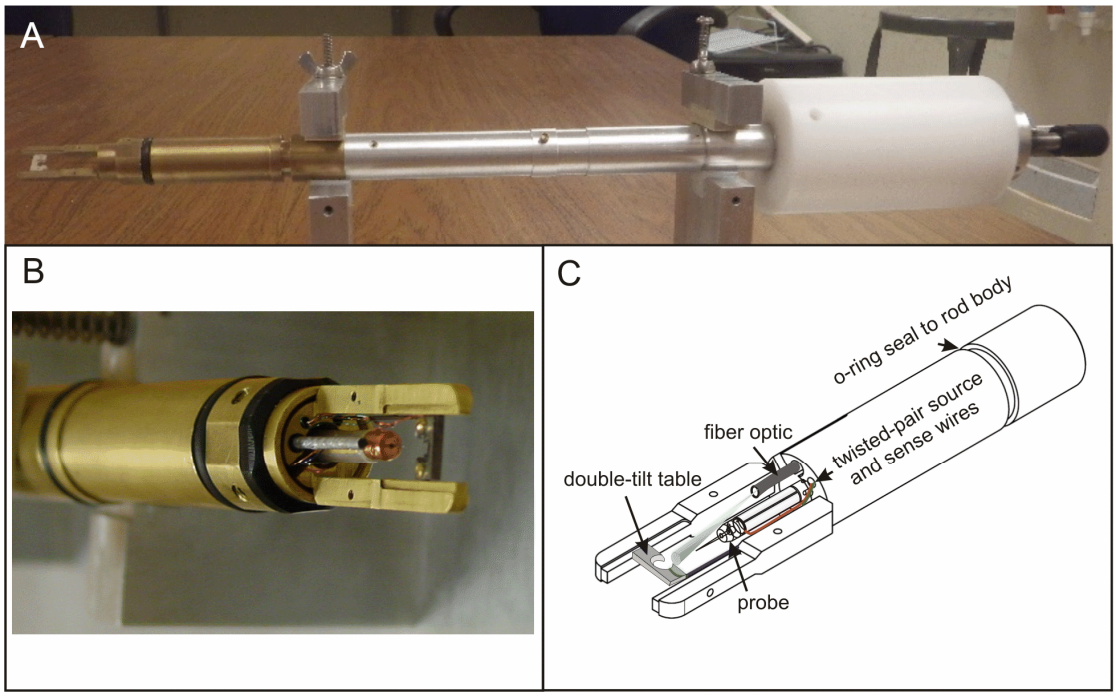

Figure 6.3. Complete rod and assembled fork. (A) shows the complete assembly. The black knob at the back of the holder actuates the z-motion. (B) and (C) show an image and schematic of the tip assembly.All of the moving components are sealed into the tip component, which then seals against the interior of the rod bore. The tip is mounted on the copper cap in panel (B).

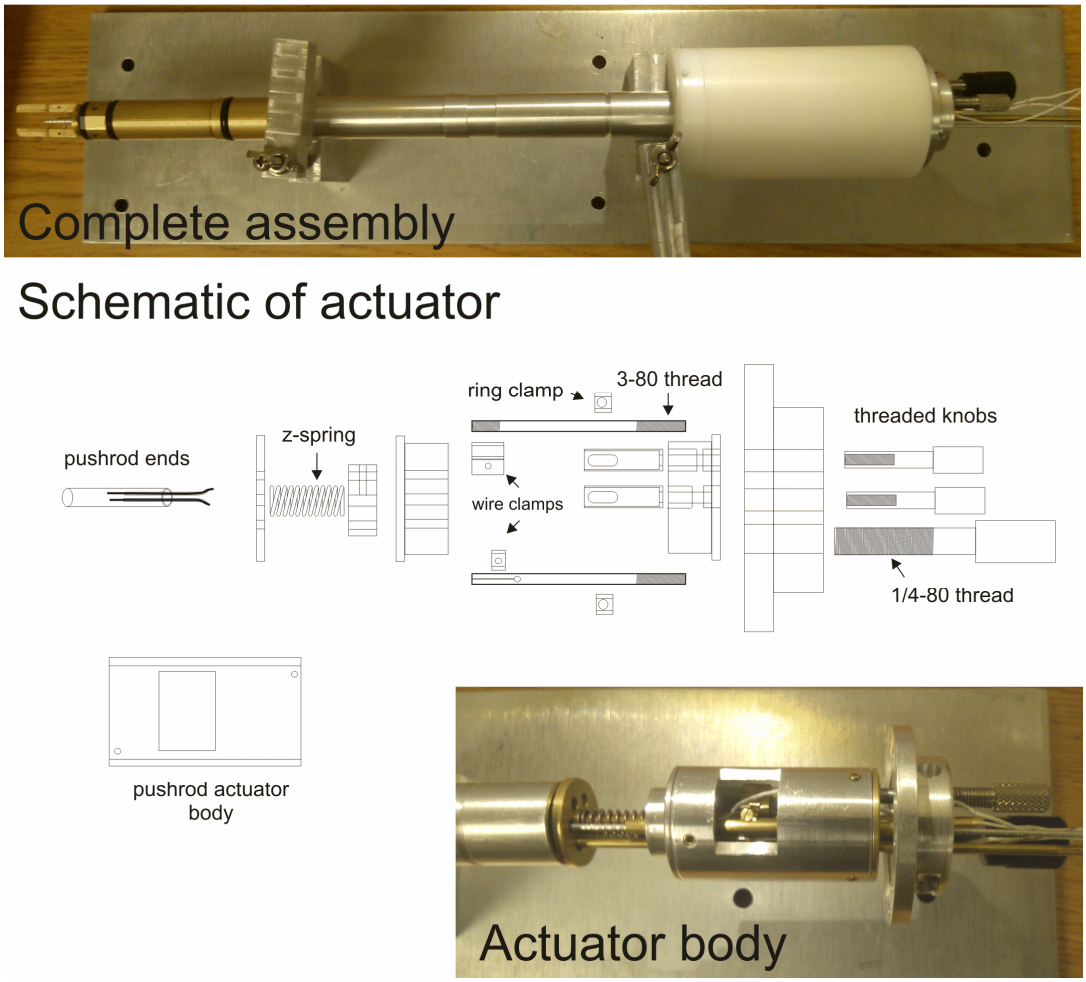

Figure 6.4 Schematic of the actuator component for the mechanical motion. The spring-loaded micrometers are all contained at the rear of the rd, where they are clamped to the wire pushrods at the end of their guides. The entire actuator body moves within the rear cover for motion along the rod axis

As electron beams operated in vacuum, the pushrods for the mechanical drive must pass through an effective sliding vacuum seal. The vacuum seal for the x and y tilting motion is shown in detail in Fig. 6.4. The pushrod wires pass through a viton seal sandwiched between two guide washers that prevent buckling of the pushrod wires and provide pressure to create an effective seal for the very small linear motion of the pushrod wires. The z-motion of the entire assembly is sealed by an internal o-ring groove at the back of the tip portion, as shown in Fig. 6.5. The drive wires for the fine-

positioning piezo pass through the same tube as the pushrod wires and guides. This effectively isolates them from the wiring used for sensing.

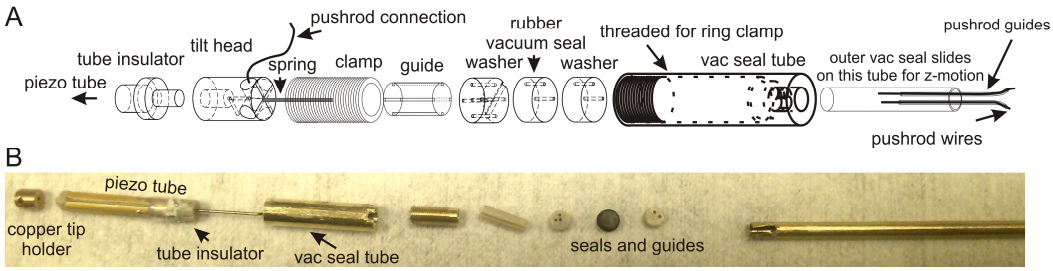

Figure 6.5 Schematic of the x-y mechanical motion system and image of the components. For scale, the piezo tube in the image is 3mm in diameter

The fine motion drive is a PZT piezo tube allowing sub-nanometer spatial resolutions for positioning and STM scanning within the TEM. The scan tube is mounted on an insulating base which connects it to the mechanical coarse motion system. The scan tube has four quartered electrodes and a center electrode, and can be driven by any available SPM scan controller. In this work, the scanner was connected to a Nanosis SPM scan control system from SPECS. This allows both fine positioning and STM scanning to be carried out. The scan tip is mounted in a copper cap, insulated from the piezo scan tube. The tip voltage and stage sense wires are carried by twisted pair shielded wire that is completely separated from the piezo drive electrics in order to prevent crosstalk between the scan and bias voltages.

In order to effectively image single-crystal film specimens, a double-tilt holder is required. The tilt-stage is also actuated by a mechanical mechanism constructed in the same manner as the coarse-motion approach system. It should be noted that the majority

of *in-situ* holders are single-tilt, and therefore unsuitable or difficult to use for high resolution imaging of thin film specimens which constitute the majority of electronic materials samples. The double-tilt system is driven by a rod arrangement mounted to another spring-loaded micrometer at the rear of the specimen rod.

Finally, the optical system is comprised of a hard-mounted fiber optic element which can be coupled to either a visible light source, or to an external spectrometer. The combination of an optical feedthrough, double-tilt capability, and three axis scan and motion control was a considerable engineering challenge, and is unique to this measurement setup.

6.2.2 Spectroscopy holder design

Currently, Gatan supplies a commercial CL measurement holder, and it is single-tilt, and relatively low efficiency, using two single-mode optical fibers to illuminate/collect optical signals. In this holder, space is extremely limited, and electrical connections would be very difficult. The system is also very large, and requires additional support facilities from the electron microscope. A commercial fiber-based optical holder was previously available from the now defunct NanoFactory AB[212]. However, from our experience with NF holders, the probe's coarse motion is somewhat unpredictable, nor did they produce a double tilt holder that would fit in an ultra-high resolution TEM where the polepiece gap is limited to ~2.2 mm. Other methods for optical input and detection either allow only fiber-based illumination, or required extensive modifications to the TEM[213, 214].

The spectroscopy holder design described here utilizes many of the same design elements as the STM holder described above. In particular, the tilt stage and tilt

mechanism are identical. In this holder, there are two included optical fibers, one for excitation and one for spectroscopy. In order to optimize the optical system, a focusing/approach mechanism was implemented. This allows for either a very close approach with a fiber, or focusing of a lens system on the sample, as the greatest amount of light is collected when the emitted area is in focus. Light input is also accomplished similarly to the previous holder, where a bare, polished optical fiber is used. The optics required for light collection, however, demand greater complexity. Images of the holder, specimen stage, and the optical design schematic are shown in Fig. 6.6.

From a physical standpoint, the zone from which light is emitted from the interaction between the electron beam and the specimen is small enough to be considered a point source. The challenge is to collect as many of the emitted photons as possible and couple them into the optical fiber. As the acceptance angle of an optical fiber is very small, 24.8° in this case, in order to increase the amount of emitted light collected, additional optical elements were needed. These consist of a mirror shroud surrounding the fiber, a small objective lens, and a graded-index lens to effectively couple the collected light into the optical fiber. As we are using a lens system, the focal point must sit at the sample. This necessitates a focusing system in order to maximize the amount of signal collected. The objective increases the acceptance angle of the fiber and helps capture the photons collected at the mirror. The diameter of the fiber also affects the total solid angle from which the signal is captured. A very thin fiber collects light from a smaller total area than a wide one for the same total collection angle. However, there is a trade-off. Due to dispersion, the collected light beam becomes less collimated over the fiber length than for

a thinner fiber. This effect is minimized by keeping the length of optical fiber between the holder and the spectrometer used for analysis as short as possible.

A second factor determining the amount of signal collected is losses between the lenses, fiber, patch cable connections, and the spectrometer. The signal losses can be minimized using a few optical elements and cable connections as possible. At each fiber-fiber connection some of the collected light is lost due to reflection at the interface. The best way to avoid this type of loss is not to use a fiber at all. Instead, the ideal situation would be to project the collimated signal through free space. Unfortunately, due to space and the need for vacuum seals, this is not possible and some kind of light guide is required. Since an actual image of the interior of the microscope is not required and the optics to project an image from inside the TEM would be very awkward, the simplest solution is to use a fiber optic element. Finally, a spectrometer is needed to analyze the captured light. In this case, the greatest constraint is the requirement for portability and space, as the unit must be transportable between different TEM facilities. With this in mind, it drastically reduces the options for spectrometers. Fortunately, several makers produce miniaturized spectrometers, though miniaturization comes at the expense of a loss in energy resolution due to the low path length. The second requirement on the spectrometer is a low-noise high sensitivity sensor. There are several sensor types, including photomultiplier tubes (PMTs), avalanche photodiodes, and charge-coupled devices (CCD). Avalanche photodiodes and PMTs are essentially photon counting devices, they can only measure the intensity of all light hitting them at a point in time. This requires the spectrum to be scanned via a monochromator, which is not generally possible in the micro-spectrometers. The situation is similar for PMTs. This leaves only

CCDs. There are two major benefits to CCD detectors. The first is that a CCD array collects from the entire spectrum at once, greatly reducing the spectrum acquisition time. Secondly, back-thinned CCDs can have very high sensitivities and with thermoelectric cooling, sufficient stability for long integration times. For this reason, an Ocean Optics QE Pro spectrometer was chosen for this application.

Our optical holder design allows for several unique capabilities. First, it is a double-tilt (DT) holder that is designed to fit in the 2.2 mm UHR pole-piece gap for JEOL microscopes. Other optical excitation or measurement platforms are not DT, or require larger gaps. This is important to allow simultaneous high-resolution imaging along with optical excitation and measurement. Secondly, typical optical holders rely on direct coupling into the fiber, requiring the fiber to be placed very close to the sample. In this case, the large lens area coupled with the reflector, allow collection from a much larger solid angle while far enough away to allow for DT motion. This allows for collection of several different types of optical signal. One of primary interest is cathodoluminescence, which yields detailed chemical information that may be mapped with the high resolution of STEM. A second mode of operation allows illumination from the second optical fiber, and measurement of fluorescence or photoluminescence (PL , or integrated photocurrent from the sample. With the appropriate edge filters for the spectrometer, *in-situ* Raman is also possible. In this way, electron-beam driven reactions or photoactivated reactions can be monitored *in-situ*. Finally, electrical feed-throughs allow *in-situ* examination of electro-optical devices.

Unique features include:

- Double tilt capability allows for high resolution TEM
- Large, adjustable-focus optical element means the solid angle for detection is not limited by the narrow numerical aperture of the fiber.
- The system is designed to fit in a UHR pole-piece gap, which would otherwise limit the TEMs that could be used.
- Capable of CL, PL, Raman, fluorescence, and optical excitation measurements, with appropriate external optics
- Together, these holders represent a unique design with novel capabilities, as well as a considerable improvement on older systems. There development will vastly expand the possibilities for *in-situ* TEM.

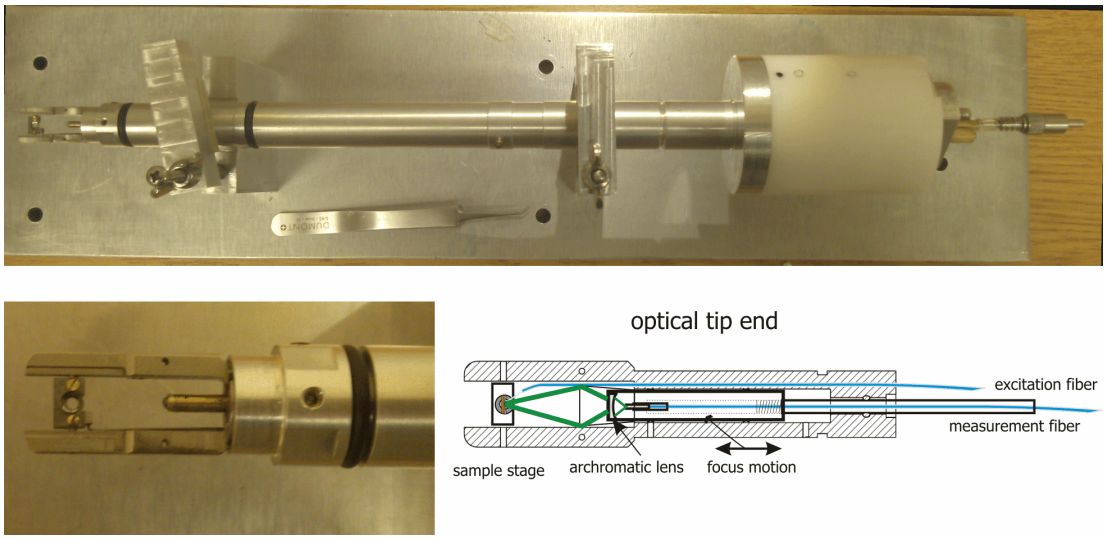

Figure 6.6 Optical holder design schematic. The optical fiber is bare in the image at the bottom left. The rod is threaded to accept different caps that can contain either, the lens and reflector assembly in the schematic, a bare optic fiber for close approach, or a single graded-index lens to improve collimation.

6.2.3 Performance Testing

At this time, the TEM holder platforms described here are in testing, as depicted in Fig. 6.7, which shows the optical holder inserted in the TEM and a test image of a partially oxidized silver film. The mechanical and optical systems have been proven to work, but the bulk of the experimental work remains, as Future Work.

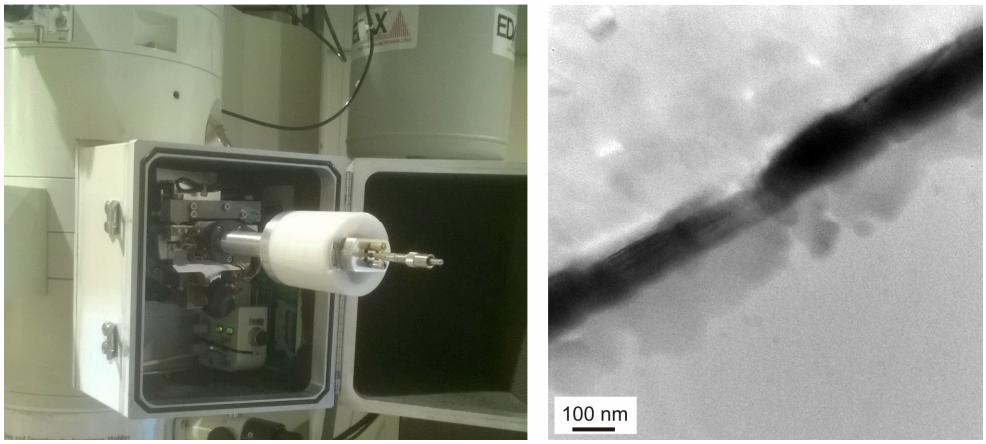

Figure 6.7 TEM specimen holder inserted into the TEM. The second panel is a test image of a partially oxidized silver film.

Conclusions

A novel set of specimen holder rods for *in-situ* transmission electron microscopy were developed.The custom-built *in-situ* stages allow for a combination of electrical probing, optical excitation, and spectroscopy with double-tilt capability that accommodates conventionally polished specimens. The design parameters and performance of the system is demonstrated.

Chapter 7

Polarization-dependent Raman spectroscopy of epitaxial TiO2(B) thin films

7.1 Background

The bronze polymorph of titanium dioxide, known as TiO_2(B), has promising photochemical and electronic properties for potential applications in Li-ion batteries, photocatalysis, chemical sensing, and solar cells. In contrast to previous studies performed with powder samples, which often suffer from impurities and lattice water, here we report Raman spectra from highly crystalline TiO_2(B) films epitaxially grown on Si substrates with a thin $SrTiO_3$ buffer layer. The reduced background from the Si substrate significantly benefits acquisition of polarization-dependent Raman spectra collected from the high-quality thin films, which are compared to nanopowder results reported in the literature. The experimental spectra were compared with density functional theory calculations to analyze the atomic displacements associated with each Raman-active vibrational mode. These results provide a standard reference for further investigation of the crystallinity, structure, composition, and properties of TiO_2(B) materials with Raman spectroscopy.

By a modification on the recently reported growth of highly crystalline TiO_2(B) thin films on $SrTiO_3$(STO) substrates,[25] we successfully synthesized high-quality twinned epitaxial TiO_2(B) thin films on STO-buffered Si. Use of Si substrates is advantageous for

characterization by Raman spectroscopic measurements, as the background signal from Si is much weaker than that of STO, and the approach may eventually be useful in integrating such oxide thin films into electronic devices. Based on detailed analysis by high-resolution transmission electron microscopy (HRTEM), the crystallographic orientations of the thin-film structure were characterized, and the high crystallinity and epitaxial growth of the film were confirmed. These results were combined with polarization-dependent Raman spectroscopy and density functional theory results. Polarization-dependent Raman has been shown to be a powerful tool, allowing the unambiguous assignment of the phonon symmetries through direct comparison to theoretical calculations.[135] Furthermore, this approach allows Raman peak positions and intensities to be directly correlated to specific displacements in the crystal when coupled with detailed first-principles calculations of the phonons. The combination of theoretical and experimental results provides a complete set of Raman peaks that we then compare to TiO_2(B) nanopowder data available in the literature. These results can be used to identify preferred orientations,[215-217] analyze strains during inculcation for battery applications,[218-220]and inform future studies of the structure and properties of this promising material.

7.2 Experimental

All films were grown by pulsed laser deposition (PLD) on (100) Si substrates pre-deposited with a 20-unit-cell-thick STO buffer layer grown by molecular beam epitaxy (MBE), as described elsewhere[136]. The ~50 nm thick Ca:TiO_2(B) ($CaTi_5O_{11}$) template layer[25] was deposited from a $CaTi_4O_9$ target made by mixing 80% TiO_2 and 20% CaO powders and dry pressing them into a green body, which was then sintered at 1400 °C.

The TiO_2(B) layer was deposited on the Ca:TiO_2(B) template from a pure TiO_2 target. The vacuum chamber used for PLD had a base pressure $<10^{-7}$Torr. A 248 nm KrFexcimer laser with a pulse duration of 22 ns and a fluence of ~3.4 J/cm^2 was used at a 10 Hz pulse repetition rate for film deposition. The substrate-target distance was 6.35 cm and deposition was carried out at 800 °C in an ambient oxygen pressure of 0.05 Torr. The deposition rate was ~0.01-0.02 Å/pulse. The films studied in this work had thicknesses of 50-200 nm, as measured by a Veeco/Dektak profilometer and via TEM.

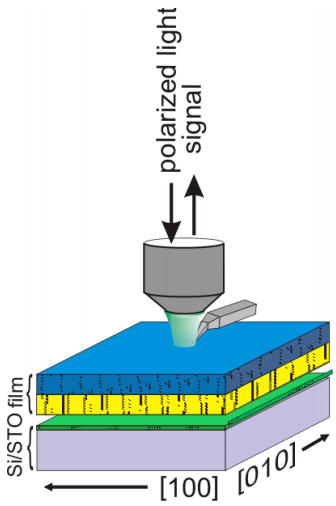

7.1.The experimental Raman setup. Light is collected normal to the TiO_2(B)/Ca:TiO_2(B)/STO/Si film stack.

Raman spectroscopy was conducted using a combined scanning micro-Raman and scanning probe microscope (SPM) using a532 nm diode-pumped solid-state laser with confocal diffraction-limited optics (NT-MDT, Inc.). Both the excitation and collection of the signal were normal to the sample though the same objective lens. The polarization of the input light was controlled using a half-wave plate, and the depolarized light was collected using a linear polarizer at 90° to the input polarization. Atomic force

microscope (AFM) images were collected with the same instrument. The cantilever detector laser is a 1064 nm low-power diode. For the spectral range measured, any sum frequency effects are removed by the edge filter. In addition, spectra were taken with the IR laser both on, and off, and no difference was detected between the spectra. The experimental setup is shown in Fig. 7.1. HRTEM imaging was carried out with a JEOL 3011 TEM, and a JEOL 3100R0.5 equipped with a spherical aberration corrector was used for scanning transmission electron microscopy(STEM) imaging. In order to compare with the available literature, peak positions were extracted from reported data after digitization and calibration of the x-axis scale for all of the spectra using image processing software (ImageJ) and free scripting utilities including SciPy and matplotlib.

Theoretical vibrational frequencies were calculated from first principles with density functional perturbation theory[130] in the local density approximation[131]. All calculations were performed with the plane-wave norm-conserving pseudopotential method, as implemented in the Quantum Espresso software package.[132, 221, 222] A semi-core Ti pseudopotential including the 3s and 3pelectrons in the valence was used, requiring a 200 Ry plane-wave cutoff energy and 4×4×4 k-point mesh to converge the total energy within 1 mRy/atom[223]. With these parameters, the Raman-active optical phonon frequencies were converged to within 10 cm^{-1}.

7.3 Results and Discussion

TiO_2(B) films were grown epitaxially on ~50 nm thick (001) Ca:TiO_2(B) template films, which were previously grown on STO-buffered undoped (001) Si substrates. The film and details of its structure are shown in Fig. 7.2. Selected area diffraction shows clear alignment and epitaxy between all of the layers and the substrate. Within a grain,

HRSTEM images clearly show the epitaxy between the TiO_2(B) and the template layer. The images compare well with the atomic model in Fig. 7.2A, and it is clear the material is well crystallized with few defects. Overall, the film is twinned; the epitaxial relationship between the TiO_2(B), the template layer, and the STO buffer layer restrict the possible orientations of crystallites in the film. The TiO_2(B) grows with the [100] direction aligned to the [100] direction of the Ca:TiO_2(B) template, while the template grows on a (001) face of STO. In the TEM specimen imaged along the [100]zone axis of Si, bronze grains are seen on either a [100] (a-axis) or [010] (b-axis) zone axis with the [001] (c-axis) normal to the film, or along a [100] zone axis, but rotated 90° with the b-axis normal to the film. Grains with the b-axis normal to the film are not found in films grown on a bulk STO substrate.[25]The rotated grains originate in the buffer layer, where the template film begins to grow on the (110) face of a tilted STO grain. Figure 7.2D shows the base of a tilted bronze grain where the template layer nucleates on the (110) face of a tiny STO grain, which is visible in the HAADF image. The rotated TiO_2(B) grains protrude from the surface, being typically ~10-15 nm taller than the rest of the film. AFM analysis of the film surface shows that ~50% of the surface is populated by each of the two orientations of TiO_2(B) grains(Fig. 7.2F). Therefore, it is expected that both orientations will contribute to polarization-dependent Raman spectra. A few anatase inclusions (Fig. 7.2E) which are 1-4 unit cells thick along the high-energy$(\bar{2}01)$face of TiO_2(B), corresponding to the (103) face of the anatase[224], also exist, but they were not sufficiently numerous to appear in either the XRD pattern (shown in Fig. 7.6) or the Raman spectra of the film. Additional high-resolution STEM images of the interfaces in the film stack, and EDS and EELS spectroscopy are provided in Fig. 7.7 and 7.8. Atomic

resolution imaging indicates only TiO_2(B) and Ca:TiO_2(B) crystals are present in the film. EDS linescans show no significant migration of Si into the titanium oxides films, and EELS data suggest all of the titanium is in the Ti^{4+} state, ruling out the presence of oxygen-deficient Magneli phases[225].

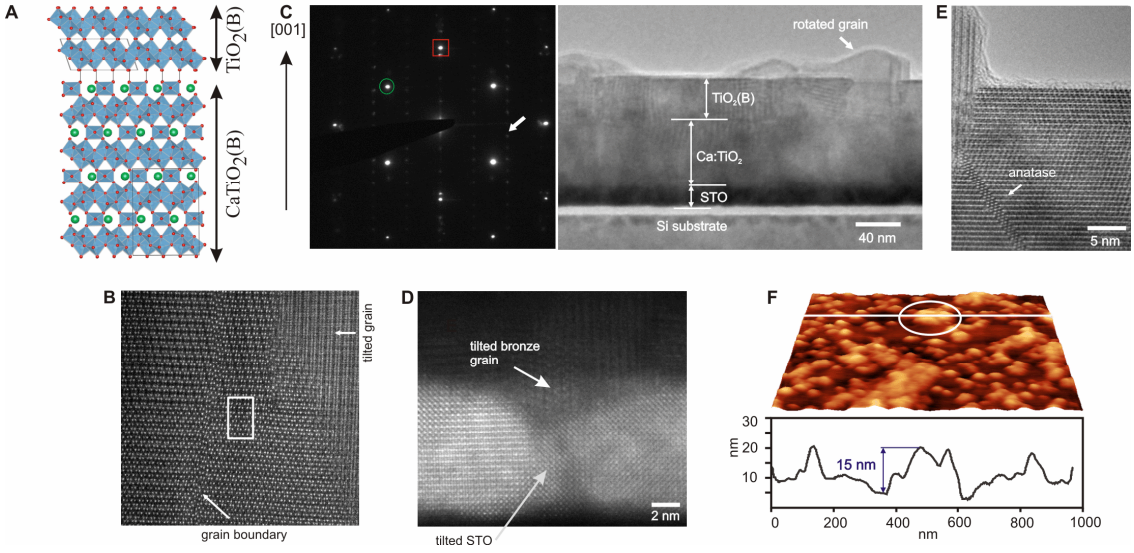

7..2 TEM and AFM images confirming the structure of the TiO2(B) film grown on STO-buffered silicon. (A) Structural model of the TiO_2(B) film and Ca:TiO_2(B) template layers that normally grow on (100)STO. (B) HRTEM of the interface between film and template showing high crystallinity and epitaxy of the layers viewed on a [010] axis. The inset shows a selected area diffraction pattern covering the film stack, where the square is the STO [002] spot, the circle marks the Si [-11-1] spot, and the arrow indicates the bronze pattern. The three diffraction patterns are aligned along the <001> direction. The white box in B corresponds to the model shown in A. An out-of-phase boundary and a tilted grain viewed along the [100] axis are also shown. (C) HRTEM of the complete film stack showing the STO buffer (~10nm thick), Ca:TiO_2(B) (~ 50 nm thick), and TiO_2(B). The TiO_2(B) film consists of crystallites of two orientations related by a rotation twin, with one population oriented with the c-axis perpendicular to the film and the other rotated by 90 degrees with the b-axis along the perpendicular direction. (D) HAADF image of the interface between the template layer and the STO buffer, which shows that the taller, tilted grains are also epitaxial, but originate from tilted crystallites in the STO buffer layer. (E) HRTEM showing an anatase inclusion. (F)AFM scan of the surface of the film, showing that the taller, tilted grains cover ~50% of the surface.

Raman spectra from the epitaxialTiO_2(B) thin film grown on silicon are shown in Fig. 7.3.The Raman signal obtained from this thin film is relatively strong, possibly attributable to the difference in crystal structure between cubic silicon and orthorhombic TiO_2(B). Spectra were collected with the incident polarization perpendicular to the

analyzer polarization(depolarized spectra), minimizing the signal collected from the Si substrate.

In an attempt to sample all of the available Raman modes, the polarization of the incident light was rotated with respect to the sample. The polarization-dependent Raman spectra from the TiO_2(B)/Ca:TiO_2(B)/STO/Si thin-film stack with the polarization of the light along the [100] and the [110] directions of Si are shown in Fig. 7.3A. The spectra vary because the intensity of the Raman response is dependent upon the angle between the polarization of the input light and the crystal axes. There is also a dependence on the mode symmetry and collection of polarized light. The symmetric A_g-typemodes would be expected to appear weaker when collecting depolarized light, while the asymmetric B_g-typemodes in the orthorhombic TiO_2(B) crystal would tend to scatter more intensely. Coincidentally, the intensity of scattered light is higher when the input polarization is aligned to the active vibrational displacement in the crystal. This means the strong scattering angle for some modes in the TiO_2(B) crystal can be found by rotating the crystal, while collection of the depolarized light reduces the intensity of the substrate (Si) background. This arrangement does attenuate scattering from the A_g-typemodes somewhat, but most are visible in the spectrum. This is due, at least in part, to the fact that the input polarization is not perfect due to the use of a high-power objective lens.

Together, the two spectra shown in Fig. 7.3A account for the complete set of measured Raman-active modes. As the film structure is somewhat complicated, the contribution of different interface types must be addressed. Firstly, the very good agreement between the peak positions calculated from first principals and the experimental spectra indicates that interface effects are weak. The crystal domains in the film, seen in Fig. 7.2, form a small

fraction of the total possible scattering volume and may slightly shift the modes, but no modes are shifted beyond the confidence range of the calculated positions. Since TiO_2(B) requires a Ca:TiO_2(B) template to grow, it is important to clarify the contribution from the template layer and thin film interfaces. Figure 7.3B shows the Raman spectrum of a pure Ca:TiO_2(B) template layer deposited on the same STO/Si substrate, collected under identical conditions. The Ca:TiO_2(B) material shows a low overall scattering intensity. A peak near the strongest peak of Ca:TiO_2(B) at 214 cm^{-1}does appear in the TiO_2(B)/Ca:TiO_2(B)/STO/Si spectrum. As this peak does not exist in the calculated TiO_2(B) spectrum, it must originate from either the Ca:TiO_2(B), or is a local mode associated with the interface between the Ca:TiO_2(B) and the TiO_2(B) layers. Similarly, it is also important to consider the contribution from the STO buffer layer. Figure 7.3C compares the measured TiO_2(B) Raman spectrum to that of the STO/Si substrate, collected under the same conditions. These data confirm that the STO/Si substrate has a minimal background contribution to the TiO_2(B) film spectrum, with the strongest peak at ~522cm^{-1}, and weaker peaks at ~310cm^{-1} and ~620 cm^{-1}. There is no apparent contribution from the very thin STO layer or the interface between the STO andthe template layers, which is advantageous as STO has a very strong Raman background in bulk. Anatase, which overlaps the ~148 cm^{-1} peak of TiO_2(B) and has smaller peaks at 400, 500, and 620 cm^{-1}, was found to have a much smaller Raman cross section than TiO_2(B) (from comparable measurements made on a thin film of anatase), and thus the small inclusions present in our film (Fig. 7.2E) also do not contribute to the background. The main features of the measured spectra thus are a strong peak at 200 cm^{-1}, a number of smaller peaks between 300 and 500 cm^{-1}, and a broad peak at ~630 cm^{-1}.

We also performed first-principles calculations to determine the vibrational modes of TiO_2(B) and compare to experimental Raman spectra. To test the accuracy of the computational approach, Raman spectra were first calculated for rutile and anatase TiO_2, and they were found to be in good agreement with experiments[226], within 10 cm^{-1} for anatase and 20 cm^{-1} for rutile. The calculations for TiO_2(B) are expected to have similar accuracy. Measured and DFT calculated Raman peak positions for TiO_2(B) are compared in the first two columns of Table 7.1, exhibiting an average deviation of 5 cm^{-1}.

Peak positions measured from published spectra acquired in TiO_2(B) powders are also listed in Table 7.1 for comparison.[15, 16, 18, 22, 74-76, 227-229] Literature peak positions were assigned to a row in the table based on the nearest calculated peak position. The calculated peaks at 190 $cm^{-1}$and 196 cm^{-1}seem to appear as a single peak between 194 and 210 cm^{-1} in these reports. Similarly, calculated peaks at 651 $cm^{-1}$and 666 cm^{-1} may be either split or combined in a single peak in experimental data, depending on the material synthesis.

Table 7.1Summary of the calculated Raman-active phonon-mode frequencies and mode assignments compared to experimental Raman spectra. Average and standard deviation values are computed from the literature experimental data.

DFT		Film	Literature Experimental Data (cm^{-1})												Statistics	
Mode Sym.	TiO_2 (B)	TiO_2 (B)	bulk[2]	NW[2]	micro-flower[21]	powder[22]	Milled powder[6]	Poly-film[23]	NW[19]	NW[18]	NW[43]	NW[44]	powder[45]	Platelet[45]	AVG	DEV
B_g	128	126				118	123	118	123	124	123	122	123	121	122	2
A_g	146	146				144		140	147	149	149	145	146		145	3
A_g	152	165						157							153	6
A_g	190	194														
B_g	196	200	200	200	210	195	196	195	196	196	196	194	197	204	198	5
B_g	224	239	241	238	232		238	235		238		240	236	234	236	2
B_g	248	254	255	256	257	242	250	250	244	250	246	248	249	258	253	4
A_g	285	289	299	298		292	295	290	294	295	297	293	295		295	3
A_g	365	365	365	368		362	364	362	366	370	238		379	382	367	7
A_g	383	380			380										380	
A_g	407	405 *	409	413		405	407	405		411	412	402	410		408	4`
A_g	443	435 *	437	437	422	434	433	433	432	431			431	431	432	4
A_g	485	472		474	477	469	473	471	467	470	470	470	468	477	472	3
B_g	490	492							511			513			512	2
A_g	558	556 *	554	556	552	545	550	551	552	564	552		552	553	553	5
A_g	651		636	640	633	631	636	633	636	636	644	638	636	634	636	3
B_g	666	660	662	659	657	659	659	662		656			655		659	3
					826									828	827	1
A_g	859		859	858		864	855		858	860			860	872	858	2
				1000	925									922	949	44

* taken from off-axis spectrum

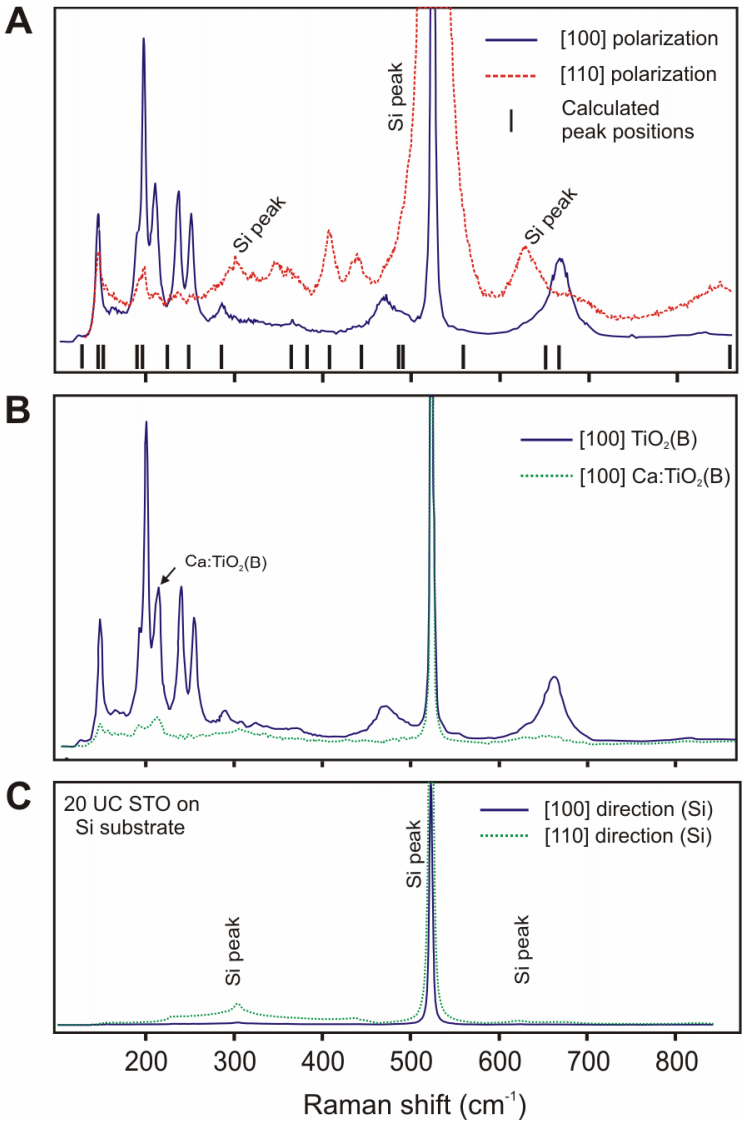

7.3 Raman spectra of the TiO_2(B) films. (A) Raman spectra with light polarized along the [100] and[110] axes of Si. The calculated peak positions are also denoted. Spectra were taken consecutively under the same conditions.(B) Comparison of spectra taken under identical conditions for the TiO_2(B)/Ca:TiO_2(B)/STO/Si film stack and for a Ca:TiO_2(B)/STO/Si film of similar thickness. The Ca:TiO_2(B) has lower overall intensity and contributes little signal to the TiO_2(B) film spectrum, though it likely accounts for the peak at ~214 cm^{-1}. (C) Raman spectrum from the bare STO/Si substrate shows a low background, except for the main 522 cm^{-1} peak and weak peaks at 302 $cm^{-1}$and 623 cm^{-1}. The substrate peaks are more prominent for incident polarization along the [110] axis of Si.

The normalized intensities of the Raman peaks from our thin film and literature data are compared in Fig. 7.4. Peak positions and intensities show considerable variation in the published spectra. Some portion of this can be attributed to experimental differences, as a variety of instruments, excitation wavelengths, and geometries were used to collect the spectra. While this may introduce some variation in the measured intensities, a qualitative comparison is still useful, and the peak positions are not expected to change significantly. The spectra obtained from the literature span a wide range of preparation methods and particle morphologies, including nanoparticles, nanowires, microflowers, and platelets. For example, in the report from Armstrong *et al.*,[18] both bulk (bottommost literature spectrum) and nanowire spectra are provided. Xiang *et al.*[229]provided spectra for both platelets, where adsorption of ethylene glycol was used to control the crystal growth (topmost spectrum), and nanoparticles. In particular, the microflower[74] and platelet[229] materials show very similar spectra, including several peaks at high wavenumbers that are not present in the nanowires, nanoparticles, thin film samples, or calculated Raman spectrum results. This indicates a chemical difference in the platelet-like powders compared to pure TiO_2(B) crystals, or materials prepared by other methods.

By combining the measured Raman peak positions and calculated atomic displacements, we have qualitatively examined the variation of the intensity of each Raman peak with respect to the optical polarization. The calculations indicate that vibrations at 196, 224, 248,285, 485, and 666 cm^{-1}involve atomic displacements along the [100] crystal axis and should therefore be strongest for incident polarization along the [100] direction. This agrees well with the experimental data, as seen in Fig. 7.3A. Phonon

modes associated with peaks between 300 and 450cm^{-1} are generally A_g-type modes and therefore appear weak for light polarized along the [100] axis of the crystal. The expected peak at 859cm^{-1} is off-axis with respect to both the a- and c-axes, and is therefore very weak in all spectra.

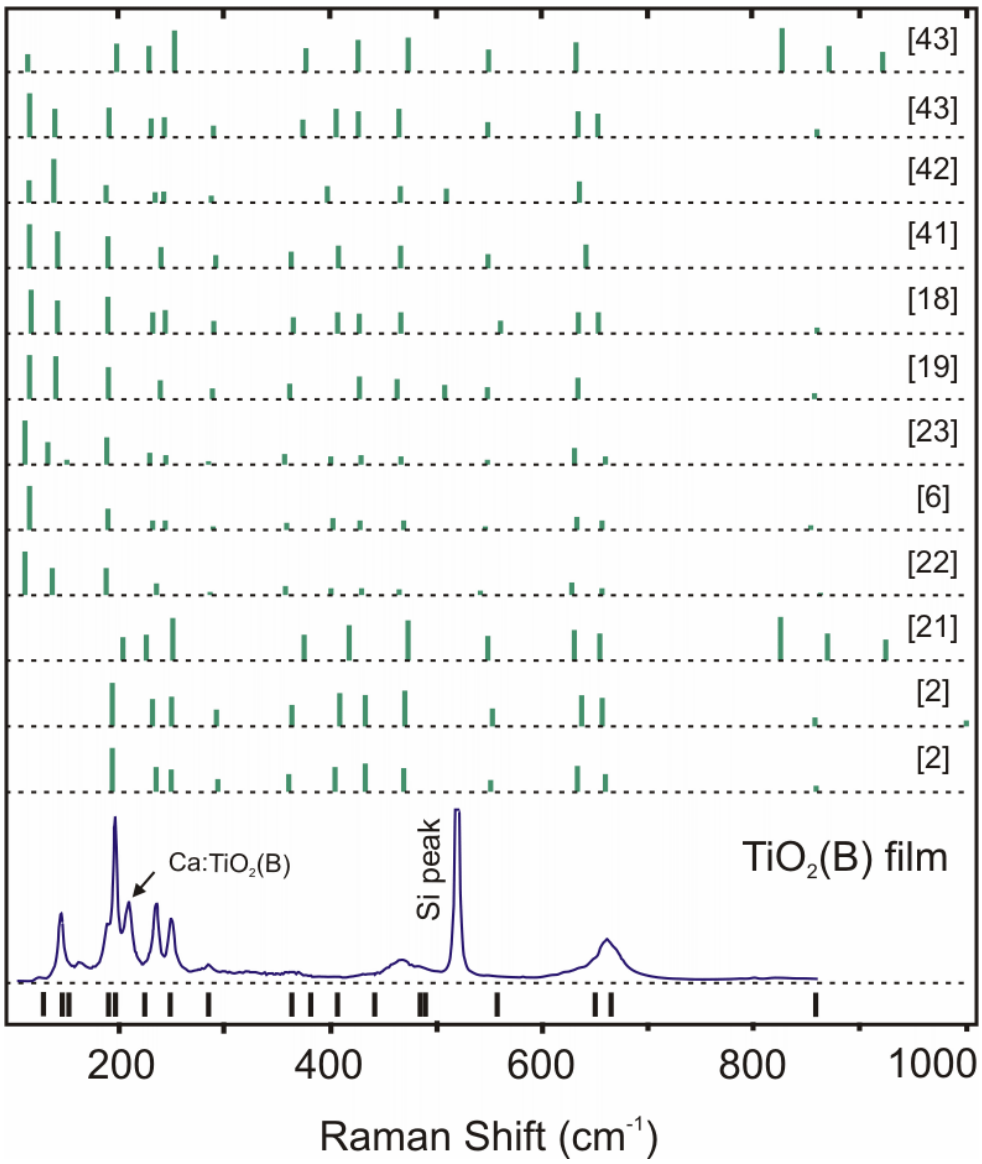

7.4 Comparison of the measured and calculated TiO_2(B) film Raman spectra with data from the literature. The experimental spectra from the literature were digitized and the peak positions and normalized intensities were determined. The thin-film Raman spectrum and the calculated peak positions (bottom black vertical lines) appear at the bottom.

The theoretical results reveal that the experimentally measured broad peaks near 485 and 666cm^{-1} each consist of two closely spaced peaks at 485/490 and at 651/666cm^{-1}, respectively. The peak at 651cm^{-1} should be strong with light polarized along the a-axis, while the peak at 666cm^{-1}should be strongest when light is polarized close to the c-axis of the crystal. The combination of these two modes may account for the width of the peaks, which is corroborated by examining the Raman peak intensity as the polarization is rotated with respect to the crystal axis (Fig. 7.5A).In the figure, a set of spectra was taken at one degree intervals as the incident polarization was rotated relative to the in-plane TiO_2(B) crystal axes. The intensities of the most prominent TiO_2(B) peaks decrease smoothly as the polarization is rotated from [100]towards [110], and the peaks re-appear as the polarization approaches [010]. In between these two orthogonal axes, the substrate signal significantly increases. There are also several smaller peaks which correspond to the TiO_2(B) structure, whose intensities reached a second maximum with excitation along[110]. Some peaks vary with more than one maximum over the rotation.

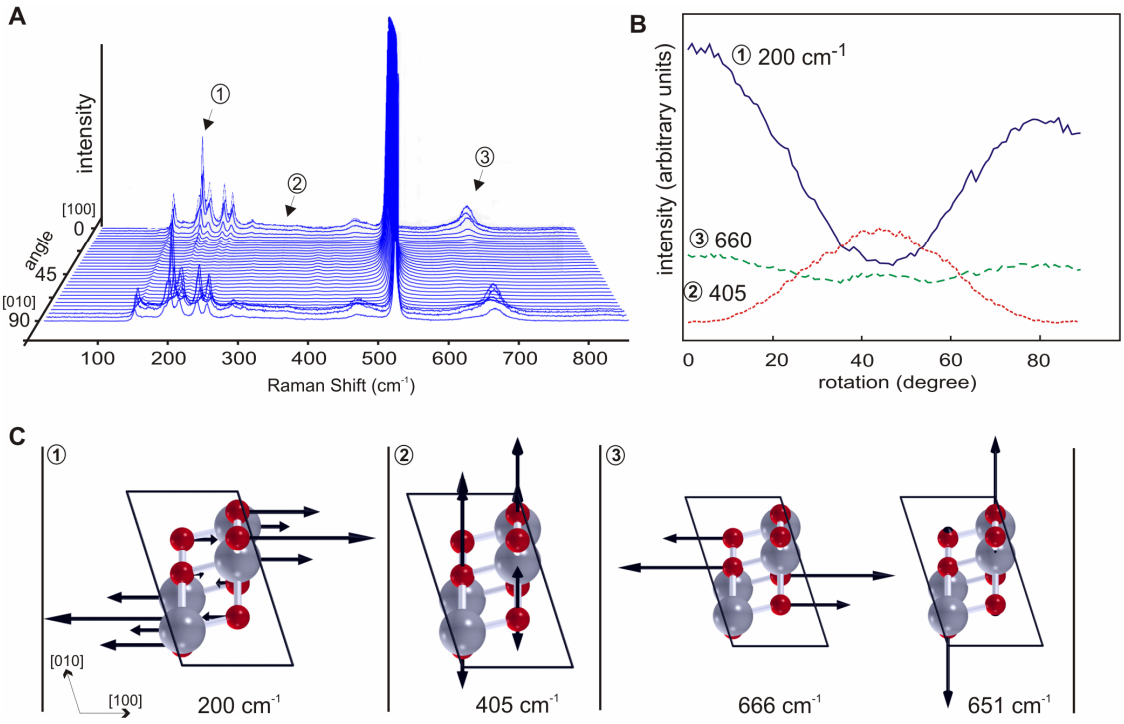

7.5.Polarization-dependent Raman spectra of TiO_2(B).(A) Thirty spectra with in-plane angles of rotation between 0° and 90°with respect to the *a*-axis of the TiO_2(B) film. (B) The normalized peak-height change of threeTiO_2(B) peaks (at 200 cm^{-1}, 405 cm^{-1}, and 660 cm^{-1}) as the incident polarization is altered. (C) Calculated atomic displacements for the phonon modes corresponding to each of the three peaks. For peak (1) the displacements are along the *a*-axis of the film and coincident with the optical polarization, while for peak (2) the atoms are displaced along the *b*- and *c*-directions, and the peak is therefore most visible off-axis. Peak (3) is broad and involves two different vibrational modes, one along the *a*- and one along the *b*- and *c*-axes, resulting in the triple peak in (B).

The thorough analysis of the correspondence between the theoretical results and the polarization-dependent Raman spectra improves the reliability of our mode assignments. Figure 5.5B shows the peak intensity as a function of the rotation angle between [100] and the polarization of the incident light for three selected Raman peaks. The change of intensity can be related to the alignment of the polarization to the direction of the atomic displacements associated with the phonon vibrations that produce the Raman response. The theoretical atomic displacements involved with each phonon mode for the three peaks in Fig.7.5B are shown in Fig. 7.5C. The broad peak corresponding to the theoretical lines at 651 and 666 cm^{-1} shows three intensity peaks, corresponding to a

polarization along either the [100] or$[00\bar{1}]$ directions. These are due to contributions from the two different phonon vibrations noted in the theoretical spectrum. The polarization dependence allows the two different modes to be identified though they appear as a single peak experimentally.

7.4 Summary

In summary, we have grown TiO_2(B) epitaxially on a novel Ca:TiO_2(B) template on $SrTiO_3$-buffered Si substrates, which were examined in detail using TEM and Raman spectroscopy. A review of Raman spectra on nanostructured TiO_2(B) materials shows considerable variation among the reports, and these were compared to our highly crystalline thin-film samples. First-principles calculations were carried out to produce reference spectra, which enabled us to uncover the symmetry and direction of atomic displacements of all Raman-active modes in TiO_2(B). Our results provide an essential reference for the characterization of crystallinity, composition, and structure in TiO_2(B), and may aid in the development of new applications for this material.

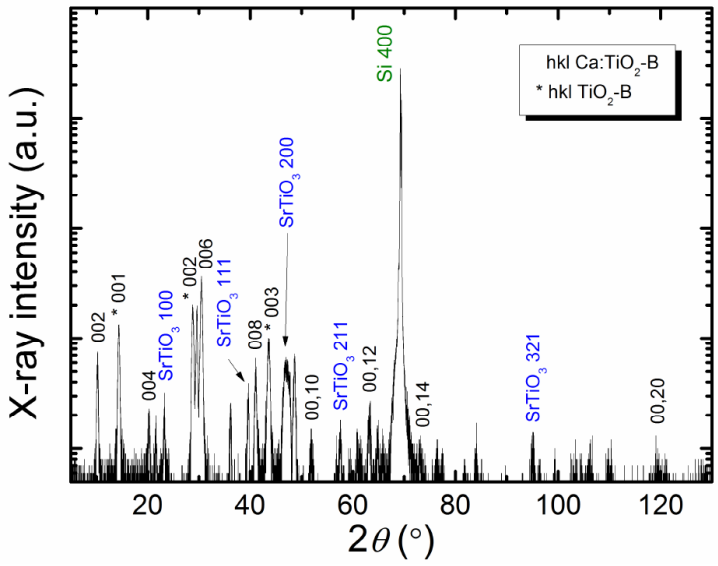

7.6 X-ray diffraction confirming the presence and crystallinity of the TiO_2(B) phase. The Ca:TiO_2(B) phase is also present. No strong peaks from anatase or any other TiO_2 phases were found. The additional $SrTiO_3$ peaks are due to the polycrystalline nature of the buffer layer. These other orientations in the buffer layer seed the two distinct orientations seen in the TiO_2(B) film.

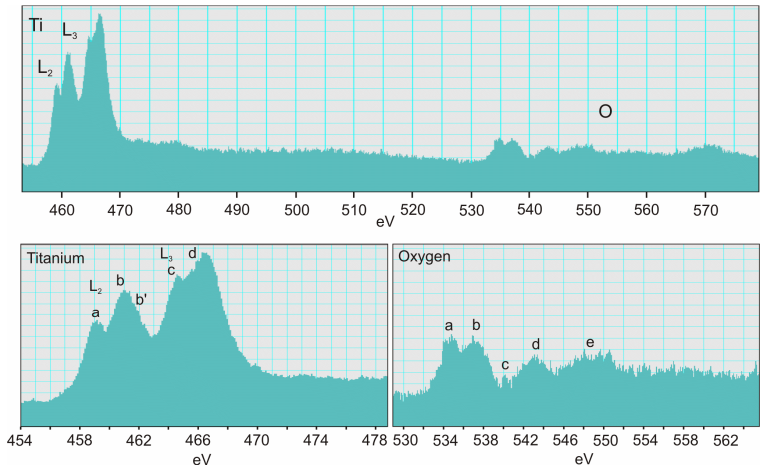

7.7 EELS data for TiO_2(B) thin film stack. In accordance with Stoyanovet *et al.* [230], the L_2 and L_3 titanium edges and the higher intensity of the (a) oxygen edge with respect to the (b) oxygen edge indicates the titanium is primarily in the Ti^{4+} oxidation state. This is consistent with TiO_2(B), but not with Magneli or other titanium oxide phases with mixed Ti^{3+} and Ti^{4+} valences and matches well with HAADF imaging data that only indicate the presence of the TiO_2(B) and template Ca:TiO_2(B) phases

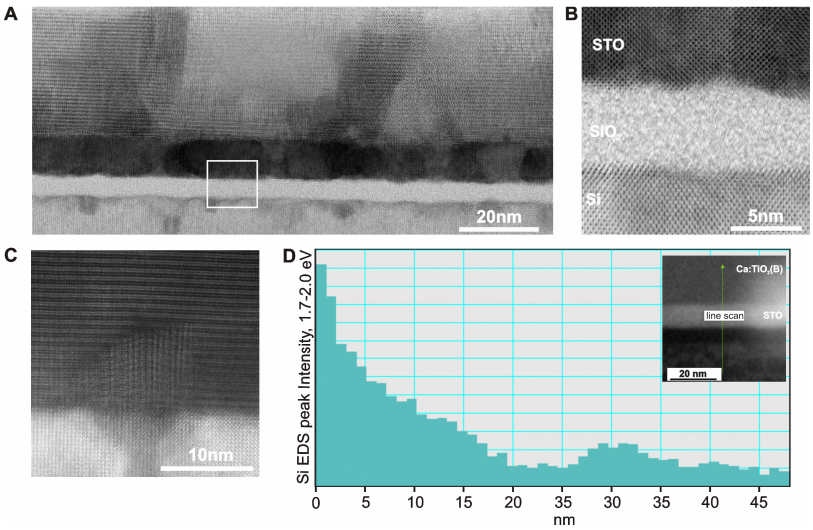

7.8 HRSTEM images of the TiO_2(B)/Ca:TiO_2(B)/STO/Si film. A) is a bright field STEM image of the film stack showing some overlap between crystal domains B) is a BF image of the interface between the silicon and STO buffer layers. A very thin SiO_2 layer is present that appears to have formed during deposition of the buffer layer C) shows an atomic resolution HAADF image illustrating that the small crystallites at the base of the film are also the bronze phase, as seen by the distance between the atomic planes D) is an EDS line scan across of the Si peak across the Si/STO/Ca:TiO_2(B) interfaces. There is little indication of the presence of Si in the template or TiO_2 films, which corroborates the TEM observations that indicate the film does not contain extraneous phases. The increase in the Si signal in the STO region is due to the overlap between the Si K peak and the Sr L edge and the slow rise in signal over the silicon is due to the increasing thickness of the substrate.

Chapter 8

Summary and future work

8.1 Summary

A broad theme of all of this work is the attempt to correlate advanced microscopy methods including transmission electron microscopy, scanning probe microscopy, and optical spectroscopy on the same materials and even the same specimens to obtain complimentary measurements in the hope that these would reveal new details about structure-property relationships measured on a nanometer scale. Combining measurements not only corroborates the information obtained from any particular method, but also compensates for deficiencies of any single technique. One example would be the difference in area that can be sampled by TEM at high resolution, which is very small and may be altered by thinning the sample to electron transparency, and SPM which can cover micron scales but has difficulty resolving atomic scale detail. Here, this approach is applied to investigate several means of controlling domain structures in BFO and for characterizing novel materials such as TiO_2(B). Finally, in order to incorporate multiple microscopy methods into a TEM stage, including electrical probing, STM, and optical excitation and spectroscopy, a pair of specimen holders were designed, constructed and are demonstrated here.

It is known from previous work that domain structures in ferroelectric oxides control many of the important properties. In multiferroic BFO, these include resistance, selective

conductivity, surface charge, and magnetic exchange coupling. Through the application of TEM, SPM, and optical techniques, it was discovered that the decrease with film thickness of the depolarization field in BFO drives a quasi-phase change from a 109°striped domain structure to a 71° striped domain structure; occurring at film thicknesses between 100 and 200 nm. In between these lengths, the appearance of a 'mushy zone'(by analogy to metallurgy) mixed domain structure was confirmed. I also found that 100 and 200 nm films show different switching characteristics, likely related to this structure change.

Another route to approach domain engineering in thin films is through the application of misfit strain. Though the films were grown under the same conditions for the same time, there were also coincident changes in film thickness for different substrates, with higher misfit producing thinner films. However, the domain structures were surprisingly similar. Two clear trends in domain width and variability as a function of misfit strain appeared for these BFO films grown on pseudoperovskite substrates with different epitaxial misfit strains. Domain widths fall as strain moves from compressive towards tensile with the narrowest domains, and therefore highest domain densities, at high tensile strain. This indicates that some of the misfit strain energy is relaxed by forming additional domain walls when the sample is strained in tension. The variation in domain width also showed a strong correlation with misfit strain, peaking for low misfits and increasing for both compressive and tensile strains. Apart from these trends, two particular thin film/substrate systems showed anomalous behavior. Films grown on NGO and SSO substrates had unique domain configurations, potentially indicating unusual

properties, and BFO thin films grown on these substrates would be good candidates for future investigation.

Beyond this, the introduction of certain types of defects in BFO, that result from changes in stoichiometry during growth, have long-range effects on the ferroelectric properties. Linear defects that form in conjunction with a metastable layered phase stabilize 109° domains at the expense of 71°domains due to charge on the defect and the strain it introduces into the surrounding material. The strain seems to have a very local effect, creating nanodomains, while the charge completely alters the domain structure in the film and stabilizes charged domain boundaries. This defect-mediated structure was discovered through the combination of TEM and PFM studies that allowed mapping of cross-sectioned specimens from the thick edge of a TEM specimen covering over 20 microns of interface between electron transparent region and the edge of the ion-polished region, rather than the ~1 um in TEM alone.

Further, SPM, TEM, Raman spectroscopy, and theoretical calculations were applied to make detailed study of unique thin film TiO_2(B) battery material grown on silicon substrates. The combination of methods allows correlation of the crystallographic details of the film to the Raman scattering modes. This kind of analysis could be very significant both for using polarized Raman for phase identification and examining small structural details, and for future in-situ experiments where the material's battery performance and the electrochemistry of charging could be studied in real time.

To further explore the application of complimentary microscopy methods, I also undertook the design and construction of a new experimental specimen rod platform for *in-situ* TEM studies. *In-situ* TEM is one of the few methods where the electronic

properties of nanoscale structures such as domain walls, or the atomic-scale effects of charging a battery material can be measured directly and unambiguously. In addition, to explore the potential of these materials for photo-active devices such as photovoltaics and to use spectroscopy to watch reactions occur in real time in a photocatalalyst such as TiO_2(B), optical excitation is needed. To this end two specimen rods were built and their capabilities for in-situ work were demonstrated on model systems.

8.2 Future work

There are several directions in which this work can be extended. The first is to explore the idea of controlling the introduction of the linear defects into BFO thin films, both to control domain structures and to examine the properties of the defects themselves. Similarly, the metastable layered phase in the particles may also have useful properties themselves, or when incorporated with $BiFeO_3$. In terms of thin films and strain, the combination of these two factors open a wide parameter space for optimizing domain structures for specific applications. Similarly, the very unusual domain structures in BFO grown on SSO and on NGO should be further explored, particularly in terms of their switching and magnetic properties.

The most obvious avenues for future work rests in the *in-situ* platform. With further refinement, it enables a kind of nanoscale characterization that is hitherto unavailable for photovoltaic and photocatalytic systems, such as the titanium oxide films and BFO thin films featured in this work. With the combination of so many functionalities on this experimental platform, it is not difficult to imagine new and interesting applications for this technology. Such possibilities are really too numerous to list in detail, but carrying forward from the ferroelectrics work, there is an opportunity to quantitatively explore the

electronic functionalities of domain walls, as well as potential for ferroelectric materials as photovoltaics by nanoscale probing of the photocurrent at defects and domain walls.

Another avenue offered from the work presented here comes from polarization-dependant Raman spectroscopy, particularly when coupled with first principals modeling. This technology using visible light is capable of extracting structural details from crystals that rival much more complex X-ray systems, where results from real-world materials can now be compared to first principles calculations for identification, or to extract additional information. Further refinement of the calculations to get the Raman intensities would yield a powerful new tool for examining structure in crystals. Finally, this work has explored several means of controlling ferroelectric properties in BFO, and the logical extension is to use these mechanisms coupled with the in-situ platform to further explore the potential of domain boundaries as nanoscale ferroelectric devices.

Bibliography

1. Schlom, R.R.a.D.G., *Whither Oxide Electronics?* MRS Bulliten, 2008. **33**: p. 1006-1014.
2. Seidel, J., et al., *Conduction at domain walls in oxide multiferroics.* Nature Materials, 2009. **8**(3): p. 229-234.
3. Guo, R., et al., *Non-volatile memory based on the ferroelectric photovoltaic effect.* Nat Commun, 2013. **4**: p. 1990.
4. Chu, Y.-H., et al., *Controlling magnetism with multiferroics.* Materials Today, 2007. **10**(10): p. 16-23.
5. Catalan, G., et al., *Domain wall nanoelectronics.* Reviews of Modern Physics, 2012. **84**(1): p. 119-156.
6. Wang, D., et al., *The effect of dipole moment and electron deficiency of analytes on the chemiresistive response of TiO_2(B) nanowires.* Analyst, 2011. **136**(20): p. 4179-82.
7. Wang, D., A. Chen, and A.K. Jen, *Reducing cross-sensitivity of TiO_2-(B) nanowires to humidity using ultraviolet illumination for trace explosive detection.* Phys Chem Chem Phys, 2013. **15**(14): p. 5017-21.
8. Wang, D.L., et al., *Room-Temperature Chemiresistive Effect of TiO_2 - B Nanowires to Nitroaromatic and Nitroamine Explosives.* Ieee Sensors Journal, 2011. **11**(6): p. 1352-1358.
9. Wang, G., et al., *Photoelectrochemical study on charge transfer properties of TiO_2-B nanowires with an application as humidity sensors.* Journal of Physical Chemistry B, 2006. **110**(43): p. 22029-22034.
10. Kemmitt, T., et al., *Transparent, photocatalytic, titania thin films formed at low temperature.* Current Applied Physics, 2013. **13**(1): p. 142-147.
11. Thomas, J. and M. Yoon, *Facile synthesis of pure TiO_2(B) nanofibers doped with gold nanoparticles and solar photocatalytic activities.* Applied Catalysis B: Environmental, 2012. **111-112**: p. 502-508.
12. Yu, C., et al., *Synthesis and characterization of Ag/TiO_2-B nanosquares with high photocatalytic activity under visible light irradiation.* Materials Science and Engineering: B, 2013. **178**(6): p. 344-348.
13. Zukalová, M., et al., *Electrochemical and gas-phase photocatalytic performance of nanostructured TiO_2(B) prepared by novel synthetic route.* Progress in Solid State Chemistry, 2005. **33**(2-4): p. 253-261.
14. Jo, H.J., et al., *Improved performance of dye-sensitized solar cells with novel conjugated organic dye using aluminum oxide-coated nanoporous titanium oxide films.* Journal of Power Sources, 2014. **249**: p. 385-391.
15. Qi, L., C. Li, and Y. Chen, *Dye-sensitized solar cells based on nitrogen-doped TiO2–B nanowire/TiO_2 nanoparticle composite photoelectrode.* Chemical Physics Letters, 2012. **539-540**: p. 128-132.

16. Qi, L., Y. Liu, and C. Li, *Controlled synthesis of TiO_2-B nanowires and nanoparticles for dye-sensitized solar cells.* Applied Surface Science, 2010. **257**(5): p. 1660-1665.
17. Tsai, C.-C., Y.-Y. Chu, and H. Teng, *A simple electrophoretic deposition method to prepare TiO2–B nanoribbon thin films for dye-sensitized solar cells.* Thin Solid Films, 2010. **519**(2): p. 662-665.
18. Armstrong, A.R., et al., *TiO_2-B Nanowires.* Angewandte Chemie, 2004. **116**(17): p. 2336-2338.
19. Armstrong, A.R., et al., *TiO_2-B nanowires as negative electrodes for rechargeable lithium batteries.* Journal of Power Sources, 2005. **146**(1-2): p. 501-506.
20. Brutti, S., et al., *TiO_2-(B) Nanotubes as Anodes for Lithium Batteries: Origin and Mitigation of Irreversible Capacity.* Advanced Energy Materials, 2012. **2**(3): p. 322-327.
21. Huang, J.P., et al., *Electrochemical sodium storage of TiO_2(B) nanotubes for sodium ion batteries.* RSC Advances, 2013. **3**(31): p. 12593.
22. Kim, B.R., et al., *Electrochemical properties of the TiO2(B) powders ball mill treated for lithium-ion battery application.* Chemistry Central Journal, 2013. **7**.
23. Liu, Z., et al., *Nanostructured TiO_2(B): the effect of size and shape on anode properties for Li-ion batteries.* Progress in Natural Science: Materials International, 2013. **23**(3): p. 235-244.
24. Ren, Y., et al., *Nanoparticulate TiO2(B): An Anode for Lithium-Ion Batteries.* Angewandte Chemie-International Edition, 2012. **51**(9): p. 2164-2167.
25. Kui Zhang, M.B.K., Baihai Li, Sung Joo Kim, Xianfeng Du,Xiaoguang Hao, Jacob R. Jokisaari, Shuyi Zhang, George W. Graham, Bart M. Bartlett, Xiaoqing Pan1, *Waterless Epitaxial TiO_2-B Thin Films for Superfast Lithium Ion Transport* In Press, 2014.
26. Bleloch, A. and A. Lupini, *Imaging at the picoscale.* Materials Today, 2004. **7**(12): p. 42-48.
27. Hetherington, C., *Aberration correction for TEM.* Materials Today, 2004. **7**(12): p. 50-55.
28. Scott, J.F., *Nanoferroelectrics: statics and dynamics.* J Phys Condens Matter, 2006. **18**(17): p. R361-86.
29. Damjanovic, D., *Ferroelectric, dielectric and piezoelectric properties of ferroelectric thin films and ceramics.* Reports on Progress in Physics, 1998. **61**: p. 1267-1324.
30. Kumar, A., et al., *Multiferroic Memory: A Disruptive Technology or Future Technology?* Solid State Phenomena, 2012. **189**: p. 1-14.
31. I. C. Infante, S.L., B. Dupe, M. Bibes, S. Fusil, E. Jacquet, G. Geneste,S. Petit, A. Courtial, J. Juraszek, L. Bellaiche, A. Barthelemy, B. Dkhil, *Bridging Multiferroic Phase Transitions by Epitaxial Strain in BiFeO3.* Physical Review Letters, 2010. **105**: p. 057601.
32. Chengliang Lu, W.H., Yufeng Tian, and Tom Wu, *Multiferroic oxide thin films and heterostructures.* Applied Physics Reviews, 2015. **2**: p. 021304.

33. C. R. Bowen, H.A.K., P. M. Weaver and S. Dunn, *Piezoelectric and ferroelectric materials and structures for energy harvesting applications.* Energy Environ. Sci., 2014. **7**: p. 25-44.
34. Scott, J.F., *Applications of modern ferroelectrics.* Science, 2007. **315**(5814): p. 954-9.
35. Hiroyuki Yamada, V.G., Ste´phane Fusil, So ren Boyn, Maya Marinova, Alexandre Gloter, Stephane Xavier, Julie Grollier, Eric Jacquet, Ce´cile Carre´te ´ro, Cyrile Deranlot,Manuel Bibes, and Agne`s Barthe´le ´my, *Giant Electroresistance of Super-tetragonal BiFeO3 Based Ferroelectric Tunnel Junctions.* ACS Nano, 2013. **7**(6): p. 5385-5390.
36. André Chanthbouala, V.G., Ryan O. Cherifi, Karim Bouzehouane, Stéphane Fusi, Xavier Moya, Stéphane Xavier, Hiroyuki Yamada, Cyrile Deranlot, Neil D. Mathur Manuel Bibes Agnès Barthélémy and Julie Grollie, *A ferroelectric memristor.* Nature Materials, 2012. **11**: p. 860-864.
37. Zhao, T., et al., *Electrical control of antiferromagnetic domains in multiferroic BiFeO3 films at room temperature.* Nat Mater, 2006. **5**(10): p. 823-9.
38. Chu, Y.H., et al., *Electric-field control of local ferromagnetism using a magnetoelectric multiferroic.* Nat Mater, 2008. **7**(6): p. 478-82.
39. Béa, H., et al., *Spintronics with multiferroics.* Journal of Physics: Condensed Matter, 2008. **20**(43): p. 434221.
40. Seidel, J., et al., *Domain wall functionality in BiFeO3.* Phase Transitions, 2013. **86**(1): p. 53-66.
41. Seidel, J. and L.M. Eng, *Shedding light on nanoscale ferroelectrics.* Current Applied Physics, 2014. **14**(8): p. 1083-1091.
42. Keith T. Butler, J.M.F.a.A.W., *Ferroelectric materials for solar energy conversion: photoferroics revisited.* Energy Environ. Sci., 2015. **8**: p. 838-848.
43. S.Y Yang, J.S., S.Y. Byrnes, P. Shafer, C.-H. Yang, M.D. Rossell, P. Yu, Y.-H Chu, J.F. Scott, J.W. Ager III, L.W. Martin, and R. Ramesh, *Above-bandgap voltages from ferroelectric photovoltaic devices.* Nature Nanotechnology, 2010. **5**: p. 143-147.
44. Choi, T., et al., *High rectification and photovoltaic effect in oxide nano-junctions.* New Journal of Physics, 2012. **14**(9): p. 093056.
45. Yang, S.Y., et al., *Photovoltaic effects in BiFeO[sub 3].* Applied Physics Letters, 2009. **95**(6): p. 062909.
46. Liao, W.Q., et al., *A lead-halide perovskite molecular ferroelectric semiconductor.* Nat Commun, 2015. **6**: p. 7338.
47. Bonnell, D.A., *Ferroelectric Organic Materials Catch Up with Oxides.* Science, 2013. **339**: p. 401-402.
48. Heeg, T., et al., *Growth and properties of epitaxial rare-earth scandate thin films.* Applied Physics a-Materials Science & Processing, 2006. **83**(1): p. 103-106.
49. Seidel, J., *Domain Walls as Nanoscale Functional Elements.* The Journal of Physical Chemistry Letters, 2012. **3**(19): p. 2905-2909.
50. Morozovska, A.N., et al., *Anisotropic conductivity of uncharged domain walls in BiFeO3.* Physical Review B, 2012. **86**(8).
51. Linze Li, P.G., Christopher T. Nelson, Jacob R. Jokisaari, Yi Zhang, Sung-Joo Kim, Alexander Melville, Carolina Adamo, Darrell G. Schlom, and Xiaoqing Pan,

Atomic Scale Structure Changes Induced by Charged Domain Walls in Ferroelectric Materials. Nano Letters, 2013. **13**: p. 5218-5223.
52. Stolichnov, I., et al., *Control of leakage conduction of high-fatigue-endurance (Pb, La)(Zr, Ti)O-3 film ferroelectric capacitors with Pt/SrRuO3 electrodes.* Applied Physics Letters, 1999. **75**(12): p. 1790-1792.
53. Stolichnov, I. and A. Tagantsev, *Space-charge influenced injection model for conduction in Pb(ZrxTi1-x)O-3 thin films.* Journal of Applied Physics, 1998. **84**(6): p. 3216-3225.
54. Guyonnet, J., et al., *Conduction at Domain Walls in Insulating Pb(Zr0.2Ti0.8)O3 Thin Films.* Advanced Materials, 2011. **23**(45): p. 5377-5382.
55. Eliseev, E.A., et al., *Conductivity of twin-domain-wall/surface junctions in ferroelastics: Interplay of deformation potential, octahedral rotations, improper ferroelectricity, and flexoelectric coupling.* Physical Review B, 2012. **86**(8).
56. Seidel, J., et al., *Domain Wall Conductivity in La-Doped $BiFeO_3$.* Physical Review Letters, 2010. **105**(19): p. 197603.
57. Farokhipoor, S. and B. Noheda, *Conduction through 71 degrees DomainWalls in $BiFeO_3$ Thin Films.* Physical Review Letters, 2011. **107**(12): p. 127601.
58. Catalan, G., *On the Link Beween Octahedral Rotations and Conductivity in the Domain Walls of BiFeO3.* Ferroelectrics, 2012. **433**: p. 65-73.
59. Ehara, Y., et al., *Ultrafast switching of ferroelastic nanodomains in bilayered ferroelectric thin films.* Applied Physics Letters, 2011. **99**(18): p. 182906.
60. Maksymovych, P., et al., *Polarization Control of Electron Tunneling into Ferroelectric Surfaces.* Science, 2009. **324**(5933): p. 1421-1425.
61. Maksymovych, P., et al., *Dynamic Conductivity of Ferroelectric Domain Walls in $BiFeO_3$.* Nano Letters, 2011. **11**(5): p. 1906-1912.
62. Maksymovych, P., et al., *Tunable Metallic Conductance in Ferroelectric Nanodomains.* Nano Letters, 2012. **12**(1): p. 209-213.
63. Martin, L.W. and R. Ramesh, *Multiferroic and magnetoelectric heterostructures.* Acta Materialia, 2012. **60**(6-7): p. 2449-2470.
64. Sando, D., et al., *Linear electro-optic effect in multiferroicBiFeO3thin films.* Physical Review B, 2014. **89**(19).
65. Kubel, F. and Schmid, H., *Structure of a Ferroelectric and Ferroelastic Monodomain Crystal of the Perovskite BiFeO3.* Acta Cryst., 1990. **B46**: p. 698-702.
66. A. E. Romanov, M.J.L., J. S. Speck, W. Pompe, S. K. Streiffer, C.M. Foster, *Domain pattern formation in epitaxial rhombohedral ferroelectric films. II. Interfacial defects and energetics.* Journal of Applied Physics, 1998. **83**(5): p. 2754-2765.
67. J. X. Zhang, Y.L.L., S. Choudhury, L. Q. Chen, Y. H. Chu, F. Zavaliche, M. P. Cruz, R. Ramesh, and Q. X. Jia, *Computer simulation of ferroelectric domain structures in epitaxial BiFeO3 thin films.* Journal of Applied Physics, 2008. **103**: p. 094111.
68. C. W. Huang, Z.H.C., and Lang Chen, *Thickness-dependent evolutions of domain configuration and size in ferroelectric and ferroelectric-ferroelastic films.* Journal of Applied Physics, 2013. **113**: p. 094101.

69. Qiu, Q.J.a.J.H., *The thickness dependence of ferroelectric and magnetic properties in epitaxial BiFeO3 thin films.* Journal of Applied Physics, 2006. **99**: p. 103901.
70. S. Y. Hu, Y. L. Li, and L. Q. Chen, *Effect of interfacial dislocations on ferroelectric phase stability and domain morphology in a thin film—a phase-field model.* J. Appl. Phys. 2003, **94** 2542.
71. Nelson, C.T., *The Nanoscale Structure and Dynamic Properties of Ferroelectric Films,* PhD Dissertation, 2011, University of Michigan: Ann Arbor, Michigan.
72. Gu, Y., et al., *Flexoelectricity and ferroelectric domain wall structures: Phase-field modeling and DFT calculations.* Physical Review B, 2014. **89**(17).
73. Marchand, R., L. Brohan, and M. Tournoux, *TiO2(B) A new form of titanium-dioxide and the potassium octatitanate $K_2Ti_8O_{17}$.* Materials Research Bulletin, 1980. **15**(8): p. 1129-1133.
74. Etacheri, V., et al., *Mesoporous TiO_2–B microflowers composed of (1 1$\bar{}$0) facet-exposed nanosheets for fast reversible lithium-ion storage.* Journal of Materials Chemistry A, 2013. **1**(39): p. 12028.
75. Feist, T.P. and P.K. Davies, *The Soft Chemical Synthesis of TiO_2 (B) from Layered Titinates.* Journal of Solid State Chemistry, 1992. **101**(2): p. 275-295.
76. Prochazka, J., et al., *Novel Synthesis of the TiO_2(B) Multilayer Templated Films.* Chemistry of Materials, 2009. **21**(8): p. 1457-1464.
77. Dylla, A.G., G. Henkelman, and K.J. Stevenson, *Lithium Insertion in Nanostructured TiO_2(B) Architectures.* Accounts of Chemical Research, 2013. **46**(5): p. 1104-1112.
78. Carter, D.B.W.a.C.B., *Transmission Electron Microscopy, an textbook for Materials Science*. 2009: Springer Publishing.
79. Butler, E.P., *In situ experiments in the transmission electron microscope.* Rep. Prog. Phys., 1978. **42**: p. 835-889.
80. Yamamoto, N., K. Yagi, and G. Honjo, *Electron-microscopit studies of Ferroelectri and Ferroelastic $Gd_2(MoO_4)_3$ Polarization Reversal and Field-induced phase transformation.* Physica Status Solidi a-Applied Research, 1980. **62**(2): p. 657-664.
81. Snoeck, E., et al., *Electron-microscopy stude of ferroelastic and ferroelectric domain-wall motions induced by the in-situ application of and electric field in $BaTiO_3$.* Phase Transitions, 1994. **46**(2): p. 77-88.
82. Tan, X.L., H. He, and J.K. Shang, *In situ transmission electron microscopy studies of electric-field-induced phenomena in ferroelectrics.* Journal of Materials Research, 2005. **20**(7): p. 1641-1653.
83. Tan, X.L. and J.K. Shang, *In-situ transmission electron microscopy study of electric-field-induced grain-boundary cracking in lead zirconate titanate.* Philosophical Magazine a-Physics of Condensed Matter Structure Defects and Mechanical Properties, 2002. **82**(8): p. 1463-1478.
84. Tan, X. and J.K. Shang, *Intersection of a domains in the c-domain matrix driven by electric field in tetragonal ferroelectric crystal.* Journal of Applied Physics, 2004. **96**(5): p. 2805-2810.

85. Qu, W., X. Zhao, and X. Tan, *Evolution of nanodomains during the electric-field-induced relaxor to normal ferroelectric phase transition in a Sc-doped $Pb(Mg_{1/3}Nb_{2/3})O_3$ ceramic.* Journal of Applied Physics, 2007. **102**(8).
86. Sato, Y., T. Hirayama, and Y. Ikuhara, *Real-Time Direct Observations of Polarization Reversal in a Piezoelectric Crystal: $Pb(Mg_{(1/3)}Nb_{(2/3)}O_{(3)}$-$PbTiO_{(3)}$ Studied via In Situ Electrical Biasing Transmission Electron Microscopy.* Physical Review Letters, 2011. **107**(18).
87. Winkler, C.R., et al., *Direct observation of ferroelectric domain switching in varying electric field regimes using in situ TEM.* Micron, 2012. **43**(11): p. 1121-1126.
88. Winkler, C.R., et al., *Accessing intermediate ferroelectric switching regimes with time-resolved transmission electron microscopy.* Journal of Applied Physics, 2012. **112**(5).
89. Chang, H.J., et al., *Atomically Resolved Mapping of Polarization and Electric Fields Across Ferroelectric/Oxide Interfaces by Z-contrast Imaging.* Advanced Materials, 2011. **23**(21): p. 2474.
90. Zhang, J.X., et al., *Large field-induced strains in a lead-free piezoelectric material.* Nature Nanotechnology, 2011. **6**(2): p. 97-101.
91. Nelson, C.T., et al., *Domain Dynamics During Ferroelectric Switching.* Science, 2011. **334**(6058): p. 968-971.
92. Gao, P., et al., *Revealing the role of defects in ferroelectric switching with atomic resolution.* Nature Communications, 2011. **2**: p. 591.
93. Gao, P., et al., *Direct observations of retention failure in ferroelectric memories.* Advanced materials (Deerfield Beach, Fla.), 2012. **24**(8): p. 1106-10.
94. Linze Li, J.R.J., and X.Q. Pan, *In-situ electron microscopy of ferroelectric domains.* MRS Bulliten, 2015. **40**: p. 53-61.
95. Hytch, M.J., E. Snoeck, and R. Kilaas, *Quantitative measurement of displacement and strain fields from HREM micrographs.* Ultramicroscopy, 1998. **74**(3): p. 131-146.
96. Jia, C.L., et al., *Unit-cell scale mapping of ferroelectricity and tetragonality in epitaxial ultrathin ferroelectric films.* Nature Materials, 2007. **6**(1): p. 64-69.
97. Jia, C.L., et al., *Effect of a Single Dislocation in a Heterostructure Layer on the Local Polarization of a Ferroelectric Layer.* Physical Review Letters, 2009. **102**(11).
98. Jia, C.L., et al., *Atomic-scale study of electric dipoles near charged and uncharged domain walls in ferroelectric films.* Nature Materials, 2008. **7**(1): p. 57-61.
99. Nelson, C.T., et al., *Spontaneous Vortex Nanodomain Arrays at Ferroelectric Heterointerfaces.* Nano Letters, 2011. **11**(2): p. 828-834.
100. Jia, C.L., et al., *Direct Observation of Continuous Electric Dipole Rotation in Flux-Closure Domains in Ferroelectric Pb(Zr,Ti)O-3.* Science, 2011. **331**(6023): p. 1420-1423.
101. Chang, H.J., et al., *Watching domains grow: In-situ studies of polarization switching by combined scanning probe and scanning transmission electron microscopy.* Journal of Applied Physics, 2011. **110**: p. 052014.

102. Borisevich, A.Y., et al., *Atomic-scale evolution of modulated phases at the ferroelectric-antiferroelectric morphotropic phase boundary controlled by flexoelectric interaction.* Nature Communications, 2012. **3**.
103. Lubk, A., et al., *Evidence of Sharp and Diffuse Domain Walls in $BiFeO_3$ by Means of Unit-Cell-Wise Strain and Polarization Maps Obtained with High Resolution Scanning Transmission Electron Microscopy.* Physical Review Letters, 2012. **109**(4).
104. Polking, M.J., et al., *Ferroelectric order in individual nanometre-scale crystals.* Nature Materials, 2012. **11**(8): p. 700-709.
105. Kalinin, S.V. and D.A. Bonnell, *Imaging mechanism of piezoresponse force microscopy of ferroelectric surfaces.* Physical Review B, 2002. **65**(12).
106. Park, M., et al., *Nanoscale ferroelectric switching behavior at charged domain boundaries studied by angle-resolved piezoresponse force microscopy.* Applied Physics Letters, 2011. **99**(14).
107. Park, M., et al., *Three-dimensional ferroelectric domain imaging of epitaxial $BiFeO_3$ thin films using angle-resolved piezoresponse force microscopy.* Applied Physics Letters, 2010. **97**(11).
108. Saurenbach, F. and B.D. Terris, *Imaging of ferroelectric domain walls by force microscopy.* Applied Physics Letters, 1990. **56**(17): p. 1703-1705.
109. Abplanalp, M., L.M. Eng, and P. Gunter, *Mapping the domain distribution at ferroelectric surfaces by scanning force microscopy.* Applied Physics a-Materials Science & Processing, 1998. **66**: p. s232-s234.
110. Bonnell, D.A., et al., *Piezoresponse Force Microscopy: A Window into Electromechanical Behavior at the Nanoscale.* Mrs Bulletin, 2009. **34**(9): p. 648-657.
111. Kalinin, S.V. and D.A. Bonnell, *Contrast mechanism maps for piezoresponse force microscopy.* Journal of Materials Research, 2002. **17**(5): p. 936-939.
112. Kalinin, S.V., R. Shao, and D.A. Bonnell, *Local phenomena in oxides by advanced scanning probe microscopy.* Journal of the American Ceramic Society, 2005. **88**(5): p. 1077-1098.
113. Ganpule, C.S., et al., *Imaging three-dimensional polarization in epitaxial polydomain ferroelectric thin films.* Journal of Applied Physics, 2002. **91**(3): p. 1477-1481.
114. Pan, K., et al., *Analyzing piezoresponse force microscopy for reconstruction of probed ferroelectric structures.* Journal of Applied Physics, 2012. **112**(5).
115. Peter, F., et al., *Piezoresponse in the light of surface adsorbates: Relevance of defined surface conditions for perovskite materials.* Applied Physics Letters, 2004. **85**(14): p. 2896-2898.
116. Wang, J.H. and C.Q. Chen, *A coupled analysis of the piezoresponse force microscopy signals.* Applied Physics Letters, 2011. **99**(17).
117. Soergel, E., *Piezoresponse force microscopy (PFM).* J. Phys. D: Appl. Phys., 2011. **44**: p. 464003.
118. Bhatia, B., et al., *High-temperature piezoresponse force microscopy.* Applied Physics Letters, 2011. **99**(17).
119. Balke, N., et al., *Deterministic control of ferroelastic switching in multiferroic materials.* Nature Nanotechnology, 2009. **4**(12): p. 868-875.

120. Jesse, S., et al., *Direct imaging of the spatial and energy distribution of nucleation centres in ferroelectric materials.* Nature Materials, 2008. **7**(3): p. 209-215.
121. Griggio, F., et al., *Mapping piezoelectric nonlinearity in the Rayleigh regime using band excitation piezoresponse force microscopy.* Applied Physics Letters, 2011. **98**(21).
122. Kumar, A., et al., *Dynamic piezoresponse force microscopy: Spatially resolved probing of polarization dynamics in time and voltage domains.* Journal of Applied Physics, 2012. **112**(5).
123. Gruverman, A., et al., *Vortex ferroelectric domains.* Journal of Physics-Condensed Matter, 2008. **20**(34).
124. Gruverman, A., D. Wu, and J.F. Scott, *Piezoresponse force microscopy studies of switching behavior of ferroelectric capacitors on a 100-ns time scale.* Physical Review Letters, 2008. **100**(9): p. 4.
125. Szot K., R.B., Peter F., Waser R., Tiedke S., *Electrical Characterization of Perovskite Nanostructures by SPM*, in *Scanning Probe Microscopy*, S.K.a.A. Gruverman, Editor. 2007, Springer: New York. p. 746-775.
126. George Sarau, A.B., Renata Lewandowska and Silke Christiansen, *From Micro– to Macro–Raman Spectroscopy: Solar Silicon for a Case Study.* Adv. Aspects Spectrosc., 2012: p. 221-246.
127. M. Kuball, J.M.H., M. J. Uren, T. Martin, J. C. H. Birbeck, R. S. Balmer, and B. T. Hughes, *Measurement of Temperature in Active High-Power AlGaN/GaN HFETs Using Raman Spectroscopy.* IEEE Electron Device Letters, 2002. **23**(1): p. 7-9.
128. White, S.N., *Laser Raman spectroscopy as a technique for identification of seafloor hydrothermal and cold seep minerals.* Chemical Geology, 2008.
129. R. Cusco, F.G.S.d.A.a.L.A., *Differentiation between Hydroxyapatite and /b-Tricalcium Phosphate by Means of u-Raman Spectroscopy.* Journal of the European Ceramic Society, 1998. **18**: p. 1301-1305.
130. Baroni, S., et al., *Phonons and related crystal properties from density-functional perturbation theory.* Reviews of Modern Physics, 2001. **73**(2): p. 515-562.
131. Ceperley, D.M., *Ground State of the Electron Gas by a Stochastic Method.* Physical Review Letters, 1980. **45**(7): p. 566-569.
132. Giannozzi, P., et al., *Quantum Espresso: a modular and open-source software project for quantum simulations of materials.* Journal of Physics-Condensed Matter, 2009. **21**(39).
133. John R. Ferraro, K.N., Chris W. Brown, *Introduction to Raman Spectroscopy*. 2nd ed. 2002: Elsevier Academic Press.
134. Z. Q. Lu, T.Q., and H. S. Reehal, *Polarization-dependent Raman spectra of thin crystalline silicon films.* Journal of Applied Physics, 2005. **97**(033512).
135. C. Beekman, A.A.R., Y.S. Oh, S.W. Cheong, and K.S. Burch, *Raman study of the phonon symmetries in BiFeO3 single crystals.* Phys. Rev. B, 2012. **86**(2).
136. Maitri P. Warusawithana, et al., *A Ferroelectric Oxide Made Directly on Silicon.* Science, 2009. **324**(5925): p. 367-370.
137. Schlom, R.R.a.D.G., *Orienting Ferroelectric Films.* 2006. **296**: p. 1975-1976.

138. Chen, L.-Q., *Phase-Field Method of Phase Transitions/Domain Structures in Ferroelectric Thin Films: A Review.* Journal of the American Ceramic Society, 2008. **91**(6): p. 1835-1844.
139. Chu, Y.H., et al., *Nanoscale Domain Control in Multiferroic BiFeO3 Thin Films.* Advanced Materials, 2006. **18**(17): p. 2307-2311.
140. Li, Y.L., et al., *Effect of electrical boundary conditions on ferroelectric domain structures in thin films.* Applied Physics Letters, 2002. **81**(3): p. 427.
141. Zhang, J.X., et al., *Computer simulation of ferroelectric domain structures in epitaxial BiFeO[sub 3] thin films.* Journal of Applied Physics, 2008. **103**(9): p. 094111.
142. Huang, C.W., et al., *Stability and crossover of 71° and 109° domains influenced by the film thickness and depolarization field in rhombohedral ferroelectric thin films.* Journal of Applied Physics, 2011. **110**(1): p. 014110.
143. Kenji Uchino, E.S., and Terukiuo Hirose, *Dependence of the Crystal Structure on Particle Size in Barium Titanate.* Journal of the American Ceramic Society, 1989. **72**(8): p. 1555-1558.
144. Tomoya Ohno, D.S., Kenji Ishikawa, and Hisao Suzuki, *Size effect for lead zirconate titanate nano-particles with PZT(40/60) composition.* Advanced Powder Technology, 2007. **18**(5): p. 579-589.
145. H. H. Wu, J.W., S. G. Cao, L. Q. Chen, and T. Y. Zhang, *Micro-/macro-responses of a ferroelectric single crystal with domain pinning and depinning by dislocations.* Journal of Applied Physics, 2013. **114**: p. 164108.
146. B. Srimathya, R.J., Indranil Bhaumikb, S. Ganesamoorthyc, A.K. Karnalb, P.K. Guptab, J. Kumara, *Role of dopant induced defects on the properties of Nd and Cr doped PZNT single crystals.* Materials Science and Engineering B, 2014. **185**: p. 60–66.
147. I. Bretos, R.J., C. Gutiérrez-Lázaro, I. Montero, and M. L. Calzada, *Atomic-scale mechanisms of ferroelastic domain-wall-mediated ferroelectric switching.* Nat Commun, 2013. **4**(2791).
148. Yachin Ivry , C.D., Daping Chu , and James F. Scott *Nano-Domain Pinning in Ferroelastic-Ferroelectrics by Extended Structural Defects.* Advanced Functional Materials, 2014. **24**: p. 5567–5574.
149. I. Bretos, R.J., C. Gutiérrez-Lázaro, I. Montero, and M. L. Calzada, *Defect-mediated ferroelectric domain depinning of polycrystalline BiFeO3 multiferroic thin films.* Applied Physics Letters, 2014. **104**: p. 092905.
150. Daniel M. Marincel , H.Z., Amit Kumar , Stephen Jesse , Sergei V. Kalinin , W. M. Rainforth , Ian M. Reaney , Clive A. Randall , and Susan Trolier-McKinstry, *Infl uence of a Single Grain Boundary on Domain Wall Motion in Ferroelectrics.* Advanced Functional Materials, 2014. **24**: p. 1409–1417.
151. Pan, K., et al., *Analyzing piezoresponse force microscopy for reconstruction of probed ferroelectric structures.* Journal of Applied Physics, 2012. **112**(5): p. 052016.
152. Chang, H., et al., *Watching domains grow: In-situ studies of polarization switching by combined scanning probe and scanning transmission electron microscopy.* Journal of Applied Physics, 2011. **110**(5): p. 052014.

153. Kalinin, S.V., et al., *Vector piezoresponse force microscopy.* Microsc Microanal, 2006. **12**(3): p. 206-20.
154. Ian MacLaren, L., Alan J. Craven, Quentin M. Ramasse, Bernhard Schaffer, Kambiz Kalantari, and Ian M. Reaney, *The atomic structure and chemistry of Fe-rich steps on antiphase boundaries in Ti-doped Bi0.9Nd0.15FeO3.* APL Materials, 2014. **2**: p. 066106.
155. Ian MacLaren, L., Owen Morris, Alan J. Craven, Robert L. Stamps, Bernhard Schaffer, Quentin M. Ramasse, Shu Miao, Kambiz Kalantari, Iasmi Sterianou, and Ian M. Reaney, *Local stabilisation of polar order at charged antiphase boundaries in antiferroelectric ($Bi_{0.85}Nd_{0.15}$)($Ti_{0.1}Fe_{0.9}$)O_3.* APL Materials, 2013. **1**: p. 021102.
156. Gao, P., et al., *Revealing the role of defects in ferroelectric switching with atomic resolution.* Nat Commun, 2011. **2**: p. 591.
157. Nelson, C.T., et al., *Domain dynamics during ferroelectric switching.* Science, 2011. **334**(6058): p. 968-71.
158. Deniz, H., et al., *Nanoscale Bi_2FeO_{6-x} precipitates in $BiFeO_3$ thin films: a metastable Aurivillius phase.* Journal of Materials Science, 2014. **49**(20): p. 6952-6960.
159. MacLaren, I., et al., *The atomic structure and chemistry of Fe-rich steps on antiphase boundaries in Ti-doped $Bi_{0.9}Nd_{0.15}FeO_3$.* APL Materials, 2014. **2**(6): p. 066106.
160. MacLaren, I., et al., *Local stabilisation of polar order at charged antiphase boundaries in antiferroelectric (Bi0.85Nd0.15)(Ti0.1Fe0.9)O3.* Apl Materials, 2013. **1**(2): p. 021102.
161. Axel Lubk, S.G., and N.A. Spaldin, *First-principles study of ferroelectric domain walls in multiferroic bismuth ferrite.* Phys. Rev. B, 2009. **80**(10).
162. J. Wang, J.B.N., H. Zheng, V. Nagarajan, S. B. Ogale, B. Liu1 D. Viehland, V. Vaithyanathan, 5 D. G. Schlom, U. V. Waghmare, N. A. Spaldin, K. M. Rabe, M. Wuttig, R. Ramesh, *Epitaxial $BiFeO_3$ Multiferroic Thin Film Heterostructures.* Science, 2003. **299**: p. 1719-1722.
163. Jiang, Q. and J.H. Qiu, *The thickness dependence of ferroelectric and magnetic properties in epitaxial $BiFeO_3$ thin films.* Journal of Applied Physics, 2006. **99**(10): p. 103901.
164. Zhao, J.L., et al., *Thickness dependence of piezoelectric property of ultrathin BiFeO3 films.* Physica B: Condensed Matter, 2012. **407**(12): p. 2258-2261.
165. Chu, Y.H., et al., *Ferroelectric size effects in multiferroic $BiFeO_3$ thin films.* Applied Physics Letters, 2007. **90**(25): p. 252906.
166. M. Huijben, P.Y., L. W. Martin, H. J. A. Molegraaf, Y.-H. Chu , M. B. Holcomb, N. Balke, G. Rijnders, and R. Ramesh, *Ultrathin Limit of Exchange Bias Coupling at Oxide Multiferroic/Ferromagnetic Interfaces.* Advanced Materials, 2013. **25**: p. 4739–4745.
167. Heron, J.T., D.G. Schlom, and R. Ramesh, *Electric field control of magnetism using BiFeO3-based heterostructures.* Applied Physics Reviews, 2014. **1**(2): p. 021303.
168. Gao, P., et al., *Atomic-scale mechanisms of ferroelastic domain-wall-mediated ferroelectric switching.* Nature Communications, 2013. **4**.

169. Gao, P., et al., *Ferroelastic domain switching dynamics under electrical and mechanical excitations.* Nat Commun, 2014. **5**: p. 3801.
170. Li, L., et al., *Atomic scale structure changes induced by charged domain walls in ferroelectric materials.* Nano Lett, 2013. **13**(11): p. 5218-23.
171. Winchester, B., Chen, L.Q.,, *Phase field model of domain structures in thin-film $BiFeO_3$ at differing film thicknesses.* Private Communication, Unpublished Data, 2010.
172. Folkman, C.M., et al., *Stripe domain structure in epitaxial (001) BiFeO[sub 3] thin films on orthorhombic TbScO[sub 3] substrate.* Applied Physics Letters, 2009. **94**(25): p. 251911.
173. Folkman, C.M., et al., *Study of defect-dipoles in an epitaxial ferroelectric thin film.* Applied Physics Letters, 2010. **96**(5): p. 052903.
174. Ying-Hao Chu, Q.H., Chan-Ho Yang, Pu Yu, Lane W. Martin, Padraic Shafer, and R. Ramesh, *Nanoscale Control of Domain Architectures in BiFeO3 Thin Films.* Nano Letters, 2009. **9**(4): p. 1726-1730.
175. N. Balke, S.C., S. Jesse, M. Huijben, Y.H. Chu, A.P. Baddorf, L.Q. Chen, R. Ramesh, and S.V. Kalinin, *Deterministic control of ferroelastic switching in multiferroic materials.* Nature Nanotechnology, 2009. **4**: p. 868-875.
176. Schlom, D.G., et al., *Strain Tuning of Ferroelectric Thin Films.* Annual Review of Materials Research, 2007. **37**(1): p. 589-626.
177. Uecker, R., et al., *Properties of rare-earth scandate single crystals (Re=Nd−Dy).* Journal of Crystal Growth, 2008. **310**(10): p. 2649-2658.
178. Chen, Z., et al., *Study of strain effect on in-plane polarization in epitaxial $BiFeO_3$ thin films using planar electrodes.* Physical Review B, 2012. **86**(23).
179. Maeng, W.J. and J.Y. Son, *Tetragonally strained $BiFeO_3$ thin film on single crystal Rh substrate.* Journal of Crystal Growth, 2013. **363**: p. 105-108.
180. Catalan, G., et al., *Wall thickness dependence of the scaling law for ferroic stripe domains.* Journal of Physics: Condensed Matter, 2007. **19**(2): p. 022201.
181. Daumont, C., et al., *Strain dependence of polarization and piezoelectric response in epitaxial $BiFeO_3$ thin films.* J Phys Condens Matter, 2012. **24**(16): p. 162202.
182. Chen, Z., et al., *180 degrees Ferroelectric Stripe Nanodomains in $BiFeO_3$ Thin Films.* Nano Lett, 2015. **15**(10): p. 6506-13.
183. Ren, W., et al., *Ferroelectric domains in multiferroic $BiFeO_3$ films under epitaxial strains.* Phys Rev Lett, 2013. **110**(18): p. 187601.
184. P.J. Ferreira, K.M., and E.A. Stach, Eds., *In SituTransmission Electron Microscopy.* MRS Bulletin, 2008. **33**: p. 83-90.
185. Bobji, M.S., et al., *A miniaturized TEM nanoindenter for studying material deformation in situ.* Measurement Science and Technology, 2006. **17**(6): p. 1324-1329.
186. Couret, A., et al., *In situ deformation in T.E.M.: recent developments.* Microscopy Microanalysis Microstructures, 1993. **4**(2-3): p. 153-170.
187. M. Legros, D.S.G., and C. Motz, *Quantitative In Situ Mechanical Testing in Electron Microscopes.* MRS Bulletin, 2010. **35**: p. 354-360.
188. Warren, O.L., et al., *In situ nanoindentation in the TEM.* Materials Today, 2007. **10**(4): p. 59-60.

189. Dahmen, M.A.W.a.U., *An In-Situ Nanoindentation Specimen Holder for a High-Voltage Transmission Electron Microscope.* Microsc Res Tech. **42**(4): p. 248-254.
190. Eric A. Stach, T.F., Andrew M. Minor, Doug K. Owen, John Cumings, Mark A. Wall, Tomas Chraska, Robert Hull, J.W. Morris, Jr., A. Zettl, and Ulrich Dahmen, *Development of a Nanoindenter for In Situ Transmission Electron Microscopy.* Microsc. Microanal., 2001(7): p. Microsc. Microanal.
191. Espinosa, H.D., R.A. Bernal, and T. Filleter, *In situ TEM electromechanical testing of nanowires and nanotubes.* Small, 2012. **8**(21): p. 3233-52.
192. Gao, P., et al., *In situ TEM studies of oxygen vacancy migration for electrically induced resistance change effect in cerium oxides.* Micron, 2010. **41**(4): p. 301-5.
193. Qi, X.Y., H.H. Liu, and X.F. Duan, *In situ transmission electron microscopy study of electric-field-induced 90° domain switching in $BaTiO_3$ single crystals.* Applied Physics Letters, 2006. **89**(9): p. 092908.
194. Mehraeen, S., et al., *A (S)TEM gas cell holder with localized laser heating for in situ experiments.* Microsc Microanal, 2013. **19**(2): p. 470-8.
195. Allard, L.F., et al., *Novel MEMS-based gas-cell/heating specimen holder provides advanced imaging capabilities for in situ reaction studies.* Microsc Microanal, 2012. **18**(4): p. 656-66.
196. Tyrone L. Daulton, B.J.L., Kristine Lowe, and Joanne Jones-Meehan, *In Situ Environmental Cell–Transmission Electron Microscopy Study of Microbial Reduction of Chromium(VI) Using Electron Energy Loss Spectroscopy.* Microsc. Microanal, 2001. **7**: p. 470-485.
197. Andrew J. Leenheer, K.L.J., Kevin R. Zavadil, John P. Sullivan, and C. Thomas Harris, *Lithium Electrodeposition Dynamics in Aprotic Electrolyte Observed in Situ via Transmission Electron Microscopy.* ACS Nano, 2015. **9**(4): p. 4379-4389.
198. Kim, S.J., et al., *Lithiation of Rutile TiO2-Coated Si NWs Observed by in Situ TEM.* Chemistry of Materials, 2015. **27**(20): p. 6929-6933.
199. McDowell, M.T., et al., *In situ TEM of two-phase lithiation of amorphous silicon nanospheres.* Nano Lett, 2013. **13**(2): p. 758-64.
200. Wang, C.M., et al., *In situ transmission electron microscopy observation of microstructure and phase evolution in a SnO(2) nanowire during lithium intercalation.* Nano Lett, 2011. **11**(5): p. 1874-80.
201. Cavalca, F., et al., *In situ transmission electron microscopy of light-induced photocatalytic reactions.* Nanotechnology, 2012. **23**(7): p. 075705.
202. Timmermans, F.J. and C. Otto, *Contributed review: Review of integrated correlative light and electron microscopy.* Rev Sci Instrum, 2015. **86**(1): p. 011501.
203. Bernal, R.A., R. Ramachandramoorthy, and H.D. Espinosa, *Double-tilt in situ TEM holder with multiple electrical contacts and its application in MEMS-based mechanical testing of nanomaterials.* Ultramicroscopy, 2015. **156**: p. 23-8.
204. Alexandra Nafari, D.K., Cristina Rusu, Krister Svensson, Håkan Olin, and Peter Enoksson, *MEMS Sensor for In Situ TEM Atomic Force Microscopy.* Journal of Microelectromechanical Systems, 2008. **17**(2): p. 328-333.
205. Allard, L.F., et al., *A new MEMS-based system for ultra-high-resolution imaging at elevated temperatures.* Microsc Res Tech, 2009. **72**(3): p. 208-15.

206. Ishida, T., et al., *Design and fabrication of MEMS-controlled probes for studying the nano-interface underin situTEM observation.* Journal of Micromechanics and Microengineering, 2010. **20**(7): p. 075011.
207. Jin, Q., et al., *A MEMS device for in-situ TEM test of SCS nanobeam.* Science in China Series E: Technological Sciences, 2008. **51**(9): p. 1491-1496.
208. Janusz Nowotny, M.A.A., Tadeusz Bak, Mohammad Asri Idris, Mihail Ionescu, Kathryn Prince, Mohd Zainizan Sahdan, Kamaruzzaman Sopian, Mohd Asri Mat Teridi and Wolfgang Sigmund, *Defect chemistry and defect engineering of TiO_2-based semiconductors for solar energy conversion.* Chem. Soc. Rev., 2015. **44**(8424).
209. Lam, P., et al., *Submonolayer InGaAs/GaAs quantum dot solar cells.* Solar Energy Materials and Solar Cells, 2014. **126**: p. 83-87.
210. Keith T. Butler, J.M.F.a.A.W., *Ferroelectric materials for solar energy conversion: photoferroics revisited.* Energy Environ. Sci., 2015. **8**(138): p. 838-848.
211. S. Y. Yang, J.S., S.J.Byrnes, P.Shafer, C.-H. Yang, M.D.Rossell, P.Yu, Y.-H.Chu, J. F. Scott, J.W.Ager, L.W.Martin and R. Ramesh, *Above-bandgap voltages from ferroelectric photovoltaic devices.* Nature Nanotechnology, 2010. **5**: p. 143-147.
212. Y. Zhu, M.M., M.-G. Han, J.D. Rameau, And M. Sfeir, *Multimodal Optical Nanoprobe For Advanced In-Situ Electron Microscopy.* Microscopy Today, 2012. **20**(6).
213. Furumoto, K., et al., *Development of Novel Optical Fiber System for Cathodoluminescence Detection in High Voltage Transmission Electron Microscope.* Materials Transactions, 2013. **54**(5): p. 854-856.
214. Miller, B.K. and P.A. Crozier, *System for in situ UV-visible illumination of environmental transmission electron microscopy samples.* Microsc Microanal, 2013. **19**(2): p. 461-9.
215. Itoh, Y. and T. Hasegawa, *Polarization Dependence of Raman Scattering from a Thin Film Involving Optical Anisotropy Theorized for Molecular Orientation Analysis.* Journal of Physical Chemistry A, 2012. **116**(23): p. 5560-5570.
216. Liu, T. and S. Kumar, *Quantitative characterization of SWNT orientation by polarized Raman spectroscopy.* Chemical Physics Letters, 2003. **378**(3-4): p. 257-262.
217. Richard-Lacroix, M. and C. Pellerin, *Accurate New Method for Molecular Orientation Quantification Using Polarized Raman Spectroscopy.* Macromolecules, 2013. **46**(14): p. 5561-5569.
218. DeWolf, I., *Micro-Raman spectroscopy to study local mechanical stress in silicon integrated circuits.* Semiconductor Science and Technology, 1996. **11**(2): p. 139-154.
219. G.Sarau, A.B., R. Lewandowska, and S. Christiansen, *From Micro-to Macro-Raman Spectroscopy: Solar Silicon for a Case Study*, in *Advanced Aspects of Spectroscopy*, D.M.A. (Ed.), Editor 2012.
220. Huang, C.W., et al., *Revealing anisotropic strain in exfoliated graphene by polarized Raman spectroscopy.* Nanoscale, 2013. **5**(20): p. 9626-32.

221. Ihm, J., A. Zunger, and M.L. Cohen, *Momentum-space Formalism for the Total Energy of Solids.* Journal of Physics C-Solid State Physics, 1979. **12**(21): p. 4409-4422.
222. Troullier, N. and J.L. Martins, *Efficient Pseudopotentials for Plane-wave Calculations.* Physical Review B, 1991. **43**(3): p. 1993-2006.
223. Bayerl, D. and E. Kioupakis, *Theoretical limits of thermoelectric figure of merit inn-typeTiO2polymorphs.* Physical Review B, 2015. **91**(16).
224. Jillian F. Banfield, D.R.V., David J. Smith, *The identification of naturally occurring TiO, (B) by structure determination using high-resolutionelectron microscopy, image simulation, and distanceJeast-squares refinement.* American Mineralogist, 1991. **76**: p. 343-353.
225. Stoyanov, E.L., F.; Steinle-Neumann, G, *The effect of valence state and site geometry on Ti L3,2 and O K electron energy-loss spectra of TixOy phases.* Am. Mineral., 2007. **92**.
226. Frank, O., et al., *Raman spectra of titanium dioxide (anatase, rutile) with identified oxygen isotopes (16,17,18).* Physical Chemistry Chemical Physics, 2012. **14**(42): p. 14567-14572.
227. Qiao, Y., X.L. Hu, and Y.H. Huang, *Microwave-induced solid-state synthesis of TiO_2(B) nanobelts with enhanced lithium-storage properties.* Journal of Nanoparticle Research, 2012. **14**(2).
228. Wang, Y., Electrochimica Acta, 2008. **53**: p. 7863-7868.
229. Xiang, G.L., et al., *Surface-specific interaction by structure-match confined pure high-energy facet of unstable TiO_2(B) polymorph.* Scientific Reports, 2013. **3**.
230. Stoyanov, E., F. Langenhorst, and G. Steinle-Neumann, *The effect of valence state and site geometry on Ti L3,2 and O K electron energy-loss spectra of Ti_xO_y phases.* American Mineralogist, 2007. **92**(4): p. 577-586.